Technische Universität München
TUM School of Engineering and Design

Numerical Modeling of High-Frequency Transverse Thermoacoustic Instabilities in Reheat Combustors

Pedro Romero Vega

Vollständiger Abdruck der von der TUM School of Engineering and Design der Technischen Universität München zur Erlangung des akademischen Grades eines

Doktors der Ingenieurwissenschaften (Dr.-Ing.)

genehmigten Dissertation.

Vorsitz:
Prof. Dr.-Ing. habil. Christian Große
Prüfer*innen der Dissertation:
1. Prof. Dr.-Ing. Thomas Sattelmayer
2. Prof. Dr.-Ing. Kilian Oberleithner
3. Bruno Schuermans, Ph.D.

Die Dissertation wurde am 03.11.2022 bei der Technischen Universität München eingereicht und durch die TUM School of Engineering and Design am 24.03.2023 angenommen.

Acknowledgements

This work was conducted during my research time at the Institute of Thermodynamics of the Technical University of Munich. The research project was funded by GE Power (former Alstom Power) and the German Federal Ministry of Economic Affairs and Energy (BMWi) within the framework of the AG Turbo COOREFLEX-TURBO research association (project no. 03ET7021T), which is gratefully acknowledged.

I would like to thank firstly my supervisor, Prof. Dr. Thomas Sattelmayer, not only for his scientific guidance along this journey, but also for his trust in me and his infinite patience in the end phase of the project. Special thanks also go to Dr. Bruno Schuermans, whose keen knowledge in thermoacoustics and always sharp remarks have contributed notably to the quality of this thesis. Thanks to Prof. Dr. Kilian Oberleithner for his interest in this research and taking over as second examiner. Thanks to Prof. Dr.-Ing. habil. Christian Große for organizing the doctoral defense as the chairman of the examination committee.

I would also like to acknowledge Tobias Hummel for giving me the opportunity to write a Master's thesis at the Institute and therefore, for introducing me to the topic of thermoacoustics. I thank him too for the support in getting me started with the research work. Similarly, thanks also to Frederik Berger for his contributions to the project.

Many thanks go to all colleagues of the Institute for the overall good working atmosphere. Most notably, the SI-Group, and especially Thomas Hofmeister and Gerrit Heilmann for the interesting and productive discussions about thermoacoustics and their encouragement to finish off this work. A special shoutout here also to Jonathan McClure for providing the experimental recordings in this thesis. Thanks to my students, Bugra Baris and Kah Joon Yong, for helping me out with this project. Thanks to all the administrative staff, especially Helga Bassett, for lightening all the paperwork. My deepest gratitude also to Aaron Endres for proofreading the first draft of this thesis and generally for all the support in the final phase of the Ph.D. project.

I regard this Ph.D. as the final part of my formal education, and therefore, at this point I remember many people who have been there along this journey and many people I learnt things from. Looking back, nothing –included the Ph.D.– was so mind-changing as studying at ETSIA. Been around for a while now and I can say that I've never seen a collection of raw talent like I saw at that place. Thanks to all people who helped me out there, especially Mars and Gon, for keeping me afloat in the hardest hours. This is yours more than you can imagine.

Many thanks also to the lively Little Spain we've created far away from home. Listing all the names here would be too long. You know who you are.

I want to thank my sister. It really ain't no words for describing your support. Also makes me very proud seeing you growing up from distance and experiencing how I turned from teacher to learner. Keep on pushing little sis, the world is yours for the taking.

Por último, muchas gracias también a mis padres, por inculcarme una serie de valores que aunque parecen extraños en el sitio de donde vengo, resultan muy útiles en el camino que voy haciendo.

Gracias a todos.

Munich, October 30, 2022

Pedro Romero Vega

Abstract

In this work, thermoacoustic linear stability limits of the first transverse eigenmode of a lab-scale reheat combustor are assessed using a hybrid Computational Fluid Dynamics/Computational Aeroacoustics (CFD/CAA) methodology. The analysis is based on eigenfrequency and growth rate computations with the Linearized Euler equations, which are solved using a stabilized Finite Element Method. Special focus is put on individual contributions of acoustic driving and damping of the studied eigenmode. The two relevant mechanisms of acoustic damping for the investigated benchmark are evaluated: interactions of acoustics and the non-homentropic, non-homogeneous background mean flow and viscothermal losses in the acoustic boundary layer. On the driving part, four different interactions between flame and acoustics are considered: flame displacement by the acoustic velocity field, flame deformation induced by flame displacement, acoustic modulation of reactive shear layers and acoustic modulation of autoignition time delay. For the last two mechanisms, which are specific for reheat flames, novel models for describing the flame-acoustic coupling are derived. Superposition of the aforementioned damping and driving mechanisms aims at characterize the thermoacoustic stability limits of high-frequency transverse modes in reheat combustors.

Kurzfassung

In dieser Arbeit werden die thermoakustischen linearen Stabilitätsgrenzen der ersten transversalen Eigenmode eines Reheat-Prüfstands untersucht. Dazu wird eine hybride CFD/CAA-Methodik (Engl.: Computational Fluid Dynamics/Computational Aeroacoustics) verwendet. Die Analyse basiert auf Eigenfrequenz- und Wachstumsratenberechnungen mit den linearisierten Euler-Gleichungen, die mit der stabilisierten Finite-Elemente-Methode gelöst werden. Dabei wird der Schwerpuntk auf die einzelnen Beiträge von akustischer Anfachung und Dämpfung der untersuchten Eigenmode gelegt. Die beiden relevanten Mechanismen der akustischen Dämpfung im untersuchten Benchmark werden bewertet: Interaktionen der Akustik mit der nicht-homentropen, inhomogenen mittleren Hintergrundströmung und thermoviskose Verluste in der akustischen Grenzschicht. Zusätzlich werden vier verschiedene Mechanismen für Interaktionen zwischen Flamme und Akustik betrachtet: Flammenverschiebung durch das akustische Geschwindigkeitsfeld, Flammendeformation durch Flammenverschiebung, akustische Modulation reaktiver Scherschichten und akustische Modulation der Selbstzündzeit. Für die letzten beiden Mechanismen, die für Reheat-Flammen charakteristisch sind, werden neuartige Modelle zur Beschreibung der Flammen-Akustik-Kopplung abgeleitet. Die Überlagerung der Dämpfungs- und Anfachungsmechanismen zielt darauf ab, die thermoakustischen Stabilitätsgrenzen hochfrequenter Transversalmoden in Reheat-Brennkammern zu charakterisieren.

Contents

List of Figures

List of Tables

Nomenclature

Latin Characters

c	Progress variable [-]
c	Speed of sound [$\mathrm{m\,s^{-1}}$]
c_p	Heat capacity at constant pressure [$\mathrm{J\,kg^{-1}\,K^{-1}}$]
c_v	Heat capacity at constant volume [$\mathrm{J\,kg^{-1}\,K^{-1}}$]
E_a	Specific activation energy of reaction [$\mathrm{J\,kg^{-1}}$]
f	Frequency [Hz]
h	Specific enthalpy [$\mathrm{J\,kg^{-1}}$]
h_f°	Specific enthalpy of formation [$\mathrm{J\,kg^{-1}}$]
i	Imaginary unit [-]
$\boldsymbol{I}$	Identity tensor [-]
I	Acoustic energy flux [$\mathrm{J\,kg^{-1}}$]
I_0	Stretch factor [-]
$\boldsymbol{j}$	Diffusion flux vector [$\mathrm{kg\,m^{-2}\,s^{-1}}$]
k	Turbulent kinetic energy [$\mathrm{kg\,m^{-2}\,s^{-1}}$]
k	Thermal conductivity [$\mathrm{kg\,m^{-2}\,s^{-1}}$]
l_exo	Characteristic reaction length [m]
L_y	Wrinkling length scale [m]
LHV	Lower heating value [$\mathrm{J\,kg^{-1}}$]
$\boldsymbol{n}$	Normal vector [-]
N	Number of species [-]
p	Pressure [Pa]
$\dot{q}$	Volumetric heat release rate of combustion [$\mathrm{W\,m^{-3}}$]
R	Universal gas constant [$\mathrm{J\,kg^{-1}\,K^{-1}}$]

R_g	Specific gas constant [$\mathrm{J\,kg^{-1}\,K^{-1}}$]
$\langle RI \rangle$	Time-averaged Rayleigh index [$\mathrm{kg^2\,m^{-2}\,s^{-5}}$]
s	Specific entropy [$\mathrm{J\,K^{-1}}$]
s_L^0	Unstretched laminar flame speed [$\mathrm{m\,s^{-1}}$]
$\langle s_\mathrm{c} \rangle_s$	Mean laminar flame speed [$\mathrm{m\,s^{-1}}$]
S_m	Source of continuity equation [$\mathrm{kg\,m^{-2}\,s^{-1}}$]
t	Time [s]
T	Temperature [K]
$\boldsymbol{T}$	Viscous stress tensor [$\mathrm{kg\,m^{-1}\,s^{-1}}$]
$\boldsymbol{u}$	Velocity vector [$\mathrm{m\,s^{-1}}$]
u	Velocity in x-direction [$\mathrm{m\,s^{-1}}$]
v	Velocity in y-direction [$\mathrm{m\,s^{-1}}$]
W	Molecular weight [$\mathrm{kg\,mol^{-1}}$]
$[X]$	Molar concentration [$\mathrm{mol\,m^{-3}}$]
Y	Mass fraction [-]
Z	Reduced acoustic impedance [-]

Greek Characters

α	Damping rate [$\mathrm{rad\,s^{-1}}$]
α_τ	SUPG stabilization parameter [-]
δ_L	Laminar flame thickness [m]
$\vec{\Delta}$	Displacement vector [m]
ε	Turbulent dissipation [$\mathrm{m^2\,s^{-3}}$]
λ	Excess air ratio [-]
γ	Heat capacity ratio [-]
μ	Dynamic viscosity [$\mathrm{kg\,m^{-1}\,s^{-1}}$]
ν	Kinematic viscosity [$\mathrm{m^2\,s^{-1}}$]
ρ	Density [$\mathrm{kg\,m^{-3}}$]
Σ	Flame surface density [$\mathrm{m^{-1}}$]
σ_y	Flamelet orientation factor [-]
τ	Non-dimensional ignition time [-]
τ_ρ	Heat release parameter [-]

$\boldsymbol{\Omega}$	Vorticity [s^{-1}]
ω	Angular frequency [$\mathrm{rad\,s}^{-1}$]
$\dot{\omega}$	Chemical reaction rate [$\mathrm{kg\,m}^{-3}\,\mathrm{s}^{-1}$]

Subscripts

$(\cdot)_{\mathrm{ai}}$	Auto-ignition
$(\cdot)_{\mathrm{b}}$	Burned
$(\cdot)_{\mathrm{chem}}$	Chemical
$(\cdot)_{\mathrm{e}}$	Excess
$(\cdot)_{\mathrm{f}}$	Fuel
$(\cdot)_{i}$	i-th species
$(\cdot)_{\mathrm{ign}}$	Ignition
$(\cdot)_{\mathrm{is}}$	Isentropic
$(\cdot)_{\mathrm{pr}}$	Propagation
$(\cdot)_{\mathrm{sens}}$	Sensible
$(\cdot)_{\mathrm{th}}$	Thermal
$(\cdot)_{\mathrm{t}}$	Turbulent
$(\cdot)_{\mathrm{u}}$	Unburned
$(\cdot)_{\mathrm{v}}$	Viscous

Superscripts

$(\hat{\cdot})$	Complex amplitude
$(\tilde{\cdot})$	Density-weighted average
$(\cdot)'$	Fluctuating quantity
$(\bar{\cdot})$	Stationary quantity

Non-Dimensional Numbers

Da	Damköhler number
Ma	Mach number
Pr	Prandtl number
Re	Reynolds number
Sc	Schmidt number

Operators

H	Heaviside function
$\mathrm{D}(\cdot)/\mathrm{D}t$	Material derivative
$(\cdot):(\cdot)$	Double dot product
$\mathrm{Re}(\cdot)$	Real part
$\lvert\cdot\rvert$	Module
$\lVert\cdot\rVert$	Euclidean norm

Abbreviations

1D	One Dimensional
2D	Two Dimensional
3D	Three Dimensional
APE	Acoustic Perturbation Equations
BML	Bray-Moss-Libby
CCUS	Carbon Capture, Utilization and Storage
CFD/CAA	Computational Fluid Dynamics/Computational Aeroacoustics
CI	Confidence Interval
CL	Chemiluminescence
DG-FEM	Discontinous Galerkin Finite Element Method
DLE	Dry Low-Emission
DOF	Degree of Freedom
EBU	Eddy Break-Up

GHG	Greenhouse Gas
GLS	Galerkin Least Squares
HC	Non-methane Hydrocarbons
HF	High Frequency
IEA	International Energy Agency
LEE	Linearized Euler Equations
LES	Large Eddy Simulation
LF	Low frequency
LNSE	Linearized Navier-Stokes Equations
LOS	Line of sight
PDF	Probability Density Function
PSD	Power Spectral Density
RANS	Reynolds Averaged Navier-Stokes
RMS	Root-Mean-Square
SUPG	Streamline Upwind Petrov-Galerkin
T1	First Transverse Mode
UHC	Unburned Hydrocarbons
URANS	Unsteady Reynolds Averaged Navier-Stokes

1 Introduction

1.1 Motivation

World primary energy demand grows and will continue to grow in the forthcoming decades as a result of increasing human population, economic development and urbanization. Within this context, the International Energy Agency (IEA) forecasts an increment of the global electricity consumption of approximately 30% between 2019 and 2030. As anthropogenic global warming currently poses a serious threat to our way of life, increasing electricity demand has to be met while reducing greenhouse gas (GHG) emissions. To curb GHG emissions, the share of produced electricity by renewables is planned to sharply increase up to about 40% of the global power generation mix by 2030. Specifically, solar and wind energy will account for approximately 20% of the electricity mix [1]. As a consequence, traditional thermal power plants will, on the one hand, reduce their current share of the mix. On the other hand, those that remain will have to deal with the intrinsic volatility of solar and wind energy to ensure reliable supply of electricity. Unlike oil- and coal-fired power plants, the IEA forecasts that gas-fired power plants will maintain their current share of market in the foreseeable future mainly due two reasons: (i) gas-fired power plants can operate flexibly enough to quickly dispatch when renewable production does not meet demand and (ii) natural gas is almost 50 % less CO_2 emission-intensive compared to liquid and solid fuels [2]. This last figure can be potentially further reduced or even zeroed by using alternative fuels like hydrogen or deploying Carbon Capture, Utilization, and Storage (CCUS) technologies [3].

Therefore, operational flexibility arises as the key requirement for the integration

of gas turbines into power grids that are mainly governed by intermittent power production of renewable sources [4]. The role of gas turbine power plants in these dynamic grids is to back up the fluctuating renewable production to keep a stable power supply. Such a role requires flexible operation in terms of quick start-up times and high ramping rates in both directions, up to full load and down to load part [4]. In addition to operational flexibility, fuel flexibility plays also a crucial role in the current and future power generation infrastructure. Currently, fuel flexibility is mainly motivated by the increasingly diverse offer of gaseous fuel sources e.g. natural, shale gas or syngas with very different fuel reactivities. In the future, fuel flexibility will be even more relevant as power-to-gas technology arises as a suitable approach to long-term energy storage. Thus, gas turbines will have to operate on fuels with increasing content –or even full content– of highly reactive hydrogen obtained from excess power generation of renewables. Finally, besides operational and fuel flexibility, requirements on reduced emissions, thermal efficiency and reliability also have to be considered.

Different concepts of combustors with low emission and ultra low emission characteristics have been proposed, cf. Ref. [5] for a thorough review. Among them, the reheat combustion[i] technology is an appealing concept due to its positive outcomes in operational and fuel flexibility. One of the leading design challenges of reheat combustion technology is controlling its tendency to develop thermoacoustic instabilities. Acoustic perturbations may affect the unsteady heat release of the flame resulting in a feedback loop that may lead ultimately to thermoacoustic instabilities. Thermoacoustic instabilities exhibit high-amplitude pressure oscillations that hinder normal operation of the gas turbine, e.g. reducing the operational window, increasing emissions, causing mechanical fatigue. Therefore, development of predictive tools that allow for strategies to mitigate thermoacoustic instabilities is required. Numerical methods are suitable for this purpose, since these methods can predict the instabilities already in early design phases. The present thesis is framed within that context.

[i] Also referred to as sequential combustion

1.2 Reheat Combustion Technology

The most prominent characteristic of gas turbines with reheat technology is that the combustion process is split into two separate stages, cf. Fig. 1.1. Operational flexibility benefits directly from the second combustion stage. The possibility of running the first stage alone results in an improved turndown ratio. Additionally, the relative load between both chambers can be adjusted to obtain very different power outputs while keeping high exhaust gas temperatures that preserves combined-cycle efficiency. This relative load adjustment between primary and secondary combustion stages is also beneficial for dealing with different fuel reactivities and grants a wide Wobbe Index[ii] usage. Furthermore, reheat combustion intrinsically decouples thermal efficiency from emissions. In standard designs with a single stage, thermal efficiency increases with higher firing temperatures as more work can be extracted from the thermodynamic cycle [6]. However, high firing temperatures penalize NO_x emissions as these grow quickly with temperature [5]. By splitting the combustion stage, same power outputs as for single stage combustion can be obtained for in comparison, lower firing temperatures [6, 7]. At last, CO and unburned hydrocarbons (UHC) do not increase as they are burned in the secondary combustion stage [8]. Therefore, NO_x, CO and UHC pollutant emissions are kept under control.

Reheat combustion technology was first commercialized by ABB[iii] in the 1990s with the models GT24/26[iv] [8, 9], cf. Fig. 1.1 a). In these gas turbine models, the first combustion stage is carried out in an annular combustion chamber composed of swirl stabilized burners, the so-called EV burner (EnVironmental). This is a lean premixed dry low emission NO_x burner with the ability to use gaseous and liquid fuels [10, 11]. The products of combustion are expanded in a first turbine stage, retrieving some shaft power and decreasing the temperature of the flue gases. In the subsequent second combustor, fuel is then injected into the gas stream that exits the first turbine stage. Due to the existing high temperatures, the fuel-enriched mixture is able to self-ignite and an auto-ignition stabilized secondary flame is formed. This second stage is known as Sequential EnViron-

[ii] Indicator of interchangeability of gaseous fuels
[iii] Later Alstom and now Ansaldo Energia
[iv] Now GE GT24 and GE/Ansaldo GT26

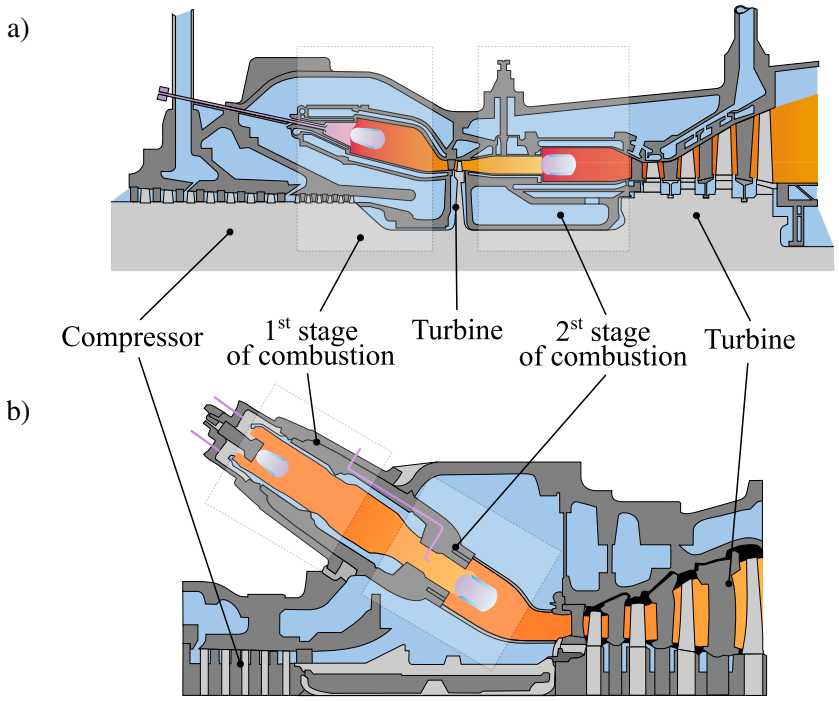

Figure 1.1: *a) Alstom's GT24 [6] and b) Ansaldo's GT36 [12].*

mental (SEV) burner. Thereafter, a second turbine expansion takes place, which completes the shaft power extraction. This concept has been lately revisited in Ansaldo's GT36 [12]. The main difference compared to the GT24/26 models is that turbine expansion stage between the combustion stages has been removed, cf. Fig. 1.1 b). In the GT36 part of the fresh air stream is not injected into the first combustor stage but is instead used to dilute the products of combustion of the first stage upstream of the secondary fuel injection. This design, in which the intermediate temperature between combustion stages can be tuned, has performed outstandingly with hydrogen-natural gas fuel blends with up to 70 % (vol.) hydrogen content [13]. Eliminating the intermediate turbine expansion also simplifies the overall design as the first turbine stage is avoided. Furthermore, by additionally replacing the annular combustors of the GT24 with can combustors in the GT36, the maintenance and transference from test rig experiments were improved [12].

1.3 High-Frequency Thermoacoustic Instabilities

One of the main challenges in development of reheat combustion gas turbines is mitigation of thermoacoustic instabilities. In this section, firstly, a differentiation between low- and high-frequency thermoacoustic instabilities is made. Secondly, an overview of relevant work in the field of thermoacoustic instabilities in reheat combustors is introduced. Finally, a survey of suitable numerical approaches for modeling thermoacoustic instabilities is presented.

1.3.1 Differences Between Low- and High-Frequency Thermoacoustic Instabilities

High-frequency[v] (HF) instabilities can be characterized by the ratio of acoustic wavelength to flame length scale [14]. In the HF regime, the flame length scale is in the same order of magnitude as acoustic wavelengths. These flames are designated as acoustically non-compact. Their unsteady heat release interacts with the acoustic field locally as thermoacoustic coupling occurs mainly by local, in-phase interactions between acoustic variables and the flame [15, 16]. Therefore, the spatial distribution of heat release is relevant. In the low-frequency (LF) regime, however, the spatially integrated heat release governs the thermoacoustic coupling. Instabilities take place due to a time-delayed response of unsteady heat release to convectively transported velocity, equivalence ratio or temperature fluctuations [17]. Finally, in the LF regime mainly one-dimensional longitudinal modes prevail, whereas HF instabilities usually feature complex three-dimensional resonant modes. In this work, only transverse eigenmodes are considered. This implies that acoustic perturbations are predominantly perpendicular to the bulk-flow direction in the combustor. All in all, due to their distinct physics models derived in the LF regime cannot be extended or have to be extended with care to the HF regime.

[v] Usually in the range of kHz, high-frequency instabilities are also denoted as screech type instabilities.

1.3.2 Thermoacoustic Instabilities in Reheat Combustors

During the past few decades, advances have been made in comprehension and prediction of LF thermoacoustic instabilities in gas turbines [18, 17]. Specifically, different studies of modeling of LF instabilities in reheat combustors can be found in literature. Modeling approaches range from analytic solutions in idealized one-dimensional configurations [19] to Large Eddy Simulations (LES) with system identification methods to determine reheat flame transfer functions of GT24/26 gas turbines [20, 21]. Lately, a reheat combustor test rig devoted to investigations in the LF regime has been commissioned at the ETH Zurich. Experiments [22] and simulations [23, 24, 25] of such a benchmark have identified acoustically induced fuel-jet flapping [22] and temperature perturbations in the mixing zone of the test rig as the cause of heat release modulation in its reheat flame.

Study of instabilities in reheat combustors in the HF regime has been less frequent. Some examples of studies are the unstable mode identification and Helmholtz dampers design of the GT24/26 in [26, 27] or the numerical investigations of a generic reheat combustor by Zellhuber [28]. In the latter, reactive LES simulations unraveled acoustically induced flame displacement and density fluctuations as the origin of heat release modulation. Similar flame response to transverse acoustic modes had been previously observed in swirl-stabilized flames by Schwing [29] Recently, at the Institute of Thermodynamics of the TU Munich, a reheat combustor setup has been commissioned in order to study transverse, high-frequency instabilities at atmospheric pressure [30]. In that test rig, the reheat flame in the secondary combustion chamber presents zones stabilized via propagation and auto-ignition similarly to gas turbine reheat combustors [30, 31]. First experiments with this test rig showed modulation of heat release in the reactive shear layers for a transverse eigenmode occurring at about 1.6 kHz [31]. Possible explanations for the modulation are that heat release is modified either by acoustically induced vortex shedding or by equivalence ratio fluctuations [31]. Acoustically induced vortex shedding had been observed in swirl-stabilized flames for high-frequency transverse eigenmodes [32]. However, in that swirl-stabilized combustor, vortex shedding is only associated with acoustic damping [33] as the flame is quenched in the shear layer due to high stretch rates [34]. Further investigations in the reheat combustor test rig concerned high-frequency limit cycle oscillations of the

first transverse eigenmode in direction of the shortest dimension of the chamber [31, 35]. At approximately 3 kHz a self-excited unstable eigenmode occurred at high thermal power levels and increased fuel reactivities, which are achieved by blending natural gas with propane. Acoustically induced flame displacement and compression and expansion of the flame was observed. These mechanisms have been previously observed, investigated and modeled for swirl-stabilized flames [15, 16, 29]. Furthermore, heat release modulation of the pressure-sensitive auto-ignition stabilized flame zones due to acoustic pressure was identified as an additional coupling mechanism [35].

1.3.3 Numerical Modeling of Thermoacoustic Instabilities

The previous section highlights the relevance of experiments for modeling thermoacoustic instabilities. However, especially at early design stages, simulations are much more cost-effective and therefore technically relevant. Simulation methods for modeling thermoacoustic instabilities can be classified mainly into two groups [36]. The first group comprises unsteady computational fluid dynamics (CFD) such as large eddy simulations (LES) [37] or unsteady Reynolds-Averaged Navier-Stokes (URANS) simulations [38] in which unsteady reacting flows are computed. This approach captures the flame dynamics and its corresponding interaction with the acoustic variables. However these methods present a major drawback regarding their intensive use of computing resources. Their high turnaround time avoids its application at industrial level or early design stages. A second group of more time-efficient procedures takes advantage of the scale disparity of acoustic motion compared to the background mean flow and only resolves the acoustic perturbations. The coupling between flame and acoustics is modeled in form of flame transfer functions, which relate the unsteady heat release to acoustic variables [15]. Subsequently, the unsteady heat release is used as a source in the acoustic governing equations. To this group belong the so-called hybrid methods, which are based on solving linearized acoustic perturbations around a steady-state mean flow. Hybrid methods present different levels of physical complexity. From more complex to less, one can distinguish linearized Navier-Stokes equations (LNSE) [39, 40] obtained by direct linearization of fluid-dynamics governing equations. The solution of the LNSE contains

coupled elemental acoustic, vortical and entropy modes [41] and accounts for viscous dissipation and thermal conduction. In acoustics, viscous and thermal dissipation only play a role in particular areas such as acoustic boundary layers or aerodynamic source regions. As those effects are usually not relevant for most practical cases, LNSE can be simplified to the linearized Euler equations (LEE) [42], which still describe the three elemental modes but without friction nor thermal diffusion. In a further step of simplification, convectively transported vorticity modes can be eliminated, retrieving the so-called acoustic perturbation equations (APE) [43], which only account for acoustic modes and their interaction with the background mean flow. If the mean flow is neglected altogether, the hybrid methods simplify to the classical wave equation (or the Helmholtz equation in the frequency domain). Hybrid methods and the wave equation can be applied to arbitrarily complex geometries without limitations in the frequency regime –i.e. with appropriate models for the unsteady heat release they can describe interactions of non-compact flames with acoustics. This entails an advantage compared to a common approach employed in thermoacoustics: network models [44, 45, 46]. Network models are formed by interconnecting transfer matrices of lumped elements representative of e.g. ducts, area jumps, junctions, flames. As all relevant acoustic features of the system have to be captured in acoustically compact elements, their extension to complex geometries and especially high-frequency regimes is cumbersome.

Among all aforementioned modeling approaches, the LEE is the simplest that captures all elemental modes: acoustic, vortical and entropy modes. Furthermore, the LEE capture linear interactions between mean flow and perturbation fields that lead to damping of the acoustic modes in HF transverse modes [33].

The LEE can be solved in time or frequency domain (cf. Chapter 3 of Ref. [42] for a thorough review of both approaches). Frequency domain analysis is advantageous compared to time domain analysis for the implementation of boundary conditions and the simplification of modal analysis. When only linear effects are considered, the frequency domain is preferred. Time domain analysis on the other hand is favorable for describing non-linear effects [42]. For complex geometries like those often encountered in gas turbine combustors, the LEE are discretized using the Finite Element Method (FEM). FEM schemes are numerically unstable

when the mean flow is included in the LEE [47]. Therefore, numerical stabilization is required. Different methods like e.g. the streamline upwind Petrov-Galerkin (SUPG) or the Galerkin Least Squares (GLS) add artificial diffusion to fix the numerical instability [47]. For certain configurations, the added artificial diffusion can have a noticeable impact on the computed damping rates so quantification of the unphysical damping is advisable. This can be performed following [48], in which the APE are employed to determine the amount of unphysical damping. Lately, discontinuous Galerkin FEM (DG-FEM) has been proposed as a suitable method to solve thermoacoustic governing equations such as the LNSE without numerical stabilization [49]. In DG-FEM, discontinuous basis functions are employed to discretize the numerical domain. This precludes integration over the entire domain. Therefore, the numerical flux between internal elements of the mesh have to be considered, similarly to finite volume methods. With appropriate models for describing the numerical flux, stable solutions can be obtained. However, the number of degrees of freedom (DOF) increases. Compared to stabilized FEM, DG-FEM requires about one order of magnitude more DOF for similar mesh sizes. As memory requirements escalate accordingly, application of DG-FEM to more complex configurations of technical relevance may be difficult.

1.4 Scope and Structure of the Thesis

Due to their outstanding operational and fuel flexibility, gas turbines with reheat combustion are a key technology for ensuring reliable power supply in power grids increasingly dominated by intermittent renewables. Thermoacoustic instabilities represent a chief design challenge in the development of reheat combustors. However, there is still limited comprehension of thermoacoustic instabilities in reheat combustors, especially at high frequencies. In this respect, obtaining linear models is of interest. With linear models, the linear stability margins of combustors can be determined. An oscillation, if it is linearly stable, will not grow in amplitude, avoiding potential damage. Furthermore, knowledge of eigenfrequencies of the system is useful to avoid structural resonance. Numerical methods are a price- and time-competitive solution compared to experiments for studying a complex multi-physics phenomenon as thermoacoustic instabilities.

In particular, it is advantageous developing predictive numerical tools for early design stages.

This work deals with the numerical modeling of HF thermoacoustic instabilities in reheat combustors, focusing on the second combustor in which the flame is partially stabilized via auto-ignition. The main objective is to assess linear stability limits of a lab-scale reheat combustor numerically. To do so, a hybrid Computational Fluid Dynamics/Computational Aeroacoustics (CFD/CAA) methodology is employed to determine eigenfrequencies and growth rates of the first transverse (T1) eigenmode.

From this main objective, specific research tasks can be derived:

- Development of models to describe linear damping in high-frequency regimes compatible with the CFD/CAA methodology.
- Development of models to describe linear flame-acoustic interactions in high-frequency regimes with focus on reheat flames.
- Assessment of individual contributions of each damping and driving mechanism to the growth rate and validation against experimental benchmarks.

Consequently, this thesis is structured as follows. The theoretical background is presented in Chapter 2. Therein, governing equations for the stationary reactive mean flow and acoustic motion as well as for the thermoacoustic coupling mechanisms employed are introduced. In Chapter 3, the experimental setup of the lab-scale reheat combustor used for validation of the numerical simulations is briefly introduced. Chapter 4 deals with the procedure and results of the reactive CFD simulations required as input for the stationary mean flow in the thermoacoustic governing equations. In Chapter 5, a linear stability analysis of the first transverse eigenmode of the lab-scale reheat combustor is carried out. Specifically, the individual contribution of each relevant mechanism responsible for acoustic damping and driving is calculated for different operating points. Subsequently, the net contribution of damping and driving is assessed and the linear thermoacoustic stability is determined. Finally, in Chapter 6, conclusions are drawn and future work is suggested.

2 Theoretical Background

This chapter lays the theoretical foundations of the thesis. In this work, a hybrid CFD/CAA methodology [40, 42] is employed for modeling thermoacoustic instabilities. CFD/CAA methods only solve linearized acoustic perturbations around a stationary background mean flow. The thermoacoustic coupling is modeled by relating the unsteady heat release to acoustic variables. These coupling models are subsequently used as sources in the acoustic governing equations. Summing up, hybrid CFD/CAA methods require three elements: a stationary mean flow, governing equations for linear acoustic motion and models for thermoacoustic coupling. All three of them are introduced in this chapter, which is structured as follows. First, the general equations of reacting mean flows are introduced. Second, the RANS[i] equations, which describe the stationary reactive mean flow, are presented. Special focus is put on specific combustion models for the auto-ignition core and propagation stabilized shear layers of the reheat flame. Third, the governing equations of acoustic motion, the linearized Euler equations (LEE) are derived. Finally, the different thermoacoustic coupling mechanisms considered in this thesis are introduced.

2.1 Governing Equations of Reacting Flows

Dynamics of unsteady reacting flows is described by the Navier-Stokes equations. Equations of conservation of mass, species, momentum and energy for a multi-component, chemically reacting ideal gas, neglecting volumetric forces are given by [50]:

[i] Reynolds-Averaged Navier-Stokes

$$\frac{\mathrm{D}\rho}{\mathrm{D}t} = -\rho\ (\nabla \cdot \boldsymbol{u}) \tag{2.1}$$

$$\rho\frac{\mathrm{D}Y_i}{\mathrm{D}t} = \nabla \cdot \boldsymbol{j}_i + \dot{\omega}_i \tag{2.2}$$

$$\rho\frac{\mathrm{D}\boldsymbol{u}}{\mathrm{D}t} = -\nabla p + \nabla \cdot \boldsymbol{T} \tag{2.3}$$

$$\rho\frac{\mathrm{D}h}{\mathrm{D}t} = \frac{\mathrm{D}p}{\mathrm{D}t} + \nabla \cdot (k\nabla T) + \boldsymbol{T} : (\nabla \boldsymbol{u}) \tag{2.4}$$

where $\rho, \boldsymbol{u}, Y_i, p, T, h$ are density, velocity, mass fraction of i-th species, pressure, temperature and specific enthalpy, respectively. Thermal conductivity is represented by k. In the species conservation Eq. 2.2, the diffusion flux vector of i-th species is denoted by $\boldsymbol{j}_i$. This describes the diffusion of mass due to gradients in concentration, pressure and temperature. The rate of production or consumption of mass due to chemical reaction for i-th species, also simply referred to as reaction rate of i-th species, is represented by $\dot{\omega}_i$. The viscous stress tensor, $\boldsymbol{T}$, is defined as:

$$\boldsymbol{T} = \mu \left[\nabla \boldsymbol{u} + (\nabla \boldsymbol{u})^{\mathrm{T}} - \frac{2}{3}(\nabla \cdot \boldsymbol{u})\ \boldsymbol{I} \right] \tag{2.5}$$

where μ is the dynamic viscosity and $\boldsymbol{I}$ is the identity tensor. Finally, the material derivative operator is defined as $\mathrm{D}\ (\cdot)/\mathrm{D}t = \partial(\cdot)/\partial t + \boldsymbol{u} \cdot \nabla(\cdot)$. The fluid is modeled as an ideal gas, so pressure, density and temperature are related by the ideal gas law:

$$p = \rho R_{\mathrm{g}} T, \tag{2.6}$$

where R_{g} denotes the specific gas constant, defined as the quotient of the universal gas constant and the mean molecular weight of the mixture $R_{\mathrm{g}} = R/W$. The mean molecular weight is given by [50]:

$$\frac{1}{W} = \sum_{i}^{N} \frac{Y_i}{W_i}, \tag{2.7}$$

where N is the total number of species. Note that although the molecular weights of each species (W_i) are constant, the mean molecular weight (W) of the mixture changes due to the combustion process and often it is different for the reactants and products. Usually, separating chemical and sensible components of the enthalpy in the energy Eq. 2.4 is useful for numerical implementation:

$$h = \sum_i^N Y_i h_i = h_{\text{sens}} + \underbrace{\sum_i^N Y_i h_{\text{f},i}^\circ}_{h_{\text{chem}}}, \tag{2.8}$$

where $h_{\text{f},i}^\circ$ is the enthalpy of formation of i-th species. By inserting Eq. 2.8 into the energy Eq. 2.4 is obtained:

$$\rho \frac{\mathrm{D}h_{\text{sens}}}{\mathrm{D}t} = \dot{q} + \frac{\mathrm{D}p}{\mathrm{D}t} + \nabla \cdot (k \nabla T) + \boldsymbol{T} : (\nabla \boldsymbol{u}) - \sum_i^N h_{\text{f},i}^\circ (\nabla \cdot \boldsymbol{j}_i). \tag{2.9}$$

In Eq. 2.9 the mass-fraction-dependent terms are eliminated using the conservation of species Eq. 2.2. Furthermore, the definition of volumetric heat release rate of combustion reaction is employed:

$$\dot{q} = -\sum_i^N \dot{\omega}_i h_{\text{f},i}^\circ. \tag{2.10}$$

Finally, for ideal gases, in which the heat capacity at constant pressure of the i-th species ($c_{p,i}$) is a function of temperature, the sensible enthalpy[ii] can be written as a function of T as follows:

$$h_{\text{sens}} = \sum_i^N Y_i \int_{T^\circ}^T c_{p,i}(T^*)\, \mathrm{d}T^*. \tag{2.11}$$

[ii] Usually the reference temperature is set to the reference state $T^\circ = 293.15\,\text{K}$, at which $h_{\text{sens},i} = 0$. Note also that the enthalpy of formation (cf. Eq. 2.8) is evaluated at the same reference state [50].

The conservation of mass (cf. Eq. 2.1), species (cf. Eq. 2.2), momentum (cf. Eq. 2.3) and energy (cf. Eq. 2.9) equations, together with the equation of state for ideal gases (cf. Eq. 2.6) form a coupled system of $N + 6$ partial differential equations. These theoretically allow to solve for the $N + 6$ unknowns of the problem, namely pressure, temperature, density, vector velocity and mass fractions of N species. However, it is not possible to directly solve them in practical applications. Therefore, the next sections are devoted to introducing models and simplifications to obtain reacting flow solutions. Furthermore, the above presented reacting flow Navier-Stokes equations serve as basis for the derivation the equations of acoustic motion, which are presented in Section 2.3.2.

2.2 RANS of Reacting Flows

A stationary background mean flow is required by the CFD/CAA methodology as input for the governing equations of acoustic motion. Therefore, the RANS formulation, which delivers a stationary averaged solution of the reacting turbulent flow, is used to simulate the mean flow. RANS is preferred to more complex CFD techniques such as Large-Eddy Simulations (LES) due to better time efficiency and the status of RANS as industrial standard. This allows to easily transfer the here developed models and procedures to industry. Those models could be potentially utilized already at early design stages due to the affordable computing power required. As RANS simulations are considered a standard engineering tool, the procedure for obtaining RANS equations is only briefly summarized in the following. Interested reader is referred to [50] for a thorough description of the derivation as well as a listing of the resulting equations.

RANS equations are obtained after time-averaging instantaneous Navier-Stokes Eqs. 2.3-2.4. As a result of averaging, additional unclosed terms that are correlations between turbulent fluctuations appear. In combustion, where density heavily varies between unburned and burned phases, density weighted averaging[iii] is employed. This prevents correlations between fluctuating density and any other flow variable from appearing and therefore reduces the number of unclosed terms. In any case, the remainder of unclosed terms have to be appropriately modeled

[iii] Also referred to as Favre averaging

using closure models for turbulence and turbulent combustion.

In the current work, the objective is to model reheat flames. This kind of flame is formed when fuel is injected in a sufficiently hot stream of vitiated gas, which is product of a previous combustion stage. Due to high temperatures, the fuel self-ignites after a certain induction time –the auto-ignition time delay– and eventually a flame is stabilized downstream of the fuel injector [51]. In gas turbine combustors, reheat flames are also stabilized by propagation in the shear layers [23, 31, 51, 52]. Therefore, suitable combustion models for each stabilization mechanism are employed. A sketch of a characteristic reheat flame is depicted in Fig. 2.1.

In this work, for modeling the reheat turbulent combustion, fully premixed operation is assumed. This greatly simplifies the RANS simulations as complex reactive simulations with ternary mixing of vitiated gas stream, fuel and shielding air are avoided [51]. Despite the fact that premixed operation may seem a crude assumption at first glance, near the reheat combustion chamber inlet flow conditions are very close to premixed [30]. This assumption shall be validated with mixing studies of the vitiated stream and fuel in Section 4.2. Effects of unmixedness and possible associated equivalence ratio fluctuations due to the technical premixing are left to future studies. Specifics about the turbulence closure models and premixed turbulent combustion models for propagation and auto-ignition stabilized zones of the flame are discussed below.

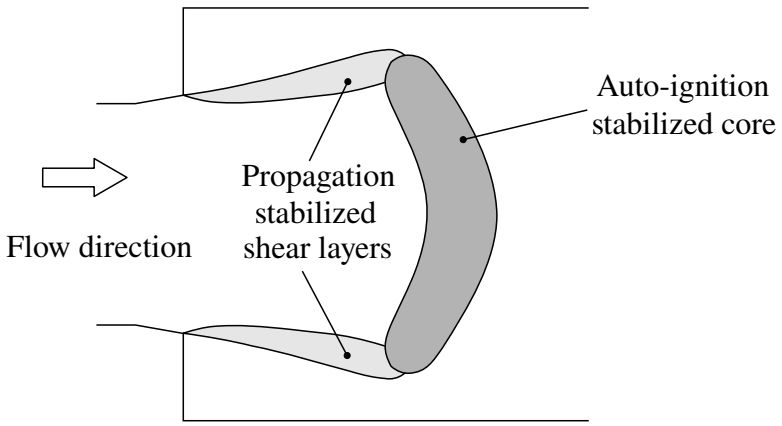

Figure 2.1: *Schematic of a characteristic reheat flame.*

2.2.1 Premixed k-ε RANS CFD

Among the different turbulent closure models available in RANS, the realizable k-ε is employed [53]. This model combines robustness and economy of the standard k-ε model while capturing jets, vortices and separated flows more accurately [50, 53]. This is relevant for a correct representation of the recirculation zones in the experimental reheat setup that is used for validation of the CFD methodology.

Mathematically, the realizable k-ε model is a so-called two-equation model in which balance equations for the turbulent kinetic energy (k) and the turbulent dissipation rate (ε) are added to the RANS equations. Following the Boussinesq assumption, the influence of the turbulent shear stress on the flow is modeled by a function of the turbulent viscosity (μ_t) and the mean velocity gradients [50]. The turbulent viscosity is in turn described by an algebraic function of the kinetic energy and the turbulence dissipation rate. Compared to the standard k-ε model, the realizable k-ε includes an improved formulation for the turbulent viscosity using a variable model constant and a upgraded transport equation for the dissipation rate [53].

In order to model turbulent combustion, it is necessary to evaluate the mean reaction rates. Reaction rates are strongly non-linear functions of temperature and composition which follow Arrhenius-like expressions. Therefore, direct application of density-weighted averaging delivers again complex quadratic terms which need a closure. However, mean reaction rates can be still derived from physical analysis. As stated in the introduction of the chapter, fully premixed operation is assumed. Similarly to laminar premixed combustion, in turbulent premixed combustion, a flame front propagates into a mixture of unburned premixed reactants. The chief difference compared to laminar combustion is that turbulence may influence the internal and external flame structure. Wrinkling of the flame front due to turbulent fluctuations for example, increases the effective flame front area, which in turn augments the consumption rate of reactants and the macroscopic turbulent flame speed at which the flame front propagates.

Assessing how turbulence and flame interact is the key aspect that allows to select adequate combustion models. This interaction is characterized using scale analysis. Specifically, characteristic turbulent and chemical times are compared

by the Damköhler number (Da):

$$Da(l_\mathrm{t}) = \frac{t_\mathrm{t}}{t_\mathrm{chem}} = \frac{l_\mathrm{t}/u'_\mathrm{RMS}}{\delta_\mathrm{L}/s^0_\mathrm{L}}. \tag{2.12}$$

The turbulent characteristic time (t_t) is the ratio of the turbulent integral scale (l_t) to the RMS turbulent velocity (u'_RMS). The chemical characteristic time (t_chem) is the ratio of the laminar flame thickness (δ_L) to the unstretched laminar flame speed (s^0_L). When turbulent times are much larger than chemical times ($Da \gg 1$), the internal flame structure remains close to laminar as it is not affected by turbulence. This is the so-called thin flame regime or flamelet regime. By inserting the order of magnitude of flow quantities from the validation experiments into Eq. 2.12, it can be shown that this is the predominant propagation regime in the studied configuration[iv].

In summary, turbulent premixed combustion can be regarded as a two-component flow consisting of regions of unburned reactants and fully burned products. The turbulent flame can be regarded as an interface that separates both components. Under the assumption of single one-step irreversible chemistry, constant bulk pressure, unity Lewis number and adiabatic conditions, it is possible to define a combustion progress variable c. By definition c is zero in regions of unburned reactants and unity in burned products. The position of the flame front is determined by solving the transport equation of the density-weighted-averaged progress variable $\tilde{c}$:

$$\bar{\rho}\frac{\partial \tilde{c}}{\partial t} + \bar{\rho}\tilde{\boldsymbol{u}} \cdot \nabla \tilde{c} = \nabla \cdot \left[\left(\frac{k}{c_p} + \frac{\mu_\mathrm{t}}{Sc_\mathrm{t}} \right) \nabla \tilde{c} \right] + \tilde{\dot{\omega}}_c \tag{2.13}$$

where $(\tilde{\cdot})$ represents the density-weighted average operator. The turbulent Schmidt number is denoted by Sc_t and the mean reaction rate is $\tilde{\dot{\omega}}_c$. The term $\tilde{\dot{\omega}}_c$ contains the chemical source term of propagation and auto-ignition:

$$\tilde{\dot{\omega}}_c = \tilde{\dot{\omega}}_{c,\mathrm{pr}} + \tilde{\dot{\omega}}_{c,\mathrm{ai}}. \tag{2.14}$$

[iv] The Damköhler number for the benchmark configuration is $Da \approx 10$, being the order of magnitude of $l_\mathrm{turb} \approx 1 \times 10^{-2}$ m, $u'_\mathrm{RMS} \approx 10\,\mathrm{m\,s^{-1}}$, $\delta \approx 1 \times 10^{-4}$ m and $s^0_\mathrm{L} \approx 1\,\mathrm{m\,s^{-1}}$

In Eq. 2.14, the mean reaction rate of propagation is $\tilde{\omega}_{c,\mathrm{pr}}$. This is modeled using the Bray-Moss-Libby model [54], which is described in detail in Section 2.2.2. The mean reaction rate of auto-ignition is denoted by $\tilde{\omega}_{c,\mathrm{ai}}$, which is modeled in Section 2.2.3.

Mathematically, Eq. 2.13 substitutes the conservation of energy and species equations. Therefore, an additional relation is needed to describe the temperature field. Assuming adiabatic combustion, temperature is defined as linear function of the progress variable:

$$\tilde{T} = (1 - \tilde{c})\, T_{\mathrm{u}} + \tilde{c}\, T_{\mathrm{b}} \tag{2.15}$$

where T_{u} and T_{b} are temperatures of unburned and burned mixture, respectively. Throughout the simulations, T_{b} is set to be equal to the adiabatic flame temperature. As thermodynamic pressure is assumed to be constant, density can be immediately retrieved from the temperature field using the ideal gas law and known conditions at the unburned side:

$$\bar{\rho}\tilde{T} = \rho_{\mathrm{u}} T_{\mathrm{u}}. \tag{2.16}$$

Finally the heat released by the combustion reaction can be obtained from the mean reaction rate similarly to Eq. 2.10:

$$\bar{\dot{q}} = Y_{\mathrm{f,u}}\, LHV\, \tilde{\omega}_c \tag{2.17}$$

where $Y_{\mathrm{f,u}}$ is the mass fraction of fuel in the unburned mixture and LHV is the lower heating value of the employed fuel.

2.2.2 Propagation Combustion Modeling: The Bray-Moss-Libby Model

The Bray-Moss-Libby (BML) model [54] is employed to model the propagation stabilized shear layers of the reheat flame (cf. Fig. 2.1). This model is suitable for

$Re \gg 1$ and $Da \gg 1$. Following [55], the mean reaction rate is described using the flame surface density:

$$\tilde{\dot{\omega}}_{c,\mathrm{pr}} = \rho_{\mathrm{u}} \langle s_{\mathrm{c}} \rangle_s \Sigma, \tag{2.18}$$

where the unburned density (ρ_{u}) is multiplied by the mean laminar flame speed at the average stretch rate ($\langle s_{\mathrm{c}} \rangle_s$) and flame surface density (Σ). $\langle s_{\mathrm{c}} \rangle_s$ can be related to the unstretched laminar flame speed by multiplying the latter by a stretch factor (I_0). Then, $\langle s_{\mathrm{c}} \rangle_s = I_0 s_{\mathrm{L}}^0$. In this work, as a first approximation, $\langle s_{\mathrm{c}} \rangle_s$ is simplified to:

$$\langle s_{\mathrm{c}} \rangle_s = s_{\mathrm{L}}^0 \tag{2.19}$$

in which stretch effects are neglected. The flame surface density Σ measures the available flame surface per unit of volume. It is thus a measure of flame front wrinkling. In [54] an algebraic expression for Σ depending only in geometric parameters and the density-averaged progress variable is given by:

$$\Sigma = \frac{g}{\sigma_y L_y} \frac{1 + \tau_\rho}{(1 + \tau_\rho \tilde{c})^2} \tilde{c}(1 - \tilde{c}). \tag{2.20}$$

In Eq. 2.20, g is a constant that arises from the integration of the presumed BML's probability density function (PDF). In the current work, g is equal to unity, as a double Dirac delta PDF is assumed. The heat release parameter is denoted by τ_ρ and is defined as $\tau_\rho = \rho_u / \rho_b - 1$. Moreover, σ_y is the flamelet orientation factor, which is assumed constant and taken as $\sigma_y = 0.5$. Finally, L_y is the wrinkling length scale, which is usually assumed proportional to the integral turbulence length scale as follows:

$$L_y = C_{\mathrm{L}}\, l_{\mathrm{t}} \left(\frac{s_{\mathrm{L}}^0}{u'_{\mathrm{RMS}}} \right)^n, \tag{2.21}$$

where C_{L} and n are two model constants that are valued 1 following [56]. By inserting Eq. 2.19 and Eq. 2.20 into Eq. 2.18, a closed expression for the propagation

mean reaction rate is obtained:

$$\tilde{\dot{\omega}}_{c,\mathrm{pr}} = \frac{g\rho_\mathrm{u} s_\mathrm{L}^0}{\sigma_\mathrm{y} L_\mathrm{y}} \frac{(1+\tau_\rho)}{(1+\tau_\rho \tilde{c})^2} \tilde{c}(1-\tilde{c}). \tag{2.22}$$

2.2.3 Auto-Ignition Combustion Modeling

When fuel is injected into a hot vitiated crossflow at sufficiently high temperature, a chemical chain reaction initiates in the mixture. A pool of radicals is formed, which splits the fuel molecules and produce even more radicals. After some time, the auto-ignition time delay, heat is released by the chemical reactions. Macroscopically, after fuel injection, random auto-ignition kernels appear in the vitiated crossflow. Those grow in size while being convected downstream by the flow. If a sufficient number of auto-ignition kernels appear, they can merge into the auto-ignition stabilized flame front (cf. sketch of a characteristic reheat flame with auto-ignition flame front in Fig. 2.1). Therefore, the key ingredient that determines the flame front position is the auto-ignition time delay.

In order to model auto-ignition, an approach similar to that developed by Haßlberger [57] is employed. To do so, an additional transport equation for the non-dimensional ignition time $\tau = t/t_{\mathrm{ign,p}}$ is required. Note that in the definition of τ, the denominator $t_{\mathrm{ign,p}}$ is the cumulative auto-ignition time delay which accounts for history of auto-ignition kernel until ignition. In the current configuration where the inlet conditions are premixed and therefore homogeneous, $t_{\mathrm{ign,p}}$ is constant throughout its history and can be simply calculated using the local auto-ignition time delay (t_{ign}) for the inlet conditions. Within the context of this work, local auto-ignition time delay means that t_{ign} is a function of local spatial conditions e.g. local temperature, fuel composition or density. All in all, analogously to the transport Eq. 2.13 for $\tilde{c}$, a transport equation for $\tilde{\tau}$ reads:

$$\bar{\rho}\frac{\partial \tilde{\tau}}{\partial t} + \bar{\rho}\tilde{\boldsymbol{u}} \cdot \nabla\tilde{\tau} - \nabla \cdot \left[\left(\frac{k}{c_p} + \frac{\mu_\mathrm{t}}{Sc_\mathrm{t}} \right) \nabla\tilde{\tau} \right] = \frac{\bar{\rho}}{t_{\mathrm{ign}}}. \tag{2.23}$$

Equation 2.23 determines where the volumetric chemical source term for auto-ignition in the reaction progress Eq. 2.14 is applied, as auto-ignition can only take place at locations where $\tilde{\tau} > 1$. For the sake of simplicity, the dependency of t_{ign} on temperature and fuel composition is modeled using an empirical correlation developed by Spadaccini and Kolket [58], which reads:

$$t_{\mathrm{ign}} = 1.77 \times 10^{-14} \exp\left(\frac{E_{\mathrm{a}}}{RT}\right) [\mathrm{O_2}]^{-1.05} [\mathrm{CH_4}]^{0.66} [\mathrm{HC}]^{-0.39} \tag{2.24}$$

In Eq. 2.24, $[\cdot]$ denotes molar concentration[v] and HC stands for non-methane hydrocarbons. The activation energy of the reaction is given by E_{a}. By exploiting the definition of molar concentration of the i-th species,

$$[X_i] = \rho \frac{Y_i}{W_i}, \tag{2.25}$$

an explicit dependency of t_{ign}[vi] on density and temperature is retrieved,

$$t_{\mathrm{ign}}(T, \rho) = 1.77 \times 10^{-14} \exp\left(\frac{E_{\mathrm{a}}}{RT}\right) \rho^{-0.78} \left(\frac{Y_{\mathrm{O_2}}}{W_{\mathrm{O_2}}}\right)^{-1.05} \left(\frac{Y_{\mathrm{CH_4}}}{W_{\mathrm{CH_4}}}\right)^{0.66} \left(\frac{Y_{\mathrm{HC}}}{W_{\mathrm{HC}}}\right)^{-0.39} \tag{2.26}$$

For given mass fractions of oxygen, methane and propane of the corresponding operating point, which in reheat combustion are known from the first combustion stage products and fuel composition, according to Eq. 2.26 the ignition delay is a direct function of temperature and density only. This serves as a source in the transport equation of the non-dimensional ignition time, Eq. 2.23.

After having determined the position of the auto-ignition flame front, a model for the mean reaction rate is still required. Following [57], the volumetric mean reaction rate is expressed as:

[v] Expressed in $\mathrm{mol\,cm^{-3}}$ in Eq. 2.24

[vi] Expressed in s

$$\tilde{\omega}_{c,\mathrm{ai}} = \bar{\rho}\tilde{u}\frac{2B}{l_{\mathrm{exo}}}\tilde{c}(1-\tilde{c})\mathrm{H}(\tilde{\tau}-1), \tag{2.27}$$

where $\tilde{u}$ is the mean flow velocity magnitude. $B \approx 4.59$ is a constant that arises from imposing that the jump of $\tilde{c}$ occurs within the limits of the characteristic reaction length l_{exo}. Therefore, l_{exo} is directly proportional to the width of the flame. This parameter is adjusted ad-hoc for matching experimentally observed reaction zone lengths. Finally, note that the auto-ignition reaction rate, Eq. 2.27, is activated only for $\tilde{\tau} > 1$ by means of the Heaviside function $\mathrm{H}(\tilde{\tau}-1)$.

2.2.4 Numerical Solution of Reactive RANS Equations

The reactive mean flow simulations are carried out in the volume-finite-element commercial package ANSYS Fluent®[53]. The embedded capabilities to simulate turbulent premixed combustion are extended via User Defined Functions (UDFs) in order to implement the auto-ignition time delay correlation (cf. Eq. 2.24) and the tailored mean reaction rates for propagation and auto-ignition (cf. Eqs. 2.22 and 2.27, respectively). Further details on the CFD setup are given in Chapter 4.

2.3 Governing Equations of Thermoacoustics

In this section the governing equations of thermoacoustics used for this work are derived. First, the linearized Euler equations (LEE) in frequency domain are obtained from the Navier-Stokes equations. Second, the LEE are simplified for isentropic thermoacoustics. Third, boundary conditions for the LEE are introduced. Finally, the numerical solution of the LEE using FEM is briefly discussed.

2.3.1 Linearized Euler Equations in Frequency Domain

In thermoacoustics, molecular diffusion only plays a role in particular areas such as acoustic boundary layers or aerodynamic source regions [59]. As those effects are usually not relevant for most practical cases, the first step for obtaining thermoacoustic governing equations is to simplify the Navier-Stokes Eqs. 2.1-

2.4 to the inviscid Euler equations by neglecting thermal conductivity, dynamic viscosity and the diffusion flux vectors –i.e. $k = 0$, $\mu = 0$ and $\boldsymbol{j}_i = 0$, yielding:

$$\frac{\mathrm{D}\rho}{\mathrm{D}t} = -\rho\ (\nabla \cdot \boldsymbol{u}), \tag{2.28}$$

$$\rho \frac{\mathrm{D}Y_i}{\mathrm{D}t} = \dot{\omega}_i, \tag{2.29}$$

$$\rho \frac{\mathrm{D}\boldsymbol{u}}{\mathrm{D}t} = -\nabla p, \tag{2.30}$$

$$\rho c_p \frac{\mathrm{D}T}{\mathrm{D}t} = \frac{\mathrm{D}p}{\mathrm{D}t} + \dot{q}. \tag{2.31}$$

Note that in the energy Eq. 2.31, sensible enthalpy is expressed as a function of temperature. This is done under two assumptions. First, a perfect gas is assumed, which implies that $c_{p,i}$ is independent of temperature. Second, c_p is mixture averaged –i.e. $c_p = \sum_i^N Y_i c_{p,i}$ – because reactive species are strongly diluted in inert nitrogen, which is the dominant species of the mixture. The latter is a reasonable assumption for air-breathing combustion systems, especially those that feature lean combustion like modern gas turbines. However, under this assumption, limitations may arise for modeling thermoacoustic instabilities in oxy-fuel combustion or rocket engines in which pure oxygen is used as oxidant [17]. The next step in the derivation is to eliminate temperature in the energy Eq. 2.31. Following [17], the substantial derivative of temperature, by using the rule of chain in the equation of state of ideal gases (cf. Eq. 2.6), can be written as:

$$\frac{\mathrm{D}T}{\mathrm{D}t} = \frac{T}{p}\frac{\mathrm{D}p}{\mathrm{D}t} - \frac{T}{\rho}\frac{\mathrm{D}\rho}{\mathrm{D}t} - T\sum_i^N \frac{W}{W_i}\frac{\mathrm{D}Y_i}{\mathrm{D}t} \tag{2.32}$$

In Eq. 2.32, the last term on the RHS accounts for the change of molar concentration in the gas due to combustion. Such a term is related to the change of mean molecular weight due to combustion as follows:

$$\sum_i^N \frac{W}{W_i}\frac{\mathrm{D}Y_i}{\mathrm{D}t} = \sum_i^N \frac{W}{\rho}\frac{\dot{\omega}_i}{W_i} = -\frac{1}{W}\frac{\mathrm{D}W}{\mathrm{D}t}. \tag{2.33}$$

In the present work, following the reasoning set out before for c_p, mean molecular weight is assumed constant as reactants and oxidants are heavily diluted in inert nitrogen. Thus, the last term on the RHS of Eq. 2.32 is zero. Considering this assumption, after inserting Eq. 2.32 into the energy Eq. 2.31, the latter is reduced to:

$$\frac{\mathrm{D}p}{\mathrm{D}t} - c^2 \frac{\mathrm{D}\rho}{\mathrm{D}t} = (\gamma - 1)\dot{q}, \tag{2.34}$$

where c is the speed of sound and γ is the heat capacity ratio, which is defined as $\gamma = c_p/c_v$. Note that the assumption of constant c_p and W due to the dominant nitrogen mass fraction in unburned and burned gases implies that effectively there is only one averaged species. Therefore, the conservation of species Eq. 2.29 can be left out as it does not add relevant information. Finally, also note that under the aforementioned assumptions the simplified Euler Eqs. 2.28, 2.30 and 2.34 are equivalent to a non-reactive monocomponent conservation set of equations to which heat is communicated from an external source, which are the equations traditionally employed in thermoacoustics, cf. for example Ref. [60].

Under the assumption of smallness of acoustic motion, Eqs. 2.28, 2.30 and 2.34 can be linearized around a steady mean state. Furthermore, if harmonic oscillations are assumed, a generic primary variable $\phi(\boldsymbol{x}, t)$ can be written as:

$$\phi(\boldsymbol{x}, t) = \bar{\phi}(\boldsymbol{x}) + \mathrm{Re}\left[\hat{\phi}(\boldsymbol{x}) \exp(\mathrm{i}\omega t)\right], \tag{2.35}$$

in which hatted variables ($\hat{\cdot}$) stand for complex amplitudes of acoustic magnitudes and the bar ($\bar{\cdot}$) indicates stationary mean flow quantities. The latter are obtained from the RANS equations introduced in Section 2.2. In Eq. 2.35, the angular frequency is represented by ω, which is related to the frequency (f) by $\omega = 2\pi f$. Applying the decomposition given in Eq. 2.35 to Euler Eqs. 2.28, 2.30 and 2.34 the LEE in frequency domain are obtained[vii]:

[vii] In Eq. 2.37 the operator $(\boldsymbol{u}\cdot\nabla)\boldsymbol{u} = \left(u_i \frac{\partial}{\partial x_i}\right) u_j = u_i \left(\frac{\partial u_j}{\partial x_i}\right)$

$$\mathrm{i}\omega\hat{\rho} + \nabla\cdot(\hat{\rho}\bar{\boldsymbol{u}}) + \nabla\cdot(\bar{\rho}\hat{\boldsymbol{u}}) = 0, \tag{2.36}$$

$$\mathrm{i}\omega\bar{\rho}\hat{\boldsymbol{u}} + \bar{\rho}\left[(\hat{\boldsymbol{u}}\cdot\nabla)\bar{\boldsymbol{u}} + (\bar{\boldsymbol{u}}\cdot\nabla)\hat{\boldsymbol{u}}\right] + \hat{\rho}(\bar{\boldsymbol{u}}\cdot\nabla)\bar{\boldsymbol{u}} + \nabla\hat{p} = 0, \tag{2.37}$$

$$\begin{aligned}&\mathrm{i}\omega\hat{p} + \bar{\boldsymbol{u}}\cdot\nabla\hat{p} + \hat{\boldsymbol{u}}\cdot\nabla\bar{p} = \ldots\\ &\ldots\bar{c}^2\left[\mathrm{i}\omega\hat{\rho} + \bar{\boldsymbol{u}}\cdot\nabla\hat{\rho} + \hat{\boldsymbol{u}}\cdot\nabla\bar{\rho} + \left(\frac{\hat{p}}{\bar{p}} - \frac{\hat{\rho}}{\bar{\rho}}\right)(\bar{\boldsymbol{u}}\cdot\nabla\bar{\rho})\right] + (\gamma-1)\hat{q}.\end{aligned} \tag{2.38}$$

Application of LEE in frequency domain is advantageous compared to time domain because it eases the implementation of the boundary conditions and simplifies the modal analysis [42]. The solution of the LEE, Eqs. 2.36-2.38, is composed of three different propagation modes, namely acoustic, vorticity and entropy modes [41, 18, 17]. Acoustic modes propagate as pressure waves at the speed of sound onto the mean flow velocity. Their thermodynamic change of state is isentropic and they are associated to an irrotational velocity field. Vorticity modes correspond to vorticity fluctuations advected by the mean flow velocity. They can be regarded as the solenoid part of the perturbation velocity [33]. Finally, entropy modes can be recognized as "hot spots" or non-isentropic temperature fluctuations which are also advected by the mean flow. They induce non-isentropic density changes, which in turn act as volumetric sources of the acoustic modes. Regarding thermoacoustic instabilities, mainly acoustic modes are of relevance as they can lead to self-sustained amplifying oscillations. Vorticity and entropy modes contribute only indirectly as part of acoustic damping and driving processes. These three intrinsic modes are only decoupled when the mean flow is homogeneous –i.e. there are no gradients of mean flow velocity and density. However, in configurations with highly turbulent flows entropy waves are greatly attenuated [61, 62]. In some cases, entropy waves can even be disregarded when assessing thermoacoustic stability limits [63, 64]. The LEE, Eqs. 2.36-2.38, nonetheless do not include turbulent mixing or diffusion as mechanisms for damping the entropy waves. This provokes that the entropy waves excited in the flame region are advected with the mean flow ultimately leading to, on the one hand, inaccurate density and temperature perturbations after the flame. On the other hand, advected entropy waves that can interact with boundaries downstream of the flame modifying in turn the acoustic propagation.

In order to avoid inaccurate results, the pragmatic solution is to impede entirely the entropy fluctuations by forcing an isentropic solution of the LEE. In that regard, in the next section, a decomposition of the LEE, Eqs. (2.36)-(2.38), into isentropic and non-isentropic parts is carried out. As a result, a set of isentropic LEE is obtained.

2.3.2 Isentropic Formulation of the Linearized Euler Equations

2.3.2.1 Derivation of the Isentropic Linearized Euler Equations

For obtaining an isentropic formulation of the LEE, density is first split into its isentropic and non-isentropic –i.e. excess density– contributions. Excess density ($\hat{\rho}_\mathrm{e}$) is ultimately generated in zones where irreversible processes such as combustion, heat diffusion or turbulent two-phase flows occur [59]. Excess density is simply defined as the difference between density and isentropic density:

$$\hat{\rho}_\mathrm{e} = \hat{\rho} - \hat{\rho}_\mathrm{is} \tag{2.39}$$

where $\hat{\rho}_\mathrm{is}$ represents the isentropic part of the density which contains acoustic perturbations. As $\hat{\rho}_\mathrm{is}$ is isentropic, it is related to the pressure by:

$$\hat{p} = \bar{c}^2 \hat{\rho}_\mathrm{is}. \tag{2.40}$$

Combining Eqs. 2.39 and 2.40, the fluctuating density can be written as a function of excess density and pressure:

$$\hat{\rho} = \frac{\hat{p}}{\bar{c}^2} + \hat{\rho}_\mathrm{e}. \tag{2.41}$$

Inserting Eq. 2.41 into the LEE Eqs. 2.36-2.38 yields:

$$\mathrm{i}\omega\frac{\hat{p}}{\bar{c}^2} + \nabla\cdot\left(\frac{\hat{p}}{\bar{c}^2}\bar{\boldsymbol{u}}\right) + \nabla\cdot(\bar{\rho}\hat{\boldsymbol{u}}) + \underbrace{\mathrm{i}\omega\hat{\rho}_\mathrm{e} + \nabla\cdot(\hat{\rho}_\mathrm{e}\bar{\boldsymbol{u}})}_{=-\hat{S}_\mathrm{m}} = 0, \tag{2.42}$$

$$\mathrm{i}\omega\bar{\rho}\hat{\boldsymbol{u}} + \bar{\rho}\left[(\hat{\boldsymbol{u}}\cdot\nabla)\bar{\boldsymbol{u}} + (\bar{\boldsymbol{u}}\cdot\nabla)\hat{\boldsymbol{u}}\right] + \nabla\hat{p} = 0, \tag{2.43}$$

$$\mathrm{i}\omega\hat{p} + \bar{\boldsymbol{u}}\cdot\nabla\hat{p} = \bar{c}^2\left[\underbrace{\mathrm{i}\omega\hat{\rho}_\mathrm{e} + \nabla\cdot(\hat{\rho}_\mathrm{e}\bar{\boldsymbol{u}})}_{=-\hat{S}_\mathrm{m}} + \bar{\boldsymbol{u}}\cdot\nabla\left(\frac{\hat{p}}{\bar{c}^2}\right)\right] + \ldots$$

$$\ldots\,\bar{c}^2\left[\hat{\boldsymbol{u}}\cdot\nabla\bar{\rho} + \hat{p}\left(\frac{1}{\bar{p}} - \frac{1}{\bar{\rho}\bar{c}^2}\right)(\bar{\boldsymbol{u}}\cdot\nabla\bar{\rho})\right] + (\gamma-1)\hat{q}. \tag{2.44}$$

Note that in Eqs. 2.42-2.44 isobaric combustion has been assumed. This simplification can be applied when mean the flow Mach number is low and implies that gradients of mean pressure are zero –i.e. $\nabla\bar{p} = 0$. Furthermore, isobaric combustion, according to the mean flow momentum equation $(\bar{\boldsymbol{u}}\cdot\nabla)\bar{\boldsymbol{u}} = \nabla\bar{p}$, implies that $(\bar{\boldsymbol{u}}\cdot\nabla)\bar{\boldsymbol{u}} = 0$, which allows to eliminate the term dependent on perturbation density in the linearized momentum Eq. 2.37. Note also that in the continuity Eq. 2.42 and energy Eq. 2.44, all the terms depending on the excess density are gathered in $\hat{S}_\mathrm{m}$ as follows:

$$\hat{S}_\mathrm{m} = -\mathrm{i}\omega\hat{\rho}_\mathrm{e} - \nabla\cdot(\hat{\rho}_\mathrm{e}\bar{\boldsymbol{u}}) \tag{2.45}$$

The term $\hat{S}_\mathrm{m}$ in Eq. 2.45 acts as a source in the continuity equation. After some manipulation, a closed expression for $\hat{S}_\mathrm{m}$, dependent only on primary variables, can be obtained from the energy Eq. 2.44:

$$\hat{S}_\mathrm{m} = \frac{(\gamma-1)}{\bar{c}^2}\hat{q} + \hat{\boldsymbol{u}}\cdot\nabla\bar{\rho} + \frac{\hat{p}}{\bar{p}}\left(\bar{\boldsymbol{u}}\cdot\nabla\bar{\rho}\right). \tag{2.46}$$

Equation 2.46 evidences that not only the unsteady heat release induces non-isentropic density changes. Non-uniform mean flow density fields, second and third terms on the right-hand side of Eq. 2.46, also contribute to the excess density source term. A detailed analysis of the individual terms of Eq. 2.46 is carried

out in Section 2.3.2.2. Summing up, the final set of simplified LEE, which only comprises continuity and momentum equations, is:

$$\mathrm{i}\omega\frac{\hat{p}}{\bar{c}^2} + \nabla\cdot\left(\frac{\hat{p}}{\bar{c}^2}\bar{\boldsymbol{u}}\right) + \nabla\cdot(\bar{\rho}\hat{\boldsymbol{u}}) = \hat{S}_\mathrm{m}, \tag{2.47}$$

$$\mathrm{i}\omega\bar{\rho}\hat{\boldsymbol{u}} + \bar{\rho}\left[(\hat{\boldsymbol{u}}\cdot\nabla)\bar{\boldsymbol{u}} + (\bar{\boldsymbol{u}}\cdot\nabla)\hat{\boldsymbol{u}}\right] + \nabla\hat{p} = 0, \tag{2.48}$$

with $\hat{S}_\mathrm{m}$ given by Eq. 2.46. Equations 2.47-2.48 are isentropic if $\hat{\rho}_\mathrm{e} = 0$ (cf. Eq. 2.41) and excess density is in turn, related to the source term of the continuity equation by definition, Eq. 2.45. Hence, criteria for the applicability of the isentropic assumption can be derived by analyzing $\hat{S}_\mathrm{m}$:

- $\hat{S}_\mathrm{m} = 0$ implies that there is no excess density and therefore Eqs. 2.47-2.48 are isentropic. Density can be recovered from pressure by using the isentropic relation $\hat{\rho} = \hat{p}/\bar{c}^2$. This happens when unsteady heat release and gradients of mean density are absent –i.e. $\hat{q} = 0$ and $\nabla\bar{\rho} = 0$ (cf. Eq. 2.46).
- $\hat{S}_\mathrm{m} \neq 0$ implies that there is excess density and therefore Eqs. 2.47-2.48 are not isentropic. Density does not follow the isentropic relation $\hat{\rho} = \hat{p}/\bar{c}^2$.

Nevertheless, for the case $\hat{S}_\mathrm{m} \neq 0$, isentropicity –i.e. $\hat{\rho} = \hat{p}/\bar{c}^2$– has to be imposed in order to avoid entropy waves. Mathematically, this can be realized only if the continuity source term is a function of pressure and velocity $\hat{S}_\mathrm{m} = \hat{S}_\mathrm{m}(\hat{p}, \hat{\boldsymbol{u}})$, which requires that the unsteady heat release has to be expressed as a function of pressure and velocity $\hat{q} = \hat{q}(\hat{p}, \hat{\boldsymbol{u}})$. When this is fulfilled, Eqs. 2.47-2.48 form a system of equations in which pressure and velocity are the only unknown variables. Density is consequently decoupled and the isentropicity assumption, which is required to avoid the unphysical entropy waves, has then no influence on the pressure and velocity fields. If $\hat{q} \neq \hat{q}(\hat{p}, \hat{\boldsymbol{u}})$ –e.g. $\hat{q} = \hat{q}(\hat{\rho})$– pressure, velocity and density are coupled. Hence, in this case, the full set of LEE, Eqs. 2.36-2.38 has to be solved.

Summarizing, Eqs. 2.47-2.48 deliver accurate pressure and velocity perturbation fields in cases with homogeneous or non-homogeneous mean flow density indistinctly as long as the unsteady heat release is a function of pressure and/or

velocity only. Density perturbations can be correctly retrieved from the isentropic relation $\hat{\rho} = \hat{p}/\bar{c}^2$ only if the gradient of the mean flow density and the unsteady heat release are zero. Otherwise, density and consequently temperature perturbations are not isentropic. All in all, when the LEE are applied to cases with non-homogeneous mean flow density or unsteady heat release a trade-off has to be made. Either the entropy waves are eliminated by imposing the isentropicity condition or the density perturbation fields are accurately calculated. Ideally, in order to capture the real physics, it would be required to have a set of governing equations which treat the flame region, where gradients of mean flow density and unsteady heat release appear in a non-isentropic fashion, but the rest of the domain where they are zero, isentropically. Obtaining such equations is left for future work.

As a last remark concerning Eqs. 2.47-2.48, note that after some manipulation, the isentropic LEE continuity Eq. 2.47 can be operated to recover:

$$\mathrm{i}\omega\hat{p} + \bar{\boldsymbol{u}} \cdot \nabla\hat{p} + \gamma\bar{p}(\nabla \cdot \hat{\boldsymbol{u}}) + \gamma\hat{p}(\nabla \cdot \bar{\boldsymbol{u}}) = (\gamma - 1)\hat{q}. \tag{2.49}$$

Equation 2.49 corresponds to the linearized energy equation written as a function of pressure. Together with the momentum Eq. 2.48 it allows full characterization of the acoustic and vortical propagation as done in Refs. [65, 66] with the previously discussed limitations about obtaining density and temperature perturbation fields. Therefore, the presented derivation of the isentropic LEE can be regarded as a formal proof that the energy pressure Eq. 2.49 can be used together with the momentum Eq. 2.48 to describe isentropic pressure and velocity perturbation fields accurately if $\hat{q} = \hat{q}(\hat{p}, \hat{\boldsymbol{u}})$.

2.3.2.2 Physical Interpretation of Continuity Source Term

In this section the terms responsible for excess density generation are further investigated in order to gain physical understanding of how they work and therefore what their influence on the acoustic modes is.

In order to ease the interpretation, the continuity source term (cf. Eq. 2.46) is first rewritten as a function of the mean heat release as follows. Taking into account

the mean flow energy equation:

$$-\bar{c}^2 \bar{\boldsymbol{u}} \cdot \nabla \bar{\rho} = (\gamma - 1)\bar{q}, \tag{2.50}$$

where isobaric combustion is again assumed, it is shown that the scalar product of mean flow velocity and density is directly proportional to the mean heat release in Eq. 2.50. Thus, the continuity source term can be rewritten as:

$$\hat{S}_\mathrm{c} = \underbrace{\frac{(\gamma - 1)}{\bar{c}^2}\hat{q}}_{\text{Term 1}} + \underbrace{\hat{\boldsymbol{u}} \cdot \nabla \bar{\rho}}_{\text{Term 2}} - \underbrace{\frac{(\gamma - 1)}{\bar{c}^2}\frac{\hat{p}}{\bar{p}}\bar{q}}_{\text{Term 3}}. \tag{2.51}$$

The terms in Eq. 2.51 can be interpreted as:

- Term 1 is directly related to the unsteady heat release. It acts as sink or source of acoustic energy –consequently damping or driving the instabilities– depending on the relative phase of $\hat{p}$ and $\hat{q}$ according to the well-known Rayleigh criterion.
- Term 2 is related to the interaction of perturbation velocity and non-isothermal mean flow fields. In Ref. [67] this term is investigated for the particular case of zero mean flow velocity. There, it is shown that in that scenario despite exciting entropy waves Term 2 does not imply acoustic energy loss, or in other words it neither damps nor drives the instability. Empirically, in the results Chapter 5, it is shown that this term has however a noticeable influence on the acoustic mode propagation, modifying notably the mode shape and the resonant frequency.
- Term 3 is related to interactions between perturbation pressure and mean heat release rate [68]. At first sight, as long as its sign is contrary to the one of Term 1 and is proportional to pressure, it can be concluded from the Rayleigh criterion that it always introduces damping. Furthermore, it is shown later that this term steadily produces entropy along an oscillation cycle. This irreversible entropy production would imply acoustic energy dissipation and therefore explain the damping of the resonant mode.

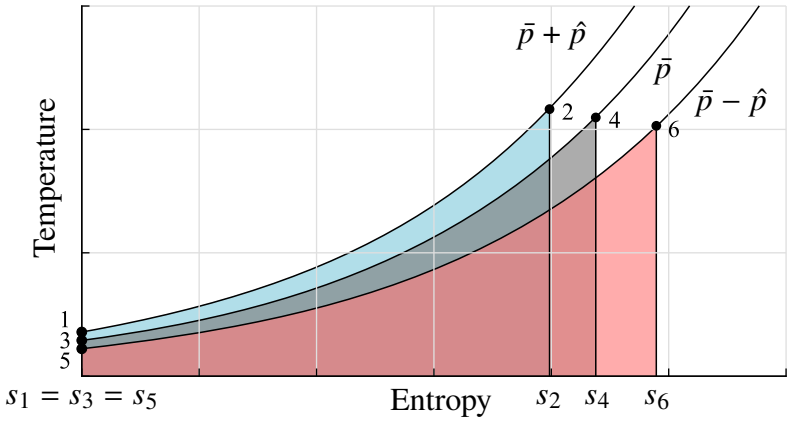

Figure 2.2: *T-s diagram displaying constant mean heat release addition at pressure levels $\bar{p}+\hat{p}$, $\bar{p}$ and $\bar{p}-\hat{p}$.*

Further delving into the physical mechanism of Term 3, with the help of a T-s diagram (cf. Fig. 2.2) it can be demonstrated that constant heat release $\bar{q}$ added at the maximum and minimum pressures of an acoustic wave, $\bar{p}+\hat{p}$ and $\bar{p}-\hat{p}$, generates entropy. Isobar lines $\bar{p}-\hat{p}$ diverge faster from the mean pressure $\bar{p}$ than isobars at $\bar{p}+\hat{p}$. If constant heat is added, the entropy generation between states 6 (at $\bar{p}-\hat{p}$) and 4 (at $\bar{p}$) is larger than the entropy loss that occurs between states 2 (at $\bar{p}+\hat{p}$) and 4 (at $\bar{p}$). This effect can be quantified from first principles (cf. Appendix A), so the net entropy production averaged over one oscillation period is:

$$\frac{\overline{\Delta\hat{s}}}{c_p} = \left(K - \frac{K^2}{2}\right)\left(\frac{\gamma-1}{\gamma}\right)^2 \frac{|\hat{p}|^2}{\bar{p}^2}. \tag{2.52}$$

In Eq. 2.52, K is a constant which depends on mean heat release, heat capacity at constant pressure and unburned mean flow temperature as follows: $K = \bar{q}/(\bar{q} + c_p\bar{T}_\mathrm{u})$. Note that $0 < K < 1$, so the entropy generation is always positive. Finally note also that the entropy increase is a second order quantity with respect to the perturbation pressure. Despite being a second order quantity with respect to the linear perturbations, its effect is still relevant for the damping rates in a linear stability analysis as it will be shown in the results of Chapter 5.

2.3.3 Boundary Conditions for the Linearized Euler Equations

Boundary conditions are required to obtain a particular solution of the LEE. In the following, the boundary conditions employed in this thesis are introduced. Special focus is put on the acoustic boundary layer, as specific boundary conditions are introduced to account for its contribution to the damping in the otherwise inviscid LEE.

2.3.3.1 Impedance Boundary Conditions

Impedance boundary conditions are the most general way of imposing acoustic boundary conditions. Impedances are defined as the ratio between acoustic pressure and acoustic velocity [69]. The acoustic velocity is taken to be perpendicular to the bounding surface and pointing out of the studied control volume:

$$Z(\omega) = \frac{\hat{p}}{\bar{\rho}\bar{c}(\hat{\boldsymbol{u}} \cdot \boldsymbol{n})}. \tag{2.53}$$

The impedance Z is a complex valued function of the frequency. Note that Z is also a non-dimensional quantity as the pressure velocity ratio is divided by $\bar{\rho}\bar{c}$, the so-called characteristic impedance, which is a property of the medium in which the acoustic waves propagate. There are two particular cases of special interest:

- Zero pressure ($Z = 0$): on open boundaries that are connected to infinitely large volumes at constant mean pressure, that mean pressure is imposed as boundary condition. Therefore, $\hat{p} = 0$, which is equivalent to applying $Z = 0$ in Eq. 2.53.
- Rigid wall ($Z \to \infty$): on walls, if viscous and thermal dissipation in acoustic boundary layers are neglected, the velocity is parallel to the wall. Therefore, a slip condition, $\hat{\boldsymbol{u}} \cdot \boldsymbol{n} = 0$, is imposed. This is equivalent to applying $Z \to \infty$ in Eq. 2.53.

2.3.3.2 Energetically Neutral Boundary Conditions

Energetically neutral boundary conditions impose that the acoustic energy flux through boundaries is zero. The acoustic energy flux is intrinsically related to the stability of the system as it modifies the acoustic energy. Setting it to zero ensures that no acoustic energy is lost or gained through the boundaries. Energy flux is the product of fluctuating mass flow rate $\hat{\boldsymbol{m}}$ times fluctuating stagnation enthalpy $\hat{h}_0$ [69]:

$$\boldsymbol{I} = \underbrace{(\bar{\rho}\hat{\boldsymbol{u}} + \hat{\rho}_{\mathrm{is}}\bar{\boldsymbol{u}})}_{=\hat{\boldsymbol{m}}} \underbrace{\left(\frac{\hat{p}}{\bar{\rho}} + \bar{\boldsymbol{u}} \cdot \hat{\boldsymbol{u}}\right)}_{=\hat{h}_0} \tag{2.54}$$

Equation 2.54 shows that a zero acoustic energy flux requires vanishing fluctuating mass flow rate or fluctuating stagnation enthalpy. By setting $\hat{\boldsymbol{m}}$ to zero, the desired boundary condition is obtained:

$$\hat{\boldsymbol{m}} \cdot \boldsymbol{n} = (\bar{\rho}\hat{\boldsymbol{u}} + \hat{\rho}_{\mathrm{is}}\bar{\boldsymbol{u}}) \cdot \boldsymbol{n} = 0. \tag{2.55}$$

2.3.3.3 Zero-Vorticity Boundary Conditions

An irrotational acoustic velocity field is commonly assumed at inlets. Then, fluctuating vorticity ($\hat{\boldsymbol{\Omega}}$) is set to zero:

$$\hat{\boldsymbol{\Omega}} = \nabla \times \hat{\boldsymbol{u}} = 0 \tag{2.56}$$

2.3.3.4 Acoustic Boundary Layer Modeling

The acoustic boundary layer is usually neglected in thermoacoustic studies as it has a negligible effect on the acoustic propagation [70] –i.e. eigenmode shapes and eigenfrequencies. However, it has an influence on damping rates. In particular, acoustic losses due to the acoustic boundary layer grow proportionally to the

square root of frequency and linearly to the surface-to-volume ratio [18, 71]. In the reheat combustion chamber used as benchmark in this thesis, the first transverse eigenmode, which occurs at high-frequency regime is investigated. Additionally, the reheat combustion chamber is relatively flat with high lateral area surface. Therefore, the contribution of the acoustic losses are relevant in this particular case. In order to quantify them, appropriate boundary conditions are introduced. Those can be applied to the LEE and thus account for the acoustic boundary layer without resolving it.

Two different diffusive effects are found in the boundary layer. The first is a thermal effect in which temperature diffuses due to heat transfer from the fluctuating stream to the walls (or vice versa). It can be cast into an impedance form [69]:

$$Z_{\mathrm{th}} = \frac{(1-\mathrm{i})\,\bar{c}}{(\gamma-1)\omega\delta_{\mathrm{th}}}, \tag{2.57}$$

where δ_{th} stands for the thermal boundary layer thickness, which is defined as follows:

$$\delta_{\mathrm{th}} = \sqrt{\frac{2k}{\bar{\rho}\omega c_p}}. \tag{2.58}$$

Compared to the usual slip wall boundary condition, $\hat{\boldsymbol{u}} \cdot \boldsymbol{n} = 0$, for which $Z \to \infty$, Z_{th} can be regarded as a "softened" wall boundary condition. In other words, due to the smallness of δ_{th} the value of Z_{th} is large, but still finite.

The second effect that damps acoustic energy is diffusion of velocity due to viscous dissipation. In this case, as the acoustic velocity is a vector for the multidimensional eigenmodes that occur at high frequencies, its direction has to be taken into account, precluding its formulation as an impedance. Nevertheless its influence can be expressed as a boundary condition which depends on the fluctuating normal velocity to walls:

$$\hat{u}_n = \hat{\boldsymbol{u}} \cdot \boldsymbol{n} = -(\nabla_{\boldsymbol{s}} \cdot \hat{\boldsymbol{u}}_\infty)\,\delta_{\mathrm{v}} \left(\frac{\mathrm{i}-1}{2}\right), \tag{2.59}$$

where $\nabla_s \cdot$ denotes the divergence in the directions tangential to the wall. A formal derivation of Eq. 2.59 is carried out in Appendix B. The viscous boundary layer thickness is represented by δ_v [69] and defined as:

$$\delta_\mathrm{v} = \sqrt{\frac{2\nu}{\omega}}. \tag{2.60}$$

By comparing Eq. 2.59 to the usual slip wall condition $\hat{\boldsymbol{u}} \cdot \boldsymbol{n}$, it can be observed that the boundary condition 2.59 induces a small normal velocity. The normal velocity can be at the same time related to an acoustic flux from which acoustic losses stem.

2.3.4 Numerical Discretization of Linearized Euler Equations

The isentropic LEE in frequency domain (cf. Eqs. 2.47 - 2.48) together with corresponding boundary conditions are discretized using a stabilized Finite Element Method (FEM). Interested readers are referred to [40, 47] for further information on stabilized FEM. FEM is easily applicable to unstructured meshes suitable for discretizing complex geometries. However, FEM based on Galerkin finite element approximations lacks numerical stability when diffusive terms of the governing equations are small compared to convective terms. In that case, spurious solutions are obtained. This issue is overcome by adding artificial viscosity that numerically stabilizes the solution [47]. In this thesis, Streamline Upwind Petrov-Galerkin (SUPG) stabilization is used. SUPG only acts on the convective operator, therefore only adds artificial diffusion along the mean flow streamlines [47]. There are a number of different stabilization techniques, among them one of the most popular is the so-called Galerkin Least Squares (GLS) method. GLS is equivalent to SUPG when using linear elements [72], as done in this thesis, so GLS shall not be further discussed here. The full set of isentropic LEE (cf. Eqs. 2.47 - 2.48) with their corresponding SUPG stabilization, can be found in Appendix D. Note that these are expressed in weak form, which is required to implement them in FEM. The weak-form equations are solved by an in-house implementation in the "Weak Form PDE" module of the commercial FEM solver

COMSOL Multiphysics® [73].

2.4 Thermoacoustic Coupling of Flame and Acoustics in the High-Frequency Regime

The coupling models between acoustics and unsteady heat release that are employed in the present work are introduced in this section. First, displacement and deformation mechanisms are briefly presented. Second, the acoustic modulation due to convective effects at the reactive shear layer is introduced. Finally, the acoustic modulation of the auto-ignition time delay is presented.

2.4.1 Coupling due to Displacement and Deformation of the Flame

In the high-frequency regime an oscillatory motion of the flame in phase with the pressure is observed in swirl stabilized flames [16, 29]. From that experimental evidence, two different models for the flame-acoustics coupling, displacement and deformation, are derived in form of thermoacoustic source terms in Ref. [15]. It is expected that both mechanisms contribute to the driving potential of reheat flames [28]. The first mechanism is the so-called displacement mechanism, by which acoustic velocity fluctuations move the flame away from its stationary position. For a transverse mode[viii] the maximum displacement occurs at the pressure node and is in phase with the pressure. The modulation of the unsteady heat release due to the flame displacement ($\hat{q}_\Delta$) can be described with the following expression:

$$\hat{q}_\Delta = -\frac{\hat{\boldsymbol{u}}}{\mathrm{i}\omega} \cdot \nabla \bar{q}. \tag{2.61}$$

The displacement mechanism intrinsically causes the second mechanism, the so-called deformation mechanism [15]. The movement of the flame towards acoustic pressure nodes or anti-nodes induces local compression or expansion of the flame

[viii] A transverse mode is an eigenmode whose main direction is perpendicular to the mean flow main direction

heat release ultimately provoking a modulation on it. The unsteady heat release due to the deformation mechanism ($\hat{q}_\rho$) can be mathematically expressed as

$$\hat{q}_\rho = \frac{\bar{q}}{\bar{\rho}}\hat{\rho}. \tag{2.62}$$

If isentropic acoustics is assumed (cf. Sect. 2.3.2), $\hat{\rho}$ can be substituted by $\hat{p}/\bar{c}^2$ in Eq. 2.62, finally yielding:

$$\hat{q}_\rho = \frac{\bar{q}}{\gamma\bar{p}}\hat{p}. \tag{2.63}$$

Note that the basic input quantity for both source terms is the mean heat release field ($\bar{q}$). In the deformation model γ and $\bar{p}$ have to be provided as well.

2.4.2 Coupling due to Convective Modulation of the Reactive Shear Layer

Experimental observations of unsteady heat release fluctuations for the T1 eigenmode of lab-scale reheat combustion chambers revealed a convective modulation of heat release in the reactive shear layers [31]. This was also observed in LES simulations of high frequency flame dynamics in reheat combustors [28]. The heat release modulation may be caused by the acoustically induced vortex shedding that occurs at the sudden area expansion. More specifically, vortices would transport hot combustion products into the cold reactants and vice versa. Consequently, the reaction is locally sped up or slowed down and heat release is modulated. Analogous vortex shedding patterns had also been discovered in swirl-stabilized flames. However, these did not lead to significant thermoacoustic driving because the flame is heavily quenched in the shear layers due to high stretch rates of this configuration [29, 34]. In that case, vortex shedding only contributes to acoustic damping [33].

Another possible explanation for the shear layer modulation is convective modulation of equivalence ratio fluctuations [31]. Equivalence ratio fluctuations can

arise due to acoustic modulation of fuel injection. This is discarded in the current work, as no significant acoustic disturbances reach the injection port due to the cut-off of the T1 eigenmode at the area jump of the chamber inlet. Yet another possible cause for the observed heat release modulation is that significant unmixedness of fuel and oxidant exists at the shear layer. Then, vortex shedding would locally modulate the mixing process, which in turn would modulate heat release. Nevertheless, this is not considered in the current work, in which a premixed framework is presumed (cf. Section 4.2). Therefore, the influence of equivalence ratio fluctuations is neglected. Investigations on the actual influence of equivalence ratio fluctuations are left to future work. Summing up, within the current premixed framework, modulation of the reactive shear layer is ascribed to vortical transport of hot products and cold reactants. This effect is modeled in detail below.

In premixed combustion, the progress variable determines which parts of the gas are burned or unburned. By analyzing the interactions between the acoustically induced vortex shedding and the progress variable it is possible to reproduce the effect of the vortical transport on unburned and burned gases. Furthermore, progress variable is directly linked to heat release through the mean reaction rate (cf. Eqs. 2.17 and 2.22). This ultimately allows to express the unsteady heat release fluctuations in the shear layer as a function of the progress variable fluctuations.

The first step to obtaining a closed expression for the unsteady heat release fluctuations is to linearize the progress variable transport Eq. 2.13. Under the assumption of negligible viscosity and harmonic acoustic motions, a linearized transport equation for the progress variable is obtained:

$$\mathrm{i}\omega\bar{\rho}\hat{c} + \bar{\rho}(\bar{\boldsymbol{u}} \cdot \nabla\hat{c} + \hat{\boldsymbol{u}} \cdot \nabla\bar{c}) + \hat{\rho}(\bar{\boldsymbol{u}} \cdot \nabla\bar{c}) = \bar{\dot{\omega}}'_{c,\mathrm{pr}}, \tag{2.64}$$

where the linearized mean reaction rate is obtained by linearizing Eq. 2.22:

$$\bar{\dot{\omega}}'_{c,\mathrm{pr}} = \frac{g\rho_\mathrm{u}s_\mathrm{L}^0}{\sigma_y L_y}(1+\tau_\rho)\frac{1-\bar{c}(2+\tau_\rho)}{(1+\tau_\rho\bar{c})^3}\hat{c} \tag{2.65}$$

Notice that in Eq. 2.65, the laminar flame speed is constant. Hence, the possible influence of acoustics on the laminar flame speed is neglected. This could be potentially addressed in future work by linearizing correlations of laminar flame speed with temperature, pressure and composition as proposed in [44]. Also, the possible influence of perturbation vortical velocity on burning speed can be investigated by using Helmholtz decomposition of acoustic and vortical fields as shown in [74]. Finally, the linearized unsteady heat release can be obtained by linearizing the mean heat release (cf. Eq. 2.17) yielding:

$$\hat{q}_{c,\mathrm{pr}} = Y_{\mathrm{f,u}} LHV \bar{\dot{\omega}}'_{c,\mathrm{pr}} \tag{2.66}$$

where $Y_{\mathrm{f,u}}$ is the unburned fuel mass fraction and LHV is the lower heating value. Both are regarded as constant under the premixed assumption.

Acoustic modulation of the propagation mean reaction rate in the shear layer is independent from the deformation and displacement mechanisms introduced in Section 2.4.1. The latter mechanisms arise ultimately from the acoustic velocity fluctuations that move the flame transversally for the studied T1 mode, modulating the unsteady heat release in the process. Therefore, below it is shown that the linearization of the BML model is independent from acoustic velocity and consequently, independent from deformation and displacement mechanisms. The starting point is linearization of BML's mean reaction rate, which is directly proportional to mean heat release, given by Eq. 2.18:

$$\frac{\hat{q}_{c,\mathrm{pr}}}{\bar{q}_{c,\mathrm{pr}}} = \frac{\hat{\rho}_{\mathrm{u}}}{\bar{\rho}_{\mathrm{u}}} + \frac{\langle \hat{s}_{\mathrm{c}} \rangle_s}{\langle \bar{s}_{\mathrm{c}} \rangle_s} + \frac{\hat{\Sigma}}{\bar{\Sigma}}. \tag{2.67}$$

In Eq. 2.67, first addend on the RHS is zero as unburned density is constant under the assumption of premixed combustion. Second addend, the burning speed, is also deliberately taken as constant so its linearization is zero. For modeling the influence of perturbation velocity on linearized burning speed, a similar modeling approach to that followed by Hofmeister in [74] could be employed. The only remaining term is the linearization of the flame surface density. In the BML model this term is a function of progress variable only, cf. for example Eq. 2.65. As a result, the modeled coupling mechanism between acoustics and reaction

shear layer is independent from velocity. Physically, this can be interpreted as the flame moves following the velocity perturbation but its inner structure does not change.

2.4.3 Coupling due to Acoustic Modulation of the Auto-Ignition Time Delay

In this section a mechanism of acoustic modulation of the auto-ignition stabilized flame front is presented. First, the modulation of time delay that leads to flame front displacement is introduced. Subsequently, a relation between the flame displacement and the unsteady heat release is derived.

2.4.3.1 Unsteady Flame Front Displacement

The key quantity that characterizes auto-ignition is the auto-ignition time delay. This accounts for the induction time elapsed between fuel injection and the formation of a definite auto-ignition stabilized flame front. The auto-ignition time delay is essentially a function of temperature and density following an Arrhenius-like law, cf. Eq. 2.26. Therefore, fluctuations of those variables along a fluid particle's flight path from injection to the flame front lead to modulation of the auto-ignition time delay, which in turn modifies the flame front position, ultimately modulating the unsteady heat release.

An equation that captures the history of auto-ignition time delay oscillations of fluid particles along their flight path on a streamline can be written as:

$$\frac{\mathrm{D}t'_{\mathrm{ign,p}}}{\mathrm{D}t} = \frac{\partial t'_{\mathrm{ign}}}{\partial t}, \tag{2.68}$$

where the material derivative is defined with respect to the mean flow velocity as $\mathrm{D}(\cdot)/\mathrm{D}t = \partial(\cdot)/\partial t + \bar{\boldsymbol{u}} \cdot \nabla(\cdot)$. By using the material derivative, the history of time delay fluctuations of every fluid particle $t'_{\mathrm{ign,p}}$ is accounted for in a Lagrangian sense. Therefore, $t'_{\mathrm{ign,p}}$ can be interpreted as a cumulative time delay that adds up local time delay oscillations t'_{ign} along the streamlines. Notice that

it is assumed that streamlines are not modified by the acoustic velocity field, so acoustic particles travel on mean flow streamlines only.

As hinted before, modulation of auto-ignition time delay modifies the position of the flame, so the next step is to determine the relation between flame position and auto-ignition time delay. The flame position is directly related to velocity and the cumulative auto-ignition time delay through the following integral equation:

$$\boldsymbol{x}_\mathrm{f} = \int_0^{t_\mathrm{ign,p}} \boldsymbol{u}\,\mathrm{d}t \tag{2.69}$$

Equation 2.69 shows that the flame front position ($\boldsymbol{x}_\mathrm{f}$) can be obtained by time-integrating the velocity until the cumulative auto-ignition time is reached. It is important to remark here that $\boldsymbol{x}_\mathrm{f}$, despite its name, is a field variable and it is thus not only defined at the flame front. The field of perturbations of $\boldsymbol{x}_\mathrm{f}$ can be retrieved after applying substantial derivation and linearization on Eq. 2.69, yielding:

$$\frac{\mathrm{D}\boldsymbol{x}'_\mathrm{f}}{\mathrm{D}t} = \boldsymbol{u}' + \bar{\boldsymbol{u}}\frac{\mathrm{D}t'_\mathrm{ign,p}}{\mathrm{D}t}. \tag{2.70}$$

Equation 2.70 describes the flame front position perturbation field. Inserting Eq. 2.68 in Eq. 2.70, the substantial derivative on the RHS of Eq. 2.68 can be eliminated and therefore, the former is further simplified:

$$\frac{\mathrm{D}\boldsymbol{x}'_\mathrm{f}}{\mathrm{D}t} = \boldsymbol{u}' + \bar{\boldsymbol{u}}\frac{\partial t'_\mathrm{ign}}{\partial t}. \tag{2.71}$$

As done before, harmonic acoustic motion is assumed, cf. for example Eq. 2.35, transforming time dependency into frequency domain. As a result, Eq. 2.71 is transformed into:

$$\mathrm{i}\omega\hat{\boldsymbol{x}}_\mathrm{f} + \bar{\boldsymbol{u}}\cdot\nabla\hat{\boldsymbol{x}}_\mathrm{f} = \hat{\boldsymbol{u}} + \mathrm{i}\omega\bar{\boldsymbol{u}}\hat{t}_\mathrm{ign}. \tag{2.72}$$

Note that there are no diffusion terms in Eq. 2.72 as those have been neglected

in this derivation. Thus, acoustic oscillations occur in an inviscid fashion as commonly assumed in thermoacoustics. The RHS of Eq. 2.72 corresponds to a linearized source term depending on acoustic velocity $\hat{\boldsymbol{u}}$ fluctuations and oscillations of the ignition time delay $\hat{t}_{\mathrm{ign}}$ multiplied by the mean flow velocity. Closed expressions for $\hat{t}_{\mathrm{ign}}$, and therefore for the linearized source term of Eq. 2.72 which only depend on acoustic variables are derived below.

Dependency of the auto-ignition time delay on temperature and fuel composition is modeled using the empirical correlation developed by Spadaccini and Kolket [58] and described in Eq. 2.26. Equation 2.26 can be linearized around the mean temperature and density resulting in

$$\hat{t}_{\mathrm{ign}}\left(\hat{T},\hat{\rho}\right) = K_1 \exp\left(\frac{E_{\mathrm{a}}}{R\bar{T}}\right)\bar{\rho}^{-0.78}\left[\left(-\frac{E_{\mathrm{a}}}{R\bar{T}}\right)\frac{\hat{T}}{\bar{T}} - 0.78\frac{\hat{\rho}}{\bar{\rho}}\right] \tag{2.73}$$

note that $K_1 = 1.77\times10^{-14}\left(Y_{\mathrm{O_2}}/W_{\mathrm{O_2}}\right)^{-1.05}\left(Y_{\mathrm{CH_4}}/W_{\mathrm{CH_4}}\right)^{0.66}\left(Y_{\mathrm{HC}}/W_{\mathrm{HC}}\right)^{-0.39}$ is a constant that comprises the premultiplier of the exponential function as well as mass fractions of the fuel mixture, which remain constant for premixed combustion.

Once a linearized expression for $\hat{t}_{\mathrm{ign}}$ is available, the order of magnitude of the flame front displacement can be estimated with Eq. 2.68. This serves as first proof of correctness of such an equation. Starting off with an estimation of the experimental value of pressure oscillations, which correspond to a pressure ratio $\hat{p}/\bar{p} \approx 0.5\,\%$, the auto-ignition time delay can be estimated. By using Eq. 2.73 under the assumption of isentropic pressure oscillations, a ratio of $\hat{t}_{\mathrm{ign}}/\bar{t}_{\mathrm{ign}} \approx 2.5\,\%$ is obtained, which in turn can be translated to $\hat{t}_{\mathrm{ign}} \approx 1.6\times10^{-4}\,\mathrm{s}$ for the auto-ignition time delay fluctuations. Both terms on LHS of transport of $\hat{\boldsymbol{x}}_{\mathrm{f}}$ Eq. 2.70 have the same order of magnitude: $\mathrm{O}(f\hat{x}_{\mathrm{f}})$. On the RHS of Eq. 2.70, perturbation velocity can be estimated based on pressure using the momentum Eq. 2.37 as follows:

$$\hat{u} \approx \frac{\hat{p}}{L_x}\frac{1}{f\bar{\rho}}, \tag{2.74}$$

where $L_x \approx 0.5\,\mathrm{m}$ is a characteristic length in x-direction, which is taken as first approximation as the chamber length. Therefore, by substituting numerical values in Eq. 2.74 ($f \approx 1600\,\mathrm{Hz}$ and $\bar{\rho} \approx 0.3\,\mathrm{kg\,m^{-3}}$) it is obtained $\hat{u} \approx 2\,\mathrm{m\,s^{-1}}$. This quantity is small compared with the second addend in the RHS of Eq. 2.70, which has a order of magnitude $\bar{u} f \hat{t}_{\mathrm{ign}} \approx 25\,\mathrm{m\,s^{-1}}$ for $\bar{u} = 100\,\mathrm{m\,s^{-1}}$. Finally, the displacement in x-direction can be estimated by comparing order of magnitude in LHS and RHS of Eq. 2.70. Thus, $\hat{x}_{\mathrm{f}} \approx \bar{u}\hat{t}_{\mathrm{ign}} \approx 1.6 \times 10^{-2}\,\mathrm{m}$. This length is comparable to the convective wavelength, $\lambda_{x,c} = \bar{u}/f \approx 6 \times 10^{-2}\,\mathrm{m}$.

The transport Eq. 2.72 for flame front displacement together with the isentropic LEE (Eqs. 2.47-2.48) describe a fluctuating flame front displacement field. Still a relationship between the displacement field and the unsteady heat release is necessary in order to close the continuity Eq. 2.47.

2.4.3.2 Unsteady Heat Release Associated with Flame Displacement

The volumetric heat released by a flame is proportional to the product of density (ρ), flame speed (s) and lower heating value (LHV):

$$q \propto \rho s LHV. \tag{2.75}$$

Note that for the time being, Eq. 2.75 represents just a one-dimensional movement. Equation 2.75 can be linearized under the assumption that the lower heating value is constant, yielding:

$$\frac{\hat{q}}{\bar{q}} = \frac{\hat{\rho}}{\bar{\rho}} + \frac{\hat{s}}{\bar{s}} \tag{2.76}$$

In Eq. 2.76 harmonic oscillations have been already assumed. The flame front speed can be expressed as function of the fluid velocity and the flame front position by the following kinematic relation:

$$\hat{s} = \hat{u} - \frac{\partial \hat{x}_{\mathrm{f}}}{\partial t} \tag{2.77}$$

Until now the derivation has been carried out for just one dimension. The resulting Eqs. 2.76 and 2.77 can be understood as the velocity follows always the direction of a mean flow streamline. This is in line with the assumption made for deriving Eq. 2.68 by which all movement occurs in mean flow velocity direction only. In order to obtain a more general solution which is implementable into the numerical solver, the one-dimensional expression valid for a streamline has to be generalized to three dimensions. This is accomplished by exploiting the definition of the local flame speed along the streamline, which can written in vector form as follows:

$$\hat{s} = \hat{\boldsymbol{s}} \cdot \frac{\bar{\boldsymbol{u}}}{\|\bar{\boldsymbol{u}}\|} = \left(\hat{\boldsymbol{u}} - \frac{\partial \hat{\boldsymbol{x}}_f}{\partial t} \right) \cdot \frac{\bar{\boldsymbol{u}}}{\|\bar{\boldsymbol{u}}\|}. \tag{2.78}$$

In Eq. 2.78, the module of the flame speed vector is expressed as the dot product of flame speed vector and the unit mean flow velocity vector. This operation is just the vector projection of the flame speed vector onto a streamline, characterized by its direction vector given by the mean flow velocity direction. Therefore, dependency on flame speed in Eq. 2.76 can be eliminated by inserting Eq. 2.78 into 2.76, resulting in:

$$\frac{\hat{q}_{\mathrm{ai}}}{\bar{q}_{\mathrm{ai}}} = \frac{\hat{\rho}}{\bar{\rho}} + \left(\hat{\boldsymbol{u}} - \frac{\partial \hat{\boldsymbol{x}}_f}{\partial t} \right) \cdot \frac{\bar{\boldsymbol{u}}}{\|\bar{\boldsymbol{u}}\|^2}, \tag{2.79}$$

which is the final expression of the unsteady auto-ignition heat release. Note that in Eq. 2.79, $\bar{s}$ has been eliminated under the assumption of the mean flow flame position being fixed and hence $\bar{\boldsymbol{s}} = \bar{\boldsymbol{u}}$.

3 Reheat Combustor Experimental Setup

This chapter briefly introduces the two-stage experimental setup used as validation for the numerical results in this thesis. The test rig is composed of two sequential atmospheric combustion stages: a primary combustion stage, denominated vitiator, and a secondary reheat combustor. Comprehension and modeling of flame dynamics of that secondary stage is the goal of the investigation carried out in the current work. A detailed analysis of the setup, its capabilities and experimental results ranging from dynamic pressure measurements to flame dynamics can be found in [30, 31].

A schematic of the vitiator is depicted in Fig. 3.1. It comprises six lean premixed, swirl and bluff-body stabilized burners and an air dilution stage. Electrically preheated air enters the plenum and is evenly distributed to all burners. Natural gas is injected into the preheated air stream at the burner entry. Both streams are mixed and passed through a swirler after which the flame is stabilized.

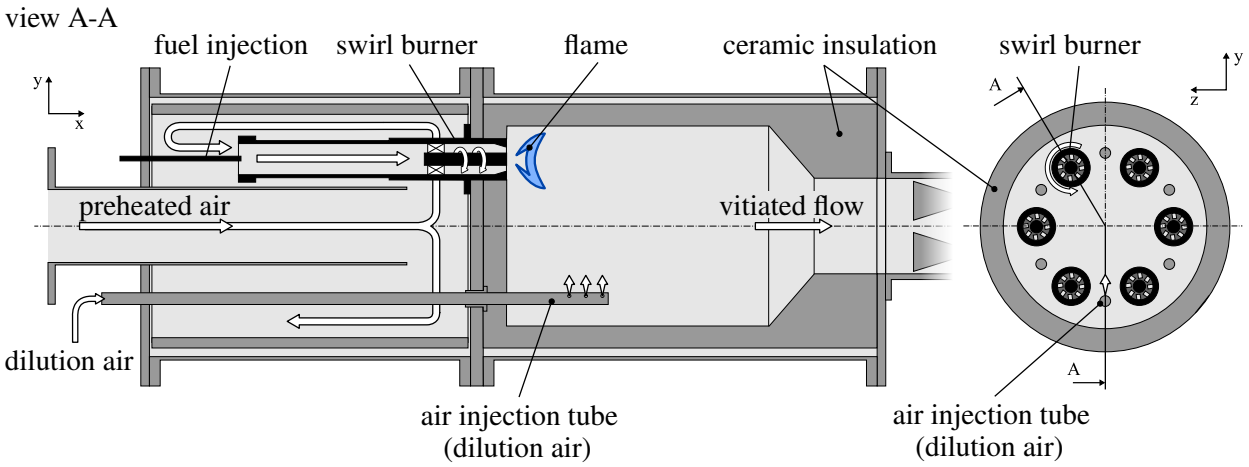

Figure 3.1: *Lateral and section views of the vitiator. Adapted from [30].*

Post-flame temperature can be reduced to adequate reheat inlet temperatures by adding dilution air. The hot vitiated flow is directed to the mixing section, which features four delta wings that generate counter-rotating vortices for improving the fuel-vitiated-air mixing (cf. view A-A in Fig. 3.2). The secondary fuel injection port is located right after the delta wings downstream tip in a jet-in-cross-flow configuration. Turbulence introduced by the vortex generators ensures that the fuel is well-mixed within short distances. In addition to the fuel, shielding air is injected. This serves as mixing enhancer as it optimizes the momentum ratio of the fuel-shielding air mixture to the vitiated flow. Finally, the fuel-enriched mixture reaches the combustion chamber where a reheat flame is stabilized. Reheat flames at atmospheric pressure characteristically present (i) a mean core flow stabilized by auto-ignition and (ii) areas towards the corner recirculation zones predominantly stabilized by propagation. This mimics reheat flames of industrial reheat combustors such as the Ansaldo GT26 or GT36 [9, 12].

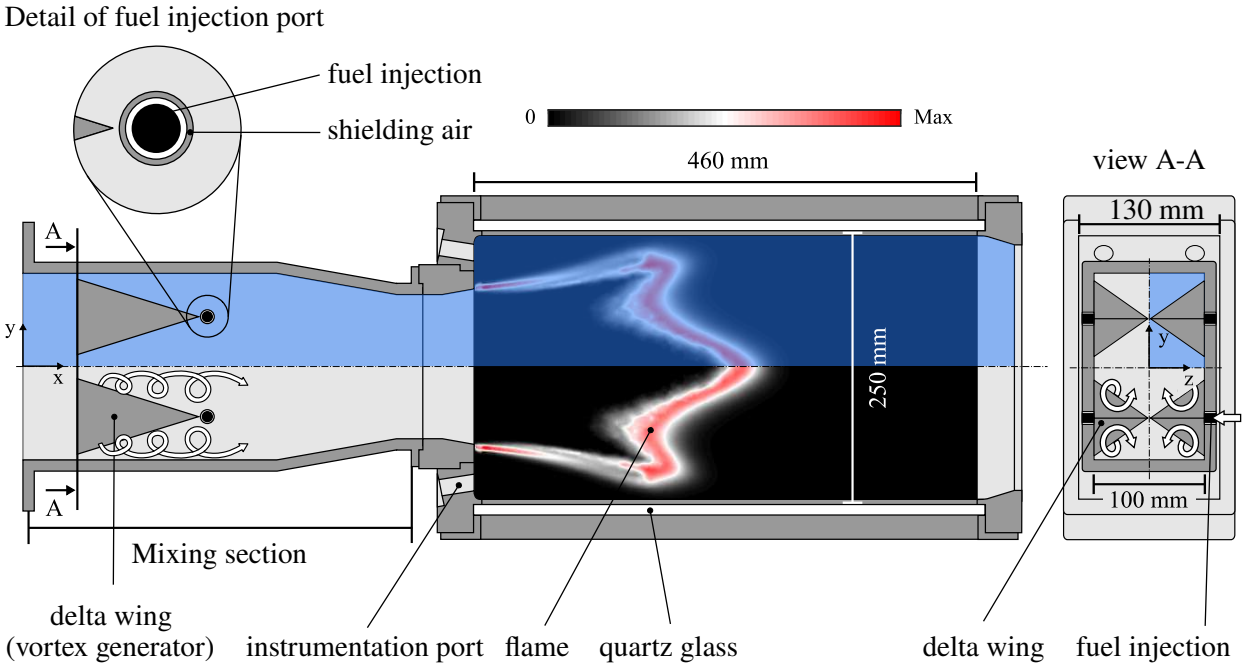

Figure 3.2: *Lateral and section views of the reheat stage with a characteristic simulated heat release field. Dimensions of the prismatic sequential chamber are 460x250x130 mm. The computational domain is highlighted in blue. Adapted from [30].*

The computational domain of the CFD calculations exploits symmetry in y- and z-directions of the secondary combustion chamber and therefore only comprises a quarter of the chamber (cf. highlighted zones in blue in Fig. 3.2).

4 Reactive Mean Flow Simulations

In this chapter, the procedure followed for the reactive CFD simulations is introduced first. This procedure comprises two steps: isothermal mixing and premixed combustion. Corresponding results for each step are shown and discussed. Additionally, simulated heat release distributions from the premixed combustion step are compared to experimental CH^* chemiluminescence images.

4.1 CFD Procedure

The employed CFD strategy is summarized in Fig. 4.1.

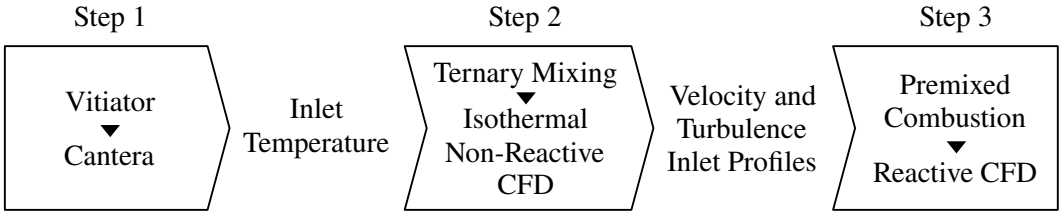

Figure 4.1: *Flow chart of the CFD procedure.*

In a first step, the vitiator is characterized. To do so, outlet temperature, composition mass fractions and transport properties of the vitiated stream are estimated using Cantera [75]. These serve as inlet conditions for the second step, in which the ternary mixing of the vitiated hot stream, fuel and shielding air is carried out. This is accomplished via RANS simulations under isothermal conditions. A quarter of the entire reheat combustor geometry including the mixing section, which comprises the delta wings vortex generators and the fuel injection port is simulated, cf. Fig. 3.2. This intermediate step of solving the ternary mixing is required because if a premixed mixture is introduced in the reheat combustor

geometry with the mixing section, the flame would stabilize in the wake of the vortex generators due to the high turbulence levels occurring there. Velocity as well as turbulent kinetic energy and turbulent dissipation profiles obtained from the non-reactive mixing simulations are extracted at the end of the mixing section, cf. Fig. 3.2. The extracted profiles are used as inlet boundary conditions for the final step in which reheat premixed combustion is simulated. Combustion is modeled with suitable models for the characteristic propagation and auto-ignition stabilized zones of reheat flames that were introduced in Section 2.2.

4.2 Ternary Mixing

4.2.1 Numerical Setup

Before starting with the simulations of the ternary mixing, the first step is to determine the inlet conditions of the vitiated flow. To do so, combustion and subsequent air dilution in the vitiator is simulated using Cantera. For a given excess air ratio of the vitiator (λ_{EV}), cf. in the operating points listed in Tab. E.1 of Appendix E, the adiabatic flame temperature is obtained. Specifically, zero-dimensional perfectly stirred reactors for 8 species (CH_4, C_2H_6, C_3H_8, N_2, O_2, CO_2, H_2O) with the GRI 3.0 mechanism [76] are employed for the Cantera simulations. After simulating the adiabatic combustion in the vitiator, the products of combustion are mixed at constant pressure and enthalpy with the staging air, reducing the adiabatic flame temperature. The obtained temperature as well as thermal and transport properties of the vitiated mixing such as constant pressure heat capacity, thermal conductivity and viscosity are used as inputs for the isothermal CFD simulations of the ternary mixing.

The ternary mixing simulations are carried out using a quarter of the full geometry which includes the vortex generators and the fuel injection port, cf. Fig. 4.2. The geometry is discretized using a non-structured tetrahedral mesh, cf. Fig. 4.2. The mixing section and the area jump are further refined in order to capture the intense turbulence in those areas. At the walls, a prismatic boundary-layer mesh is employed. A summary of the mesh properties is listed in Tab. 4.1.

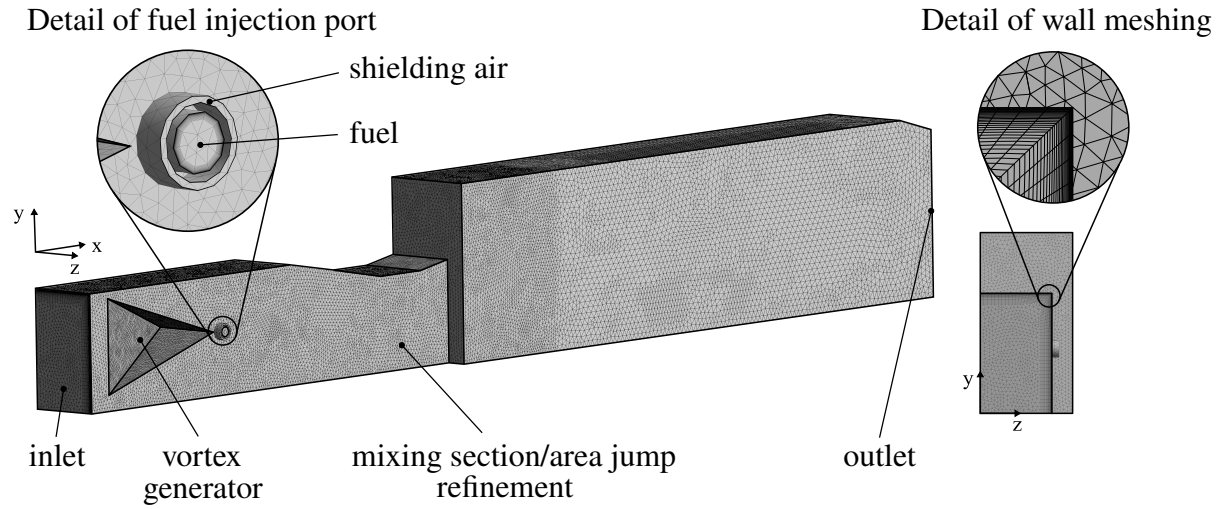

Figure 4.2: *Mesh of ternary mixing configuration.*

Table 4.1: *Summary of mesh properties for mixing configuration.*

Size	Size refinement	No. of layers prismatic mesh	Height 1stelement prismatic mesh	Growth rate prismatic mesh	No. elements
4 mm	2.5 mm	30	0.05 mm	1.10	2.3×10^6

To simulate the mixing of fuel, shielding air and the vitiated flow from the vitiator, isothermal RANS simulations with the realizable k-ε turbulence closure are carried out, cf. Section 2.2.1. At the inlets the corresponding mass flows and temperature of each stream are prescribed. The near-wall areas are modeled with wall functions, specifically the Enhanced Wall Treatment from Fluent [53] is used. The turbulent Schmidt number is set to 0.2, which increases the turbulent mass diffusion with respect to the usual value $Sc_t = 0.7$. The value $Sc_t = 0.2$ is recommended for best agreement of k-ε RANS simulations to experiments in jet-in-crossflow configurations where jet-to-crossflow momentum flux ratios are relatively small, as it is the case for the reheat combustor [77]. Numerically, a coupled velocity-pressure solver is employed with second order spatial discretization. Convergence of the solution is assumed when the residua reach levels of 1×10^{-5}. Furthermore, mass conservation is checked: the net balance of inlet/outlet mass flows through the system open boundaries is of order $1 \times 10^{-9}\,\mathrm{kg\,s^{-1}}$. Mesh independence is ensured by carrying out additional simulations with 1.4×10^6 and 3.5×10^6 cells. Details of the mesh independence study are presented in Appendix

F.1.

4.2.2 Results

Computed mean flow velocity in x-direction and fuel mass fraction are shown in Fig. 4.3. Velocity fields depicted in Fig. 4.3 a) display the flow topology, whereas fuel mass fraction serves as an indicator for the fuel-vitiated air mixing quality, cf. Fig. 4.3 b).

Figure 4.3 a) shows a strong recirculation zone after the area jump. This is formed as a result of two effects. The first effect is the flow separation at the angled diffusor, which is optimized to reinforce the recirculation zones [30]. Second, the recirculation zones are further reinforced and shortened in longitudinal direction by the effect of the vortex generators, which introduce a strong secondary flow pattern, cf. planes A-A, B-B and C-C in Fig. 4.3 a). As a result, shear layers between the bulk flow and the recirculation zones form after the area jump. These shear layers allow for flame stabilization via propagation.

Fuel mass fraction is shown in Fig. 4.3 b). The main outcome is that a homogeneous distribution is obtained within short distances, or respectively short time-delays. The secondary flow pattern induced by the vortex generators (cf. Fig. 4.3 a)) distributes the fuel over the entire channel cross section. Subsequently, turbulence homogenizes the fuel-vitiated air mixture. The evolution of the mixture history along the mixing tube, cf. cutting planes A-A, B-B and C-C in Fig. 4.3 b), proves that homogeneity is obtained within short distance of about 0.2 m from the fuel injection. Therefore, the assumption of premixed conditions before reaching the reheat combustion chamber is corroborated. Ultimately, the homogenized mixture leads to a homogeneous auto-ignition core flow as auto-ignition preferably occurs at locations close to the most reactive mixture. In reheat combustors, this happens at lean conditions due to the high temperature of the vitiated stream [51]. The homogeneous mixture within the chamber is a sign of high reactivity and therefore of auto-ignition.

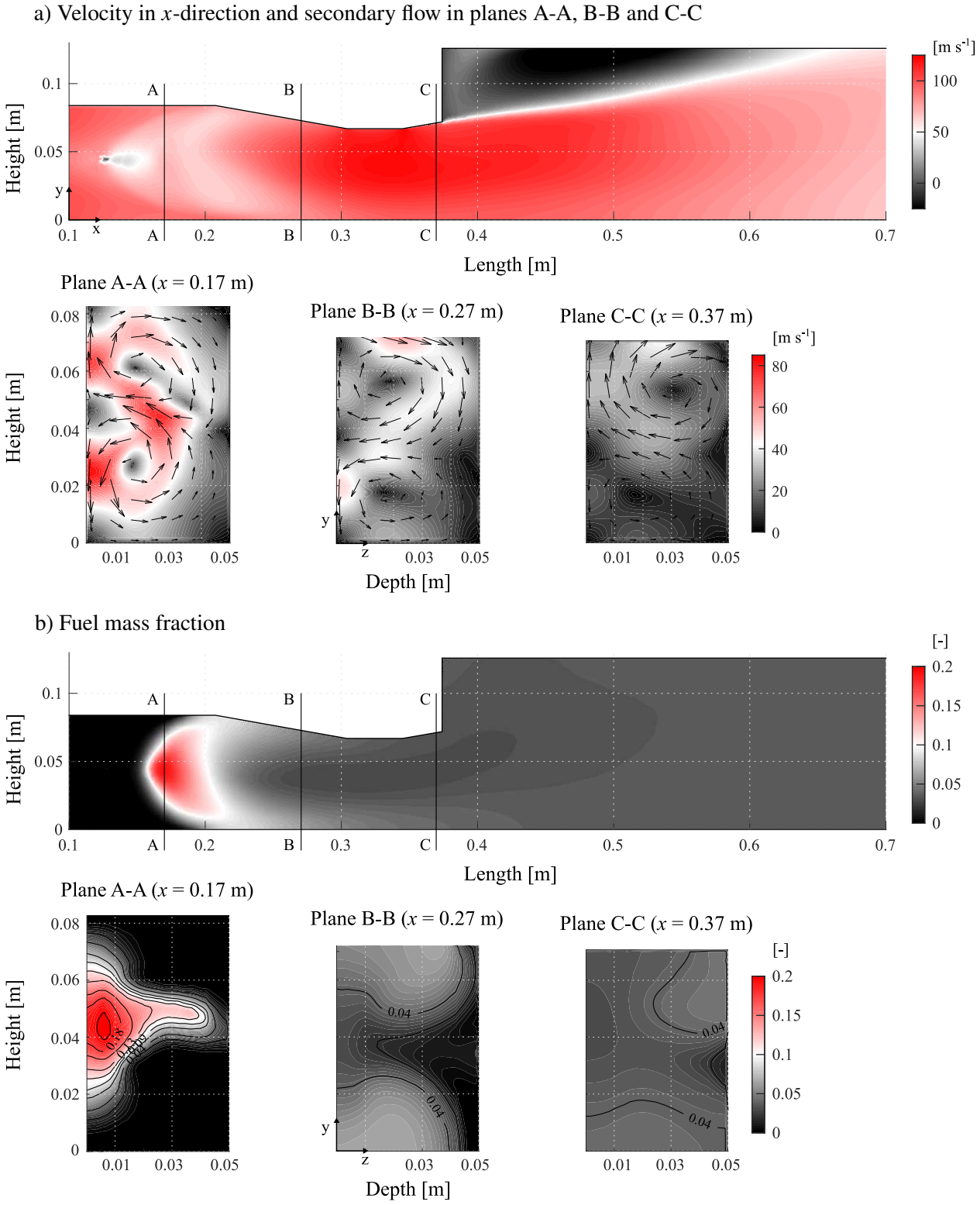

Figure 4.3: *a) Velocity in x-direction in symmetry plane b) Fuel mass fraction in symmetry plane and cut planes in increasing x-direction.*

4.3 Premixed Combustion

4.3.1 Numerical Setup

The reactive simulations are carried out using a quarter of the reheat combustor geometry without the vortex generators nor the fuel injection port. The geometry is discretized using a non-structured tetrahedral mesh, cf. Fig. 4.4. The backward facing step area is further refined in order to resolve the shear layer formed by the area jump. At the walls, a prismatic boundary-layer mesh is employed. A summary of the mesh properties is listed in Tab. 4.2.

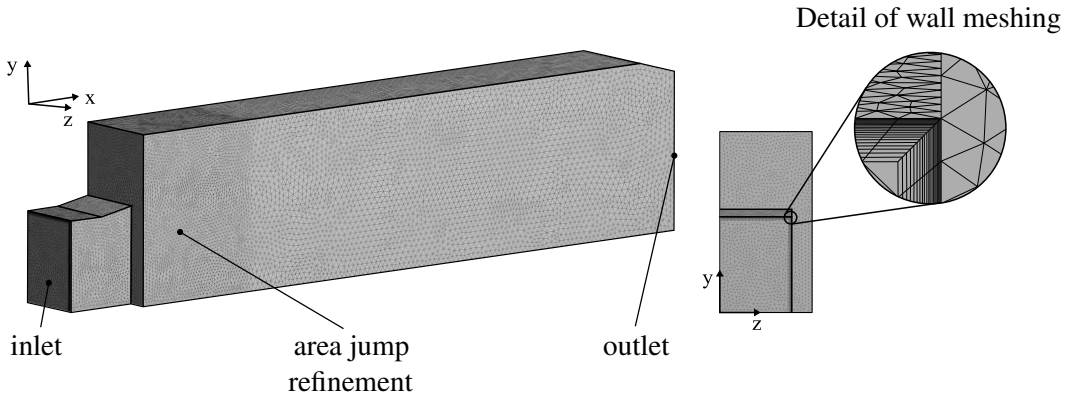

Figure 4.4: *Mesh of premixed combustion configuration.*

Table 4.2: *Summary of mesh properties for premixed configuration.*

Size	Size refinement	No. layers prismatic mesh	Height 1st element prismatic mesh	Growth rate prismatic mesh	No. elements
4 mm	2.5 mm	30	0.05 mm	1.10	1.1×10^6

Premixed RANS simulations using the realizable k-ε turbulence closure are employed for the reactive mean flow, cf. Section 2.2.1. Tailored combustion models for the propagation and auto-ignition stabilized zones are employed, cf. Sections 2.2.2 and 2.2.3, respectively. At the inlet, the velocity as well as turbulent kinetic energy and turbulent dissipation profiles obtained from isothermal simulations are prescribed. The near-wall areas are modeled with wall functions, specifically the Enhanced Wall Treatment from Fluent [53] is used. Numerically, a coupled

velocity-pressure solver is employed with second order spatial discretization. Convergence is considered achieved when the residua reach levels of 1×10^{-5}. Furthermore, mass conservation is checked: the net balance of inlet/outlet mass flows through the system's open boundaries is of order $1 \times 10^{-9}\,\mathrm{kg\,s^{-1}}$. Mesh independence is ensured by carrying out additional simulations with 0.7×10^6 and 1.7×10^6 cells, respectively. Details of the mesh independence study are presented in Appendix F.2.

4.3.2 Results

In order to determine the accuracy of the presented CFD methodology, simulated volumetric heat release distributions are compared to time averaged line-of-sight (LOS) integrated CH^* chemiluminescence (CL) images [30, 31]. Four series of measurements, in which different control parameters are varied, are used for validation. Note that CH^* CL images are representative of the spatial heat release distribution in premixed conditions and closely premixed conditions [78, 79] as it is the case in the studied reheat combustor (cf. mixing studies in Section 4.2). Therefore, they reveal useful information about the flame length and shape, which are important to determine the eigenfrequency in the thermoacoustic calculations.

A different control parameter is varied for each series of measurements. Specifically, air mass flow, inlet temperature of the reheat stage, propane content of fuel in the reheat stage and excess air ratio of the reheat stage are modified. These control parameters are selected because they have a large influence on the flame position, either directly by modifying the bulk flow velocity (air mass flow) or by varying the auto-ignition time delay (inlet temperatures of the reheat stage, propane content of fuel, excess air ratio of the reheat stage). Full characterization of the operating points used for validation is listed in Tab. E.1 of Appendix E. In the following Sections 4.3.2.1-4.3.2.4, reactive CFD simulations and CH^* measurements for each experimental series are compared with each other and discussed. For better comparison of experimental LOS integrated CH^* CL images to the three-dimensional simulations, the latter are averaged over the span of the reheat combustion chamber, i.e. z-direction in Fig. 4.4. Furthermore, note that the same color scale is kept for all simulations and CH^* CL images between

the different series to allow comparisons among them.

Generally, satisfactory agreement between simulations and experiments is obtained for the flame length. Further discussion about specific effects that affect the flame length for each series is below given in Sections 4.3.2.1 to 4.3.2.4. However, the simulated heat release distribution of all simulated cases differs significantly from CH^* CL observed in the experiments. In all simulations, heat release of the propagation stabilized brush is overestimated in the shear layer close to the burner inlet. This is a typical effect of Eddy Break-Up (EBU) combustion models. The employed BML combustion model is closely related to EBU models and can be regarded as a formal theoretical derivation of the EBU model [55]. Therefore, BML inherits the shortcomings of EBU models. Specifically, heat release is overstated in zones where the characteristic turbulent time is large. In reality, in highly strained regions like the burner inlet, reaction rates of hydrocarbon fuels are damped by local stretch rates. A very illustrative, qualitative comparison of the effect of stretch rates and heat loss on common combustion models e.g. Eddy Dissipation Model (EDM), Zimont Flame Speed Closure model, Flame Generated Manifolds (FGM), applied to a swirl-stabilized flame is given in [80]. Therein, it is shown that stretch and heat losses need to be considered for an accurate reproduction of experimental results in flames with strong shear layers. Consideration of heat losses and stretch rates in the CFD methodology used in this thesis is left for future work.

In the auto-ignition stabilized zones, the heat release distribution is parabolic and spreads evenly along the progress variable jump. This is in line with definition of the volumetric reaction rate of the employed combustion model, which is described by a parabolic function of progress variable, cf. Eq. 2.27. A comparison to experiments is nevertheless not possible. In the CH^* CL images, the auto-ignition stabilized flame front at the center of the chamber is barely visible due to the time averaging post-processing of the CH^* CL images. Due to the stochastic formation of auto-ignition kernels, the flame front is spread out in longitudinal direction [31]. Therefore, after time averaging is applied in the CH^* CL images, details of the heat release distribution at the auto-ignition front are lost.

Finally, note that the simulated heat release spatial distribution is similar for all studied series. As discussed before, the propagation stabilized shear layers burn

close to the inlet and the auto-ignition flame front spreads uniformly along the progress variable jump. These two distinct stabilized flame areas are depicted in Figs. 4.5 a) and b), where individual propagation stabilized and auto-ignition stabilized are shown. These previously discussed characteristics are common for all series and therefore are not further discussed in the sections below.

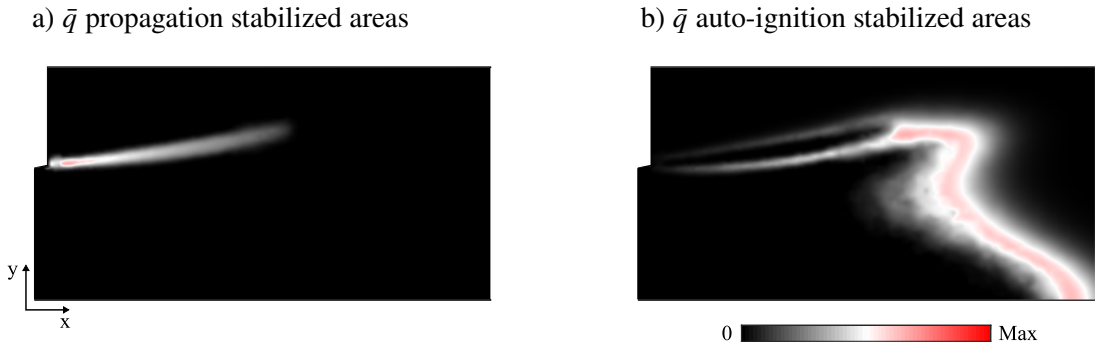

Figure 4.5: *Normalized volumetric heat release areas stabilized via propagation in a) and stabilized via auto-ignition in b). Results for OP-01.*

4.3.2.1 Series 1: Increasing Air Mass Flow

In the experimental Series 1, the inlet air mass flow of the vitiator is increased from $300\,\mathrm{g\,s^{-1}}$ in OP-01 to $420\,\mathrm{g\,s^{-1}}$ in OP-07, cf. Tab. E.1 of Appendix E. Therefore, the total mass flow through the reheat stage grows accordingly. Overall, qualitatively good agreement is found between experimental and simulated flame lengths, cf. Fig. 4.6 a). It is however observed that for increasing air mass flow, the simulated flame length increases by approximately 30%, cf. OP-01 and OP-07 in Fig. 4.6 a). The excess air ratio of the first stage is kept constant. Hence, the temperature and composition at the inlet of the reheat stage are also constant. The auto-ignition time delay only depends on temperature and composition when pressure is kept constant, cf. Eq. 2.24. The auto-ignition time delay is therefore constant in the CFD simulations for Series 1. As long as the mass flow increases, the bulk flow velocity increases. For a constant auto-ignition time delay the flame is therefore stabilized further downstream of the chamber. However, this effect is not observed in the experimental images. In Fig. 4.6 a), it can be observed that the flame length of experimental images remains constant regardless of the increasing air mass flow. This can be explained by the fact that in reality heat loss, which is

not included in the simulations, also plays a role. For higher air mass flows the heat loss in the mixing section decreases. This in turn raises temperature in the mixing section promoting the formation of auto-ignition kernels and ultimately inducing shorter flame lengths. The flame shortening effect of the reduced heat loss for higher mass flows compensates the higher bulk flow velocity resulting in the almost constant flame length observed in the experiments, cf. Fig. 4.6 a).

4.3.2.2 Series 2: Increasing Inlet Temperature of Reheat Stage

In the experimental Series 2, the inlet temperature of the reheat stage is increased, cf. Tab. E.1 of Appendix E. This is accomplished by decreasing the excess air ratio in the first stage from 2.10 in OP-05 to 1.95 in OP-13. Overall qualitatively good agreement is found between experimental and simulated flame lengths, cf. Fig. 4.6 b). As for Series 1, simulations in Series 2 yield flames about 30% longer than experiments. This difference is ascribed to the effect of heat loss on the inlet temperature, following the reasoning laid out for Series 1, cf. Section 4.3.2.1. It is also observed that for increasing inlet temperatures, the flame length decreases. The auto-ignition delay time decreases for increasing inlet temperatures, cf. Eq. 2.24. Hence, as long as the air mass flow is kept constant –i.e. bulk flow velocity is constant, the flame stabilization position is shifted towards the chamber inlet. This trend is observed similarly in the experimental CH^* CL images and the heat release distributions from the simulations. Thus, it can be concluded that the CFD methodology is able to reproduce the increase of inlet temperature of the reheat stage.

4.3.2.3 Series 3: Increasing Propane Content of Fuel in Reheat Stage

In the experimental Series 3, the mass fraction of propane in the fuel of the reheat stage is increased from 0% in OP-15 to 15% in OP-05, cf. Tab. E.1 of Appendix E. Propane features a longer hydrocarbon chain than methane, which is the main constituent of the natural gas used as fuel in the experiments. By adding propane, more reactive radicals are formed during the chain-branching reaction phase responsible for ignition [58]. Hence, the auto-ignition time is reduced and the flame stabilizes closer to the reheat combustion chamber inlet.

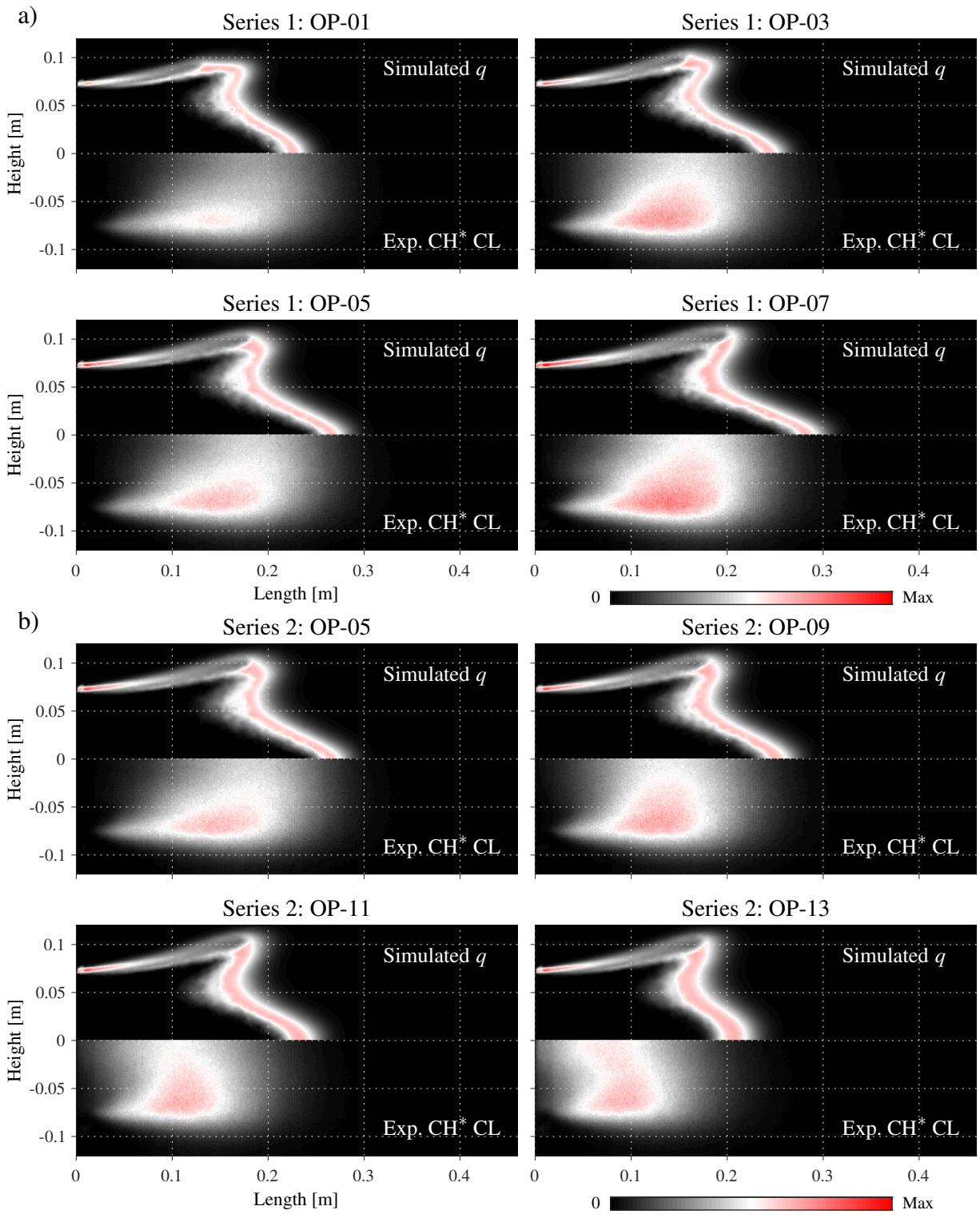

Figure 4.6: *Normalized volumetric heat release rate (q) and normalized intensity of CH* CL images for a) Series 1: Increasing air mass flow and b) Series 2: Increasing inlet temperature of reheat stage. CH* CL images were kindly provided by Jonathan McClure.*

This effect is captured by the correlation employed to determine the auto-ignition time delay, Eq. 2.24, and therefore it is reflected in the simulations. In Fig. 4.7 a), the simulated operating point OP-05 with the highest propane content (15% in mass) presents a flame approximately 40% shorter than its counterpart OP-01 without added propane. Compared to experiments, good agreement of flame length is found for the operating point OP-05 with high propane content. Accuracy is however progressively lost for low propane content. As an example of this trend, for OP-15, in which no propane is added, the simulated flame is almost 50% longer than its experimental counterpart. This indicates that the employed time-delay correlation especially overestimates the auto-ignition time delay for low propane contents. For higher propane contents however, the model accuracy increases.

For operating points with low propane content, it would be advisable to improve the auto-ignition delay model. For example, assuming isobaric combustion, values of auto-ignition time delays as function of temperature and propane content could be tabulated using Cantera. Such a look-up table could be used later as input in the CFD simulations.

4.3.2.4 Series 4: Decreasing Excess Air Ratio of Reheat Stage

In the experimental Series 4, the excess air ratio of the reheat stage is decreased from 1.55 in OP-21 to 1.10 in OP-25, cf. Tab. E.1 of Appendix E. This is achieved by keeping the air mass flow constant and increasing the fuel mass flow. Temperature and composition at the inlet of the reheat stage are also kept constant for all of the cases in Series 4. This implies that the auto-ignition time delay and therefore the flame length are constant. In general, good qualitative agreement is found between experimental and simulated flame lengths, cf. Fig. 4.7 b). As for Series 1 and 2, the simulations yield flames that are longer than those observed in the experiments, in this case about 20%. This difference can again be attributed to not taking into account heat loss effects that reduce the auto-ignition time delay, cf. Section 4.3.2.1. Finally, increased reactivity is observed for both simulations and experimental CH^* CL images for decreasing excess air ratios. Therefore, simulations are able to capture the effects of increasing fuel mass flow on the

flame lengths in the reheat combustor.

4.4 Summary and Outlook

In this chapter, a CFD procedure to obtain reactive mean flow fields of reheat flames suitable for acoustic simulations was introduced. Such a procedure comprises two steps: isothermal mixing and premixed combustion.

From the comparison of simulated heat release distributions with experimental CH^* CL images, the following conclusions can be drawn:

- The CFD procedure is able to capture satisfactorily the experimental flame length and shape. Specifically, modifications in air mass flow, reheat combustor inlet temperature and excess air ratio in the reheat combustor are reproduced. Only for low propane contents, the deviation of the flame length from experiments is larger than 30%.
- The heat release distribution in the propagation stabilized zones of the reheat flame deviates substantially from reactivity observed in experiments. Heat release is overestimated in the shear layer towards the burner inlet. This is due to not consider flame stretch rates.

The heat release distribution in propagation stabilized areas of the reheat flame could be immediately improved by adding stretch effects to the BML model. Yet another possibility is to explore other combustion models for propagation such as the FGM. For such models, extended formulations including heat loss and high stretch rates effects are readily available [34]. Within the thermoacoustic context, the main challenge to be addressed when using FGM compared to BML, would be linearizing the chemical source term ($\bar{\dot{\omega}}_c$). A linearized $\bar{\dot{\omega}}_c$ is required to capture acoustic heat release modulation in the shear layer, cf. Eq. 2.66. For the BML model, $\bar{\dot{\omega}}_c$ is a parabolic function of progress variable, cf. Eq. 2.18, and therefore its linearization is a trivial task. In FGM, however, $\bar{\dot{\omega}}_c$ is given in form of look-up tables [81], so a linearization procedure in such environment would be required.

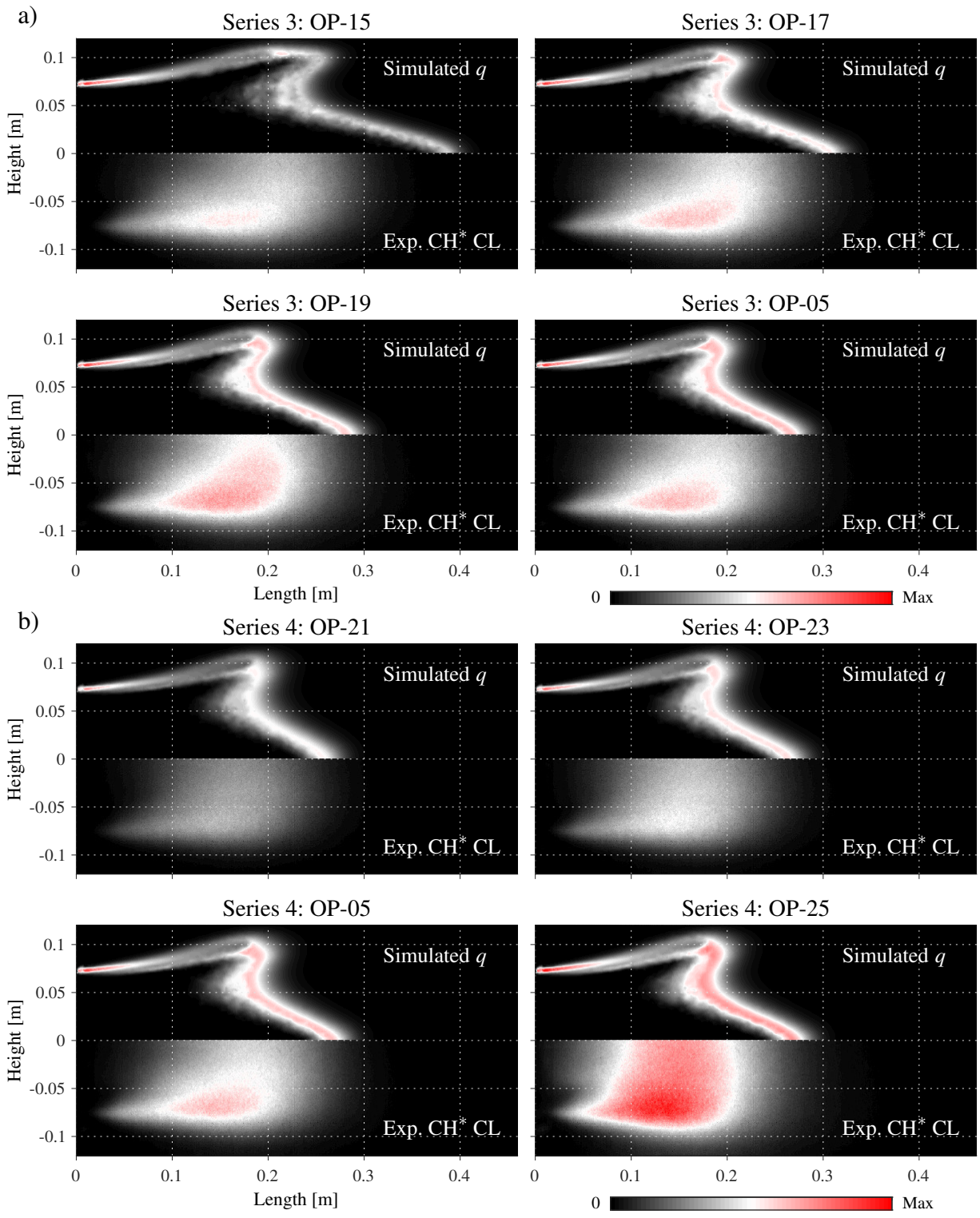

Figure 4.7: *Normalized volumetric heat release rate (q) and normalized intensity CH* CL images for a) Series 3: Increasing propane content of fuel and b) Series 4: Decreasing excess air ratio of reheat stage. CH* CL images were kindly provided by Jonathan McClure.*

Finally, to obtain a more detailed heat release distribution in the auto-ignition stabilized zones, it would be required using a more complex modeling approach. Some suitable combustion models devoted to the task could be the RANS procedure using joint PDF developed by Brandt [82] or the composite RANS method from Wang [83], which uses presumed PDF for mixing and propagation and a normalized particle residence time depending on local mixture conditions for auto-ignition. Also more intensive computing LES approaches such as those followed by Kulkarni [51] or Schulz [84] could be potentially employed. All in all, taking into account the simplicity of the models employed in the CFD setup it can be concluded that the results are accurate enough for being used as input for acoustic simulations, in which the position of the flame –i.e. the position of the temperature and density mean flow gradients– is the fundamental quantity that determines acoustic propagation. This assumption will be verified in Chapter 5 by comparing simulated and experimental eigenfrequencies of the first transverse mode of the reheat combustor.

5 Linear Stability Analysis of a High-Frequency Transverse Reheat Combustor Experiment

In this chapter, a linear stability analysis of the first transverse (T1) eigenmode of the lab-scale reheat combustor is carried out. First, the different damping mechanisms are assessed and discussed. In particular, interactions of acoustics with the non-homogeneous mean flow and the acoustic boundary layer are studied. Second, the driving for each thermoacoustic mechanism presented in Chapter 2 (deformation, displacement, convective modulation of the reactive shear layer and acoustic modulation of auto-ignition time delay) is quantified. Finally, the net contribution of damping and driving is calculated and the linear stability is determined.

5.1 Damping Assessment

Generally, in thermoacoustic systems, damping –i.e. losses of acoustic energy-– can occur due to acoustic energy flux through boundaries and acoustic dissipation within the domain. For the studied configuration, this unfolds into three contributions:

- Acoustic energy flux through inlet and outlet.
- Viscous and thermal dissipation within the acoustic boundary layer.
- Transformation of acoustic energy into vortical or entropy modes due to

interactions of acoustics with non-homogeneous, non-homentropic mean flow.

The first contribution –acoustic losses through boundaries– is usually modeled as impedances or reflection coefficients which are imposed at the corresponding inlet or outlet. There are different ways of obtaining such impedances. One can use numerical methods e.g. hybrid CAA/CFD methodology based on the LNSE as done in [85] or experimental approaches that measure the reflection coefficients in dedicated test rigs [86]. Altogether, determining inlet and outlet boundary conditions in real combustion chambers is one of the most challenging tasks in prediction of thermoacoustic instabilities. Industrial combustion chambers are surrounded by turbomachinery where acoustic waves can be reflected onto or transmitted in non-trivial manners. In any case, in the studied reheat combustor, for the studied T1 mode inlet and outlet are decoupled from the chamber acoustics. The acoustic eigenmode is cut-off at the inlet due to the area jump and at the outlet due to the combustion temperature jump. This means that fluctuating pressure is zero at the inlet and the outlet and therefore, for low Ma, the acoustic energy flux is negligible. As a result, acoustic losses through open boundaries are not relevant for the studied mode and are neglected in the subsequent analysis.

The second mechanism –losses arising from dissipation within the acoustic boundary layer– can be accounted for with appropriate boundary conditions, cf. Section 2.3.3.4. The third mechanism comprises losses of acoustic energy due to its transformation into vortical and entropy modes. This contribution is inherently captured by the LEE. Damping introduced by these last two mechanisms is discussed in following sections.

5.1.1 Damping due to Acoustic Boundary Layer

As introduced in Section 2.3.3.4, thermal dissipation within the acoustic boundary layer can be modeled as an impedance, cf. Eq. 2.57. Similarly, viscous dissipation can be expressed as function of normal velocity, cf. Eq. 2.59. In the following, studies for determination of thermal and viscous contributions to damping are conducted separately in order to compare them with each other. In each case,

zero-mean-flow isentropic LEE without unsteady heat release, which correspond to Eqs. 2.47-2.48 with $\bar{\boldsymbol{u}} = 0$ and $\hat{q} = 0$, are solved. These equations can be regarded as an equation system equivalent to the Helmholtz equation, in which only acoustic modes propagate. Mean flow velocity can be neglected based on the fact that the hydrodynamic boundary layer is much thicker than the acoustic boundary layer. Therefore, mean flow velocity can be considered zero within the acoustic boundary layer. The zero-mean-flow isentropic LEE are solved via FEM, cf. Section 2.3.4. As mean flow is neglected, there are no convective effects and numerical stabilization is not required. The computational domain only comprises a quarter of the reheat combustor and is discretized using an unstructured tetrahedral mesh with a resolution of approximately 15 cells per wavelength. The employed mesh and boundary conditions are shown in Fig. 5.1. As background mean flow, constant pressure equal to ambient pressure and mean temperature fields obtained from reactive CFD (cf. Section 4.3.2) are prescribed. Finally, dependence of viscosity and thermal conductivity on temperature is obtained from suitable correlations following [87].

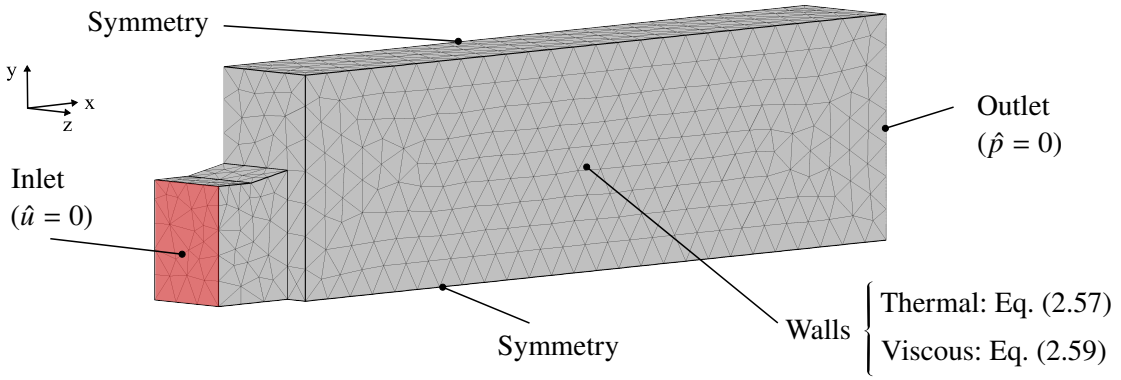

Figure 5.1: *Mesh and boundary conditions used for assessment of acoustic boundary layer losses.*

The zero-mean-flow isentropic LEE are solved for all available operating points, cf. Tab. E.1 of Appendix E. Obtained damping rates are plotted in Fig. 5.2. Similar values of damping rates are obtained for all operating points. This is due to similar acoustic mode shapes and small changes in dynamic viscosity and thermal conductivity for all the studies cases.

As linear acoustic motions are considered, the total damping due to the boundary layer is obtained by simply adding thermal and viscous contributions. Comparing

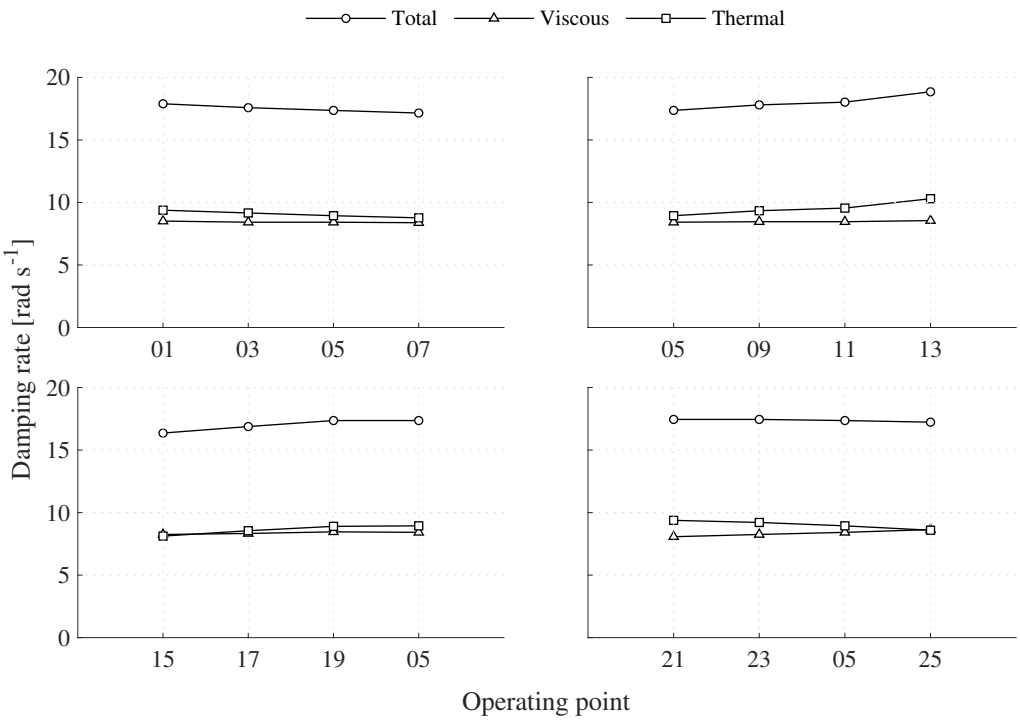

Figure 5.2: *Damping rates due to acoustic boundary layer with viscous and thermal contributions.*

thermal and viscous contributions (cf. Fig. 5.2), it is observed that both are of the same order of magnitude. This corresponds to the theoretical viscous-to-thermal acoustic energy flux ratio for one-dimensional configurations, whose order of magnitude is $\sqrt{Pr}/(\gamma - 1)$, where Pr is the Prandtl number [69]. For perfect gases, such ratio is of order unity implying that thermal and viscous losses are equally important. Results in Fig. 5.2 evidence that the theoretical ratio derived for one-dimensional configurations still holds for more complex three-dimensional geometries.

5.1.2 Damping due to Interactions with Non-Homentropic Mean Flow

In this section, the damping introduced by the non-homentropic mean flow is assessed. To do so, the isentropic LEE, Eqs. 2.47-2.48 without unsteady heat release sources are solved. First, the numerical setup is presented. Second, the

results are presented. There, the specific sources of damping are discussed.

5.1.2.1 Numerical Setup

The computational domain comprises a 2D cutting plane of a quarter of the chamber of the reheat combustor, cf. Fig. 5.3. The flat prismatic design of the reheat combustion chamber allows to characterize in first instance its flow as quasi two-dimensional. Thus, for the thermoacoustic related simulations using a simple two-dimensional geometry is justified. A schematic of the employed geometry, mesh and boundary conditions is shown in Fig. 5.3. The required background mean flow is obtained from reactive RANS simulations introduced in Chapter 4.

The geometry is discretized using an unstructured triangular mesh with a characteristic base size element of 1.5×10^{-3} m. The area near to the corner where the mean flow detaches forming a shear layer is further refined up to 3×10^{-6} m in order to appropriately capture the interactions between acoustics and mean flow [48]. Corresponding mesh independence analyses are shown in Appendix G. Eigensolutions of the isentropic LEE equations, Eqs. 2.47-2.48, are obtained using stabilized FEM, cf. Section 2.3.4. Due to dominance of convective terms in the governing equations, SUPG numerical stabilization is employed. This stabilization method uses a free parameter (α_τ) that has to be tuned for each specific setup. As SUPG stabilization introduces artificial diffusion for stabilizing, α_τ has a direct influence on damping rates. Consequently, it is needed to ensure independence of damping rates from this parameter. In order to do so, α_τ independence studies are carried out in Appendix G. Following those studies, the value of α_τ is set to 360. Here, it is of note to remark that only independence of damping rates from α_τ has been proved. The non-physical contribution due to artificial diffusion is present. Quantification of damping rates due to artificial diffusion of the SUPG stabilization method can be carried out following the procedure newly presented in [48]. This method calculates the damping rates using the APE. An example of application of this procedure to a similar configuration to the reheat combustor is shown in Ref. [66]. There, it is shown that artificial diffusion corresponds to about 10 % of the total damping of the LEE solution. For the reheat combustor, a similar contribution is expected and therefore a precise quantification of this

effect is left for future work.

Finally, regarding the employed boundary conditions, for the inlet an energetically neutral (cf. Eq. 2.55) and zero-vorticity (cf. Eq. 2.56) are used. The slip-wall condition is applied to walls. For the outlet, zero pressure is used. Symmetry conditions are imposed at the symmetry axis.

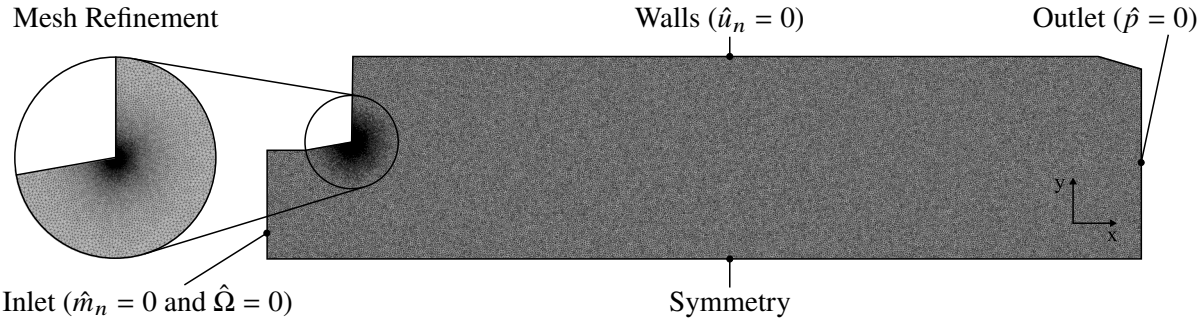

Figure 5.3: *Geometry, mesh and boundary conditions used for thermoacoustic simulations.*

5.1.2.2 Results

The results of the simulations with the isentropic LEE are structured as follows: First, general features of the T1 eigenmode are shown exemplary for the operating point OP-01. Second, a comparison of the simulated eigenfrequencies to their experimental counterparts is carried out for all operating points. Finally, the interactions of acoustics with non-homentropic mean flow are studied for all operating points. Specifically, the individual contribution to damping of the terms of the continuity source term, Eq. 2.46 is calculated. This last point allows to identify the specific sources of damping.

General Characteristics of the T1 Eigenmode

Figure 5.4 a) shows the absolute fluctuating pressure. It can be observed that the mean flow temperature jump cuts off the T1 mode before it reaches the outlet. Similarly, the area jump at the chamber inlet cuts off the mode at the inlet. Therefore, as mentioned in Section 5.1, inlet and outlet are decoupled from the acoustic eigenmode and do not contribute to energy losses. Velocity in x- and y-direction, cf. Figs. 5.4 b) and c), show the characteristic acoustically induced

vortex shedding due to interactions of fluctuating quantities and the shear layer. From those interactions acoustic damping arises, see e.g. Ref. [66].

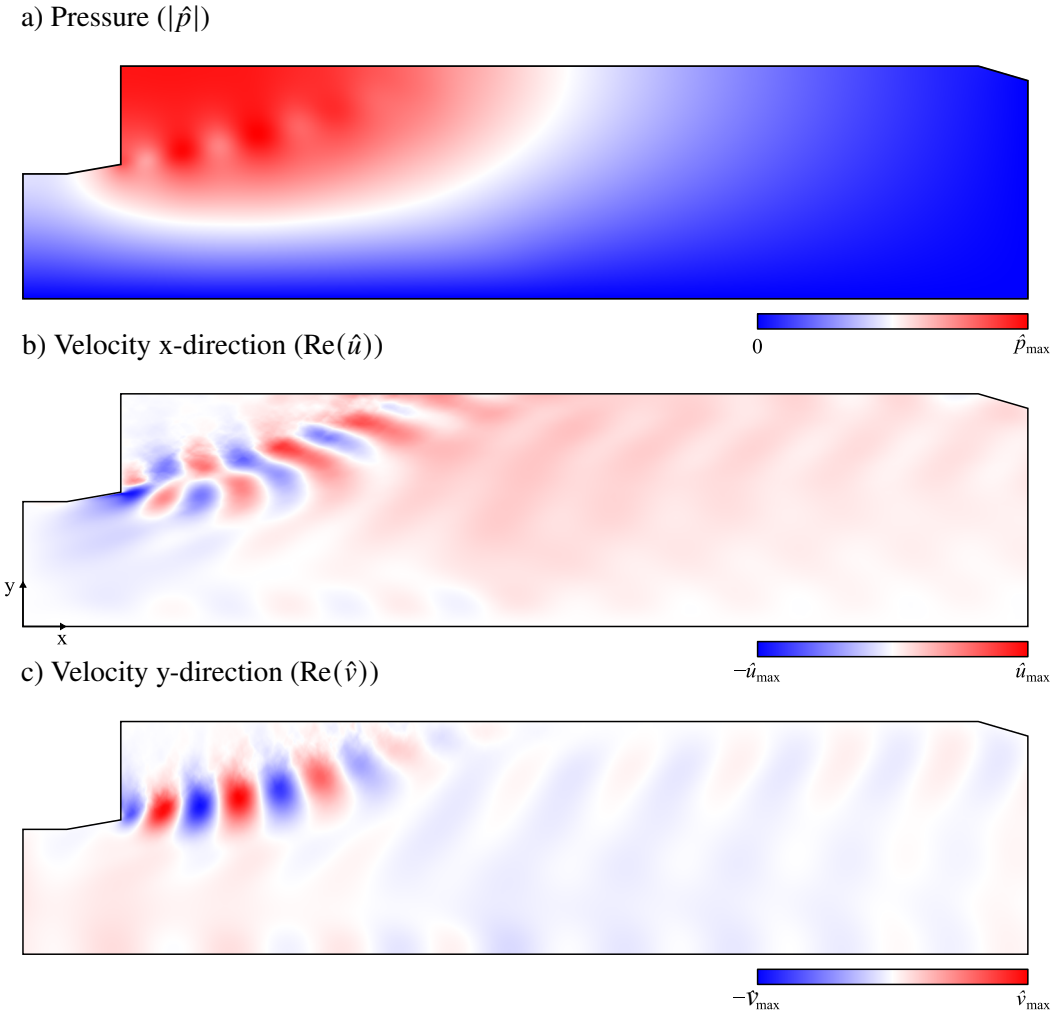

Figure 5.4: *Disturbance fields of pressure, x-direction velocity and y-direction velocity.*

Comparison of Experimental and Simulated Eigenfrequencies

In a next step, the simulated eigenfrequencies are compared to their experimental counterparts in Fig. 5.5 for all available operating points. Overall good agreement with experiments is found with errors below 5%. The largest errors observed e.g. OP-07, OP-15 or OP-25, correspond to operating points for which the flame length is overestimated in the CFD simulations, cf. Section 4.3.2.

Furthermore, the growing trend of the experimental eigenfrequencies is reproduced for all series, except Series 1. The growing/declining trend of the simulated

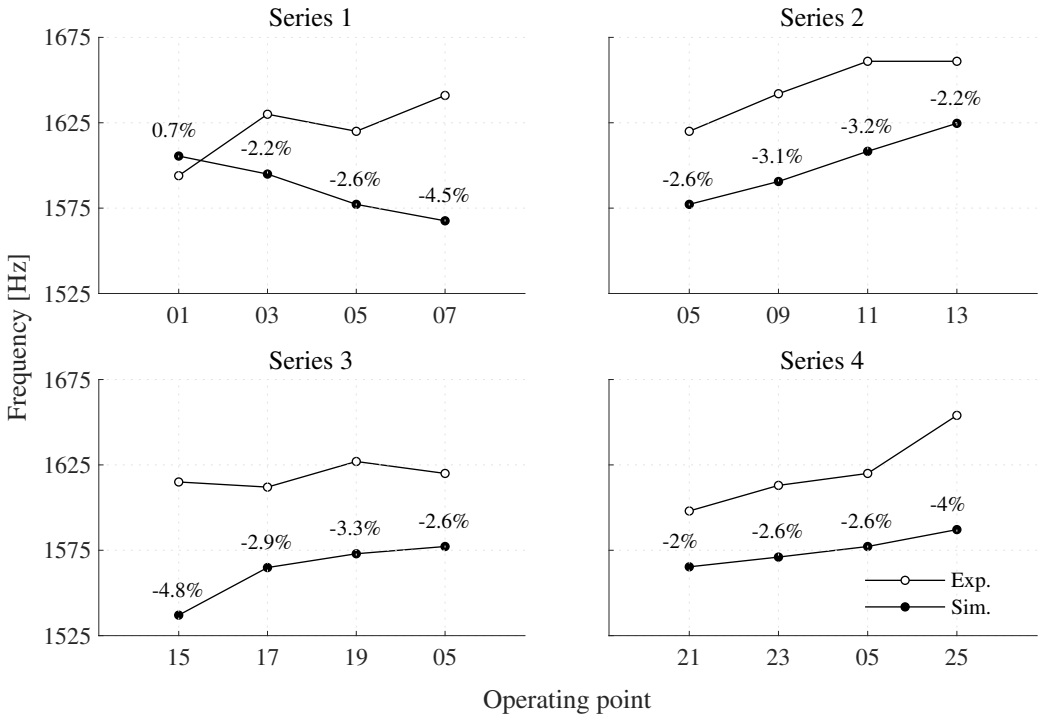

Figure 5.5: *Comparison of simulated and experimental eigenfrequencies for different operating points. Relative error of simulations with respect to experiments is also annotated.*

and experimental eigenfrequencies can be explained on basis of the flame length and temperature of the unburned and burned gas as follows. As long as the vertical dimension of the chamber is fixed, the eigenfrequencies of the T1 mode follow $f \propto \bar{c}_{\mathrm{avg}}/L_{\mathrm{fl}}$[i], in which $\bar{c}_{\mathrm{avg}}$ is the averaged speed of sound of unburned and burned gases and L_{fl} is the flame length in longitudinal direction. The flame length determines the position of the mean flow temperature jump after which the T1 eigenmode is cut off. Hence, for shorter flames, the temperature jump occurs further upstream and the effective length of the acoustic propagation domain is shorter, increasing the resonant frequency. On the other hand, when averaged temperature of the gases increases, $\bar{c}_{\mathrm{avg}}$ increases. As a consequence, the acoustic waves can propagate quicker and the resonant frequency grows.

For Series 1, the simulated flame lengths grow due to the increasing mass flow, whilst mean flow temperatures remain constant due to the constant excess air ratio. Therefore, eigenfrequency diminishes, cf. Series 1 in Fig. 5.5. The opposite

[i]Note that due to low Mach number of the configuration, frequency shift due to mean flow velocity is at first negligible.

trend is observed for experiments. In that case, frequency increases for increasing mass flows. Taking into account that in the experimental Series 1 flame length is approximately constant, increasing frequencies hints that averaged mean temperature of unburned and burn gases increases in the experiments. The CFD simulations do not reproduce such an increment because the temperature of unburned and burn gases is calculated under the adiabatic assumption and therefore obtained from adiabatic flame temperature calculations. The adiabatic flame temperature is a function of the excess air ratio. This is kept constant in Series 1 and therefore mean flow temperature in simulations is constant.

For Series 2, simulations replicate the growth of experimental eigenfrequencies, cf. Fig. 5.5. It is of note that the growth of eigenfrequencies for Series 2 is the strongest of all investigated series. This is due to the double effect of increasing the inlet temperature of the reheat combustor on increasing $\bar{c}_{\mathrm{avg}}$ and decreasing the auto-ignition time delay simultaneously. The latter, considering the main air mass flow is constant, yields shorter L_{fl}, which reinforces the effect of higher $\bar{c}_{\mathrm{avg}}$.

In Series 3, simulations show increasing eigenfrequencies for increasing propane content, cf. Fig. 5.5. With increasing propane content the auto-ignition time drops and therefore flames are shorter. Furthermore, $\bar{c}_{\mathrm{avg}}$ is constant due to constant mean temperatures. As a result, simulated eigenfrequencies grow. In experiments, the growing trend is less pronounced because the flame length is almost constant, cf. Fig. 4.7 a). Finally, for Series 4, the growing trend of the simulated eigenfrequencies is in line with that of the experimental. The growing trend can be attributed to the increment of temperature of burned gases.

Overall, the small error found between simulated and experimental eigenfrequencies supports the idea that the CFD methodology presented in Chapter 4 is sufficient to reproduce acoustic propagation.

Effect of Continuity Source Term on Eigenfrequencies and Damping Rates

By analyzing the contributions of the individual terms of the continuity source term ($\hat{S}_{\mathrm{m}}$) (cf. Eq. 2.46) it is possible to decompose damping due to acoustically induced vortex shedding and due to interactions with the non-homentropic (non-isothermal) mean flow. In order to do so, the following studies are carried out and

compared:

- Isentropic LEE, Eqs. 2.47-2.48.
- Zero-mean-flow LEE, which correspond to Eqs. 2.36-2.38 with $\bar{\boldsymbol{u}} = 0$. These equations can be regarded as a system equivalent to the Helmholtz equation. Therefore, it is used as baseline for comparisons of acoustic propagation.
- Isentropic LEE without the term $\hat{u} \cdot \nabla\bar{\rho}$, cf. Eq. 2.46, responsible for the interactions between perturbation velocity and non-isothermal mean flow.
- Isentropic LEE without the term $\frac{\hat{p}}{\bar{p}}(\bar{\boldsymbol{u}} \cdot \nabla\bar{\rho})$, cf. Eq. 2.46, responsible for the interaction between perturbation pressure and non-isothermal mean flow. This term can be interpreted as interaction between pressure and mean heat release, cf. Eq. 2.51.

Note that unsteady heat release has been neglected as the focus is put only on damping effects. Absolute perturbation pressure fields for each study of the representative operating point OP-01 are depicted in Fig. 5.6. The corresponding eigenfrequencies and damping rates for OP-01 are gathered in Tab. 5.1.

In Fig. 5.6 a), b) and c) it can be observed that the pressure modes obtained from the zero-mean-flow LEE, isentropic LEE and isentropic LEE without $\frac{\hat{p}}{\bar{p}}(\bar{\boldsymbol{u}} \cdot \nabla\bar{\rho})$ (cf. Eqs. 2.46-2.48) agree in length and shape. This is further corroborated in Tab. 5.1 where the eigenfrequencies for those cases are within 1% error margin. Therefore, the isentropic LEE correctly reproduce the acoustic propagation of the baseline solution using zero-mean-flow LEE, cf. Figs. 5.6 a) and c).

Furthermore, neglecting $\frac{\hat{p}}{\bar{p}}(\bar{\boldsymbol{u}} \cdot \nabla\bar{\rho})$ does not have effect on acoustic propagation. Exclusion of the term $\hat{u} \cdot \nabla\bar{\rho}$ (cf. Eq. 2.46) however has an elongating effect in the mode shape in comparison to the zero-mean-flow LEE solution, cf. Fig. 5.6 c).

Finally, by examining the damping rates it can be concluded that the term $\frac{\hat{p}}{\bar{p}}(\bar{\boldsymbol{u}} \cdot \nabla\bar{\rho})$ (cf. Eq. 2.46) first, induces damping –about $37\,\mathrm{rad\,s^{-1}}$ for OP-01– as expected from its theoretical physical interpretation shown in Section 2.3.2.2. Second, the damping introduced by this term, which stems from the interaction of acoustics

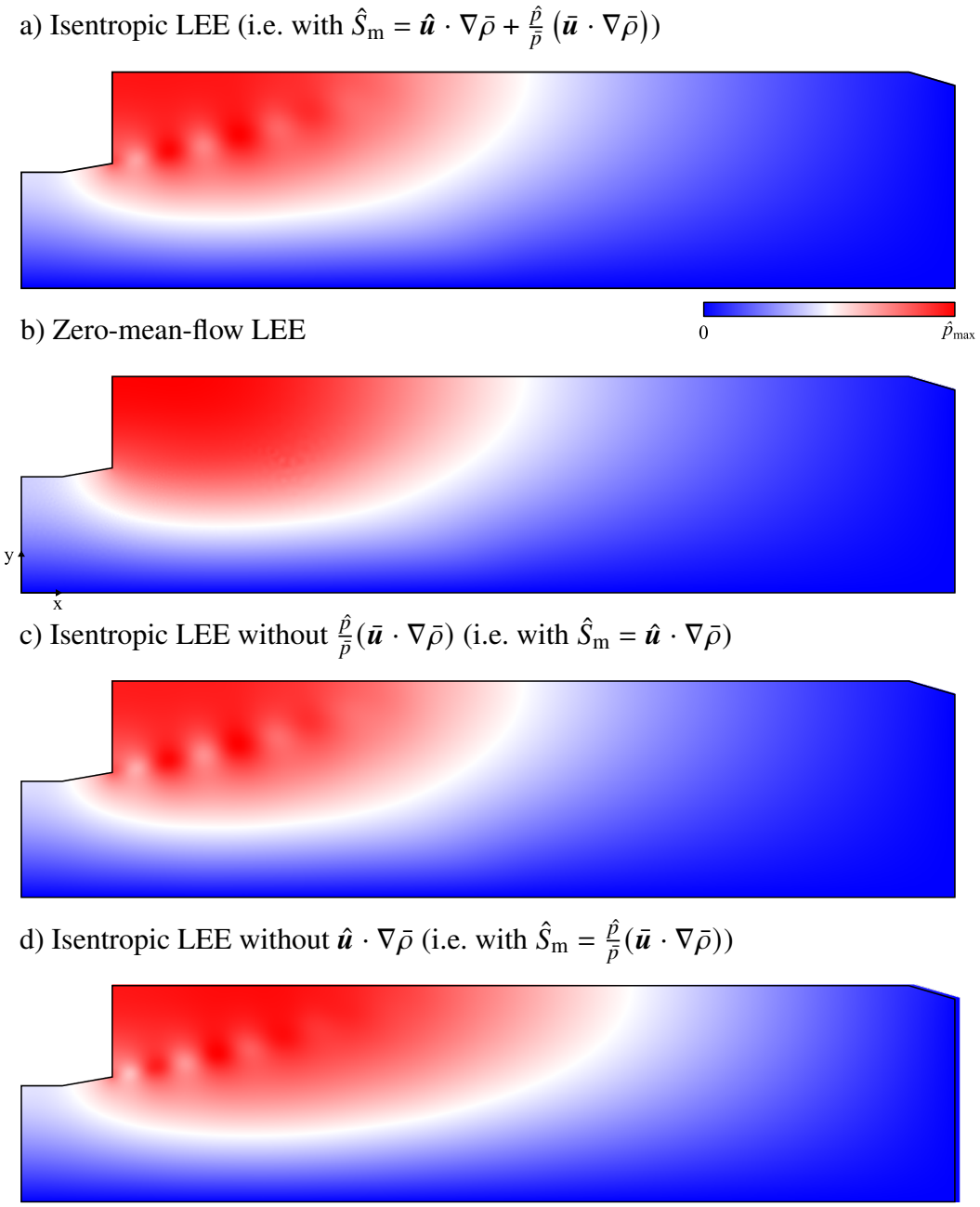

Figure 5.6: *Absolute acoustic pressure of T1 eigenmode for OP-01 obtained from solving the isentropic LEE with different continuity source terms.*

with non-homentropic mean flow is not negligible as it represents about 25% of the total damping. The remainder is attributed to damping due to vortex shedding. Note that, damping rates of isentropic LEE without $\hat{u} \cdot \nabla\bar{\rho}$ (cf. Eq. 2.46) are not discussed. The frequency and especially the mode shape for that

Table 5.1: *Eigenfrequency and damping rates neglecting different terms in the continuity source term ($\hat{S}_\mathrm{m}$).*

Equations	Eigenfrequency [Hz]	Damping rate [rad s^{-1}]
Isentropic LEE	1606	143
Zero-mean-flow LEE	1612	0
Isentropic LEE without $\hat{S}_\mathrm{m} = \frac{\hat{p}}{\bar{p}}(\bar{\boldsymbol{u}} \cdot \nabla\bar{\rho})$	1603	106
Isentropic LEE without $\hat{S}_\mathrm{m} = \hat{\boldsymbol{u}} \cdot \nabla\bar{\rho}$	1759	220

case are considered too deviated from the reference zero-mean-flow LEE solution (and the rest of isentropic LEE solutions) to be compared with the latter.

In summary, the good agreement in mode shape and eigenfrequencies between zero-mean-flow LEE and isentropic LEE hints that acoustic propagation is well reproduced by the isentropic LEE. It is also shown that the term $\hat{u} \cdot \nabla\bar{\rho}$ (cf. Eq. 2.46) plays an important role on the acoustic propagation as its exclusion notably modifies the mode shape and the eigenfrequency. In addition, it is shown that the term $\frac{\hat{p}}{\bar{p}}(\bar{\boldsymbol{u}} \cdot \nabla\bar{\rho})$ (cf. Eq. 2.46) is an important source of damping despite the fact that the generation of entropy associated to it is only a second-order magnitude quantity with respect to the perturbation pressure, cf. Eq. 2.52. Therefore, when the isentropic LEE (cf. Eqs. 2.47-2.48) are applied, it is necessary to consider all terms in the continuity source term in order to obtain accurate results.

Further studies calculating damping rates neglecting $\frac{\hat{p}}{\bar{p}}(\bar{\boldsymbol{u}} \cdot \nabla\bar{\rho})$ and eigenfrequencies neglecting $\hat{u} \cdot \nabla\bar{\rho}$ are carried out for all available operating points, cf. Tab. E.1. The corresponding results are plotted in Figs. 5.7 and 5.8, respectively.

For Series 1 (cf. Fig. 5.7), damping rates (shown as negative growth rates) obtained from the isentropic LEE with and without the term $\frac{\hat{p}}{\bar{p}}(\bar{\boldsymbol{u}} \cdot \nabla\bar{\rho})$ grow for increasing mass flow. Higher mass flows imply higher velocities at the shear layers that form after the inlet area jump and therefore mean vorticity increases. This in turn, strengthens the acoustically induced vortex shedding leading to increased damping rates [33]. When the term $\frac{\hat{p}}{\bar{p}}(\bar{\boldsymbol{u}} \cdot \nabla\bar{\rho})$ is neglected, damping rates become lower because the damping due to acoustic interactions with non-homentropic flow is not considered. The damping rate shift is roughly constant as a result

of almost constant mean flow density gradients. The damping rates calculated without $\frac{\hat{p}}{\bar{p}}(\bar{\boldsymbol{u}} \cdot \nabla\bar{\rho})$ correspond to damping due to acoustic vortex shedding only (cf. curve with black markers in Fig. 5.7) .

For Series 2, the isentropic LEE yield a nearly flat sequence of damping rates for increasing reheat combustor inlet temperatures (T_u), cf. Fig. 5.7. Mass flow is constant for Series 2, cf. Tab. E.1. Consequently, damping due to vortex shedding is also constant in first instance. Additionally, as temperature of the burned gases (T_b) is roughly constant, the temperature jump and therefore the intensity of the mean flow density gradients is lower for increasing T_u. As a result, lower damping rates should be obtained. This is not observed in the simulations, as the obtained damping rates are mostly constant. This fact could be explained by taking into consideration an additional factor: the flame length. Shorter flames result in T1 mode shapes more compact in axial direction, which in turn yield higher damping rates, cf. Ref. [88]. As flames are shorter for increasing T_u, this effect would counterweight the expected diminishing damping rates due to the term $\frac{\hat{p}}{\bar{p}}(\bar{\boldsymbol{u}} \cdot \nabla\bar{\rho})$, resulting finally in a flat curve. Following the same argument, damping rates when $\frac{\hat{p}}{\bar{p}}(\bar{\boldsymbol{u}} \cdot \nabla\bar{\rho})$ is neglected (cf. black markers in Fig. 5.7), which are solely due to vortex shedding, should be constant. However, that is not observed. The declining trend would be again explained by the effect of shorter T1 mode lengths for which higher damping rates are obtained.

For Series 3, mass flow is constant and T_u and T_b are almost constant. Therefore, as for Series 2, the decreasing flame length with increasing propane content (cf. Fig. 4.7 a)) would explain the descending trend of damping rates, cf. Fig. 5.7.

For Series 4, mass flow, T_u and flame length are constant, cf. Tab. E.1 and Fig. 4.7 b), respectively. As mass flow is constant, damping due to acoustically induced vortex shedding is nearly constant. This is observed in the damping rates obtained without the term $\frac{\hat{p}}{\bar{p}}(\bar{\boldsymbol{u}} \cdot \nabla\bar{\rho})$ (cf. white markers of Series 4 in Fig. 5.7). When the latter term is considered, damping rates increase for higher T_b due to the larger mean flow density gradients.

Finally, in Fig. 5.8 the effect of neglecting $\hat{u} \cdot \nabla\bar{\rho}$ in the continuity source term (cf. Eq. 2.46) of the isentropic LEE on eigenfrequencies is shown for all available operating points. Similarly to the observations made for the operating point OP-

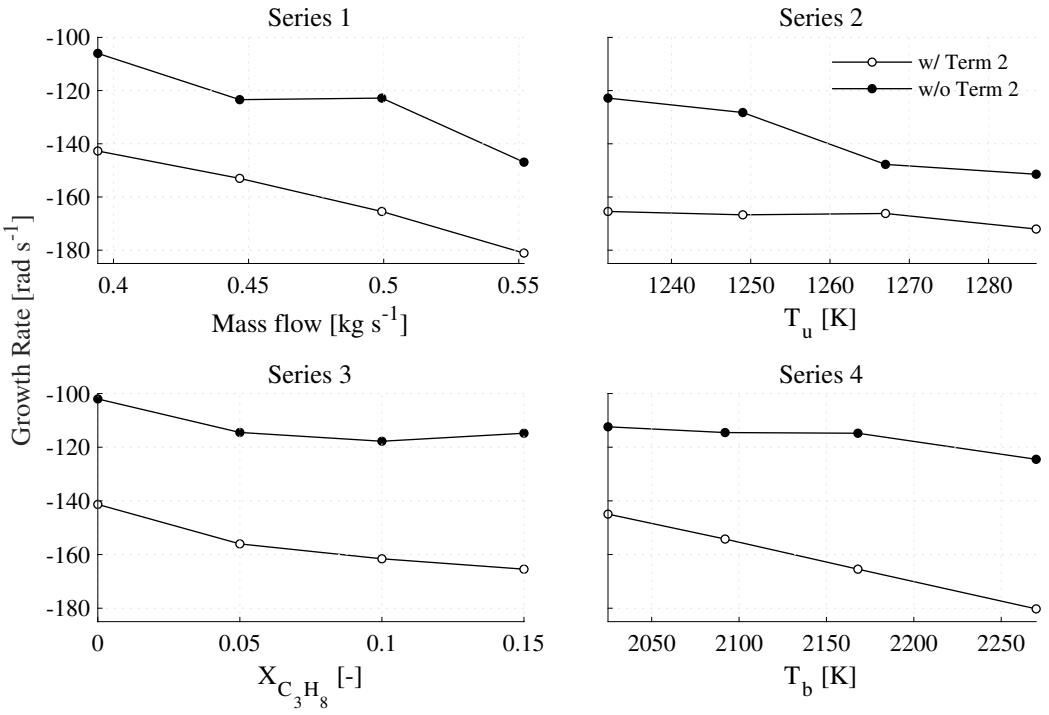

Figure 5.7: *Comparison of simulated damping rates (negative growth rates) obtained from the isentropic LEE with and without Term 2 ($\frac{\hat{\rho}}{\bar{\rho}}(\bar{\boldsymbol{u}} \cdot \nabla\bar{\rho})$) in continuity source term, cf. Eq. 2.46.*

01, a shift to higher frequencies of about 10% is obtained for all operating points. Such a frequency shift is quite regular for all operating points without changing the growing/declining trend of eigenfrequencies with the modification of the corresponding control parameter.

Summary

In this section, the following findings regarding eigenfrequencies and damping rates due to non-homentropic have been made:

- Good agreement between simulated and experimental eigenfrequencies is found. Therefore, the combination of the isentropic LEE with the CFD methodology presented in Chapter 4 is proven sufficient to correctly reproduce acoustic propagation.
- The term $\frac{\hat{\rho}}{\bar{\rho}}(\bar{\boldsymbol{u}} \cdot \nabla\bar{\rho})$ in the continuity source term (cf. Eq. 2.46) is an important source of damping despite the fact that the generation of entropy

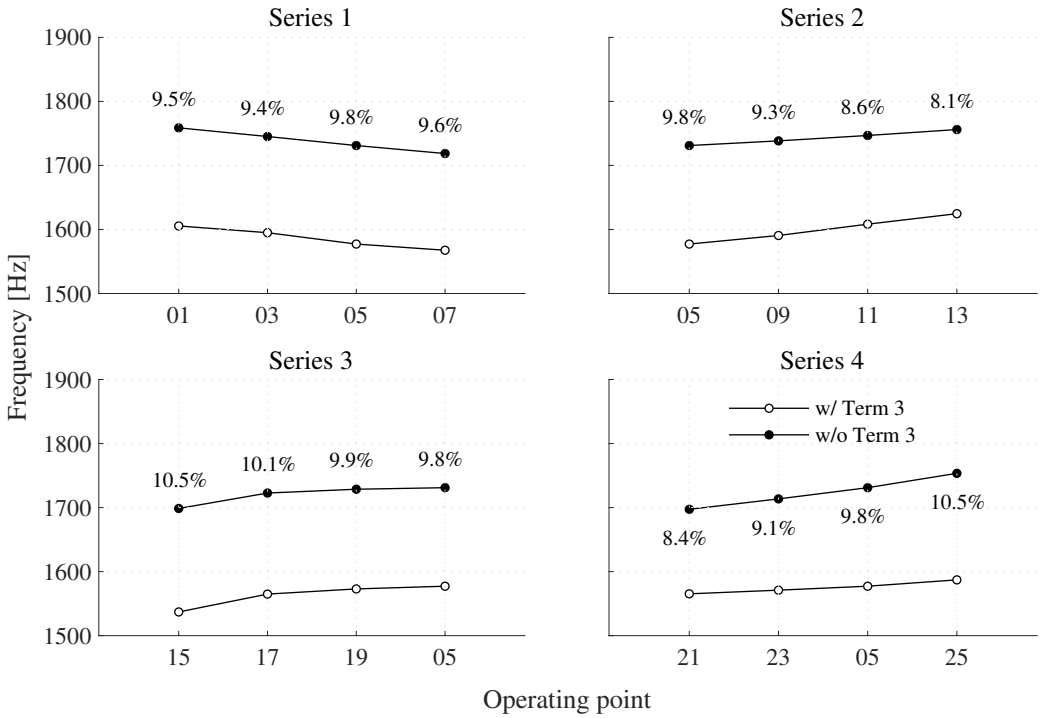

Figure 5.8: *Comparison of simulated eigenfrequencies obtained from the isentropic LEE with and without Term 3 ($\hat{u} \cdot \nabla \bar{\rho}$) in continuity source term, cf. Eq. 2.46. Relative error with respect to cases with Term 3 is also annotated.*

associated to it is only a second-order magnitude quantity with respect to the perturbation pressure, cf. Eq. 2.52. For the studied operating points of the reheat combustor it is found that it contributes to damping with values ranging from 10 to 35%. The remaining damping is due to acoustically induced vortex shedding.

· The term $\hat{u} \cdot \nabla \bar{\rho}$ in the continuity source term (cf. Eq. 2.46) plays an important role on the acoustic propagation. Its exclusion elongates the mode shape and yields inaccurate eigenfrequencies. For the studied operating points of the reheat combustor a deviation for the frequencies of about 10% is found when this term is neglected.

5.2 Driving Assessment

In this section, growth rates for all available operating points (cf. Tab. E.1) are calculated taking into account all individual thermoacoustic coupling mechanisms introduced in Section 2.4 –i.e. deformation (cf. Eq. 2.63), displacement (cf. Eq. 2.61), convective modulation of the reactive shear layer (cf. Eq. 2.66) and acoustic modulation of auto-ignition time delay (cf. Eq. 2.79). Furthermore, unsteady heat release fields and Rayleigh index fields are shown and discussed for the operating point OP-01.

The same numerical setup as the one employed for calculating damping rates due to interactions with non-homentropic mean flow is used again for assessing the driving potential. Therefore, details on the numerical setup are found in Section 5.1.2.1.

Before starting with the analysis of the driving mechanisms it is necessary to introduce the definition of the Rayleigh index (RI). RI corresponds to the integrand of the Rayleigh integral, which is the mathematical formulation of the well-known Rayleigh criterion [89]. The Rayleigh index, expressed in frequency domain, is given by:

$$\langle RI(\boldsymbol{x})\rangle = \frac{1}{4}\mathrm{Re}[\hat{p}(\boldsymbol{x})\hat{q}^*(\boldsymbol{x}) + \hat{q}(\boldsymbol{x})\hat{p}^*(\boldsymbol{x})] \tag{5.1}$$

where $\langle\cdot\rangle$ indicates the time-average operator and $(\cdot)^*$ is the complex conjugate. Equation 5.1 describes the spatial distribution of $\langle RI\rangle$ in which zones with positive values indicate driving and zones with negative values damping. Spatial integration of $\langle RI\rangle$ over the corresponding acoustic domain can also be used to determine the stability of thermoacoustic systems. As that information is redundant with the assessed growth rates will be not shown in the subsequent analysis.

5.2.1 Driving due to Displacement and Deformation Mechanisms

Flame displacement and flame deformation were identified as sources of thermoacoustic driving in swirl-stabilized flames in the high frequency regime [29, 16, 15]. It is predicted that both mechanisms also contribute to driving in propagation stabilized zones of reheat flames [28]. In the following, the contributions of both mechanisms in the lab-scale reheat combustor are analyzed and discussed. Specifically, the spatial distribution of unsteady heat release for OP-01 due to deformation $\hat{q}_\rho$ (cf. Eq. 2.63) and displacement $\hat{q}_\Delta$ (cf. Eq. 2.61) is given in Figs. 5.9 a) and c), respectively. Additionally, Rayleigh indices for OP-01 due to deformation $\langle RI_\rho \rangle$ and displacement $\langle RI_\Delta \rangle$ mechanisms are shown in Figs. 5.9 b) and d), respectively. Finally, in Fig. 5.10, growth rates calculated with each mechanism for all available operating points (cf. Tab. E.1) are shown.

Figure 5.9 a) shows a strong modulation of the heat release $\hat{q}_\rho$ at the shear layer. The intense acoustically induced vortex shedding (cf. for example $\hat{u}$ and $\hat{v}$ fields in Figs. 5.4 b) and c)) that arises from the area jump modulates $\hat{p}$ (cf. Fig. 5.4 a)) and therefore the pressure modulation is reflected in $\hat{q}_\rho$.

The driving potential of the deformation mechanism is demonstrated by inspecting $\langle RI_\rho \rangle$ (cf. Eq. 5.1) in Fig. 5.9 b). As long as isentropic acoustics is assumed, the deformation mechanism is proportional to $\hat{p}$ (cf. Eq. 2.63) and therefore it always yields positive Rayleigh index distributions (cf. Fig. 5.9 b)). It is worth mentioning that the deformation mechanism could potentially introduce damping if non-isentropic perturbations are considered. In that case, the Rayleigh index is slightly modified stating that perturbation temperature and unsteady heat release must be in phase for driving the instability [90, 67]. At the same time, in non-isentropic cases, the deformation mechanism is a function of perturbation density (cf. Eq. 2.62). Therefore, the coherence of perturbation density and pressure determines whether the instability is energized by deformation coupling. As density and temperature are not necessarily in phase, the deformation mechanism could indeed induce damping.

In Fig. 5.9 c), $\hat{q}_\Delta$ is shown. Similarly to $\hat{q}_\rho$, a modulation of heat release due to

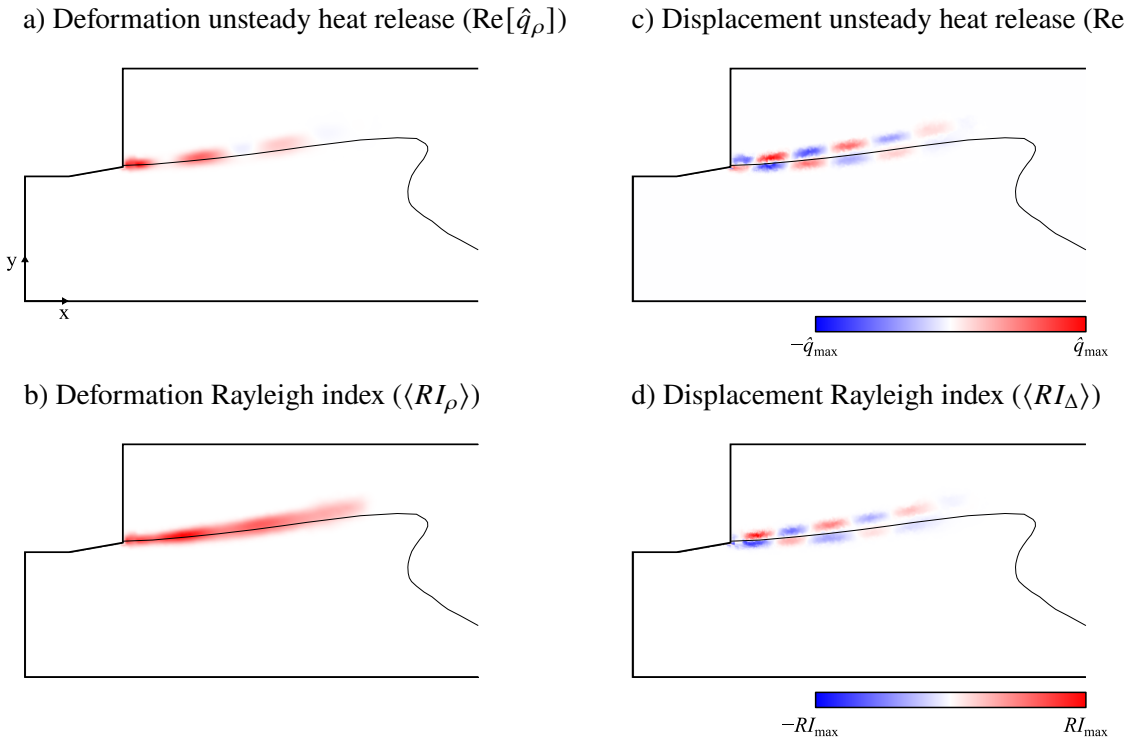

Figure 5.9: *Real part of unsteady heat release and period-averaged Rayleigh index for deformation a) and b) and displacement c) and d), respectively. Isoline $\bar{c} = 0.5$ (—), representative of the flame front position. Results for OP-01.*

vortex shedding is observed. Furthermore, an anti-symmetric pattern with respect to the flame midline (cf. black line in Fig. 5.9 c)) is observed. This is explained by the fact that the shear layer is preeminently horizontal. Therefore, $\hat{q}_\Delta$ (cf. Eq. 2.61) can be approximated to:

$$\hat{q}_\Delta \approx -\frac{\hat{v}}{\mathrm{i}\omega}\frac{\partial \bar{q}}{\partial y} \tag{5.2}$$

The mean heat release gradient in y-direction presents an anti-symmetric distribution. Thus, when it is multiplied by $\hat{v}$ (cf. Fig. 5.4 c)), which is symmetric with respect to the flame midline, an anti-symmetric pattern is obtained.

A very similar distribution compared to $\hat{q}_\Delta$ is observed for $\langle RI_\Delta \rangle$ (cf. Fig. 5.9 d)). As long as the $\langle RI_\Delta \rangle$ distribution shows negative and positive areas an a priori prediction about whether $\hat{q}_\Delta$ introduces driving cannot be made.

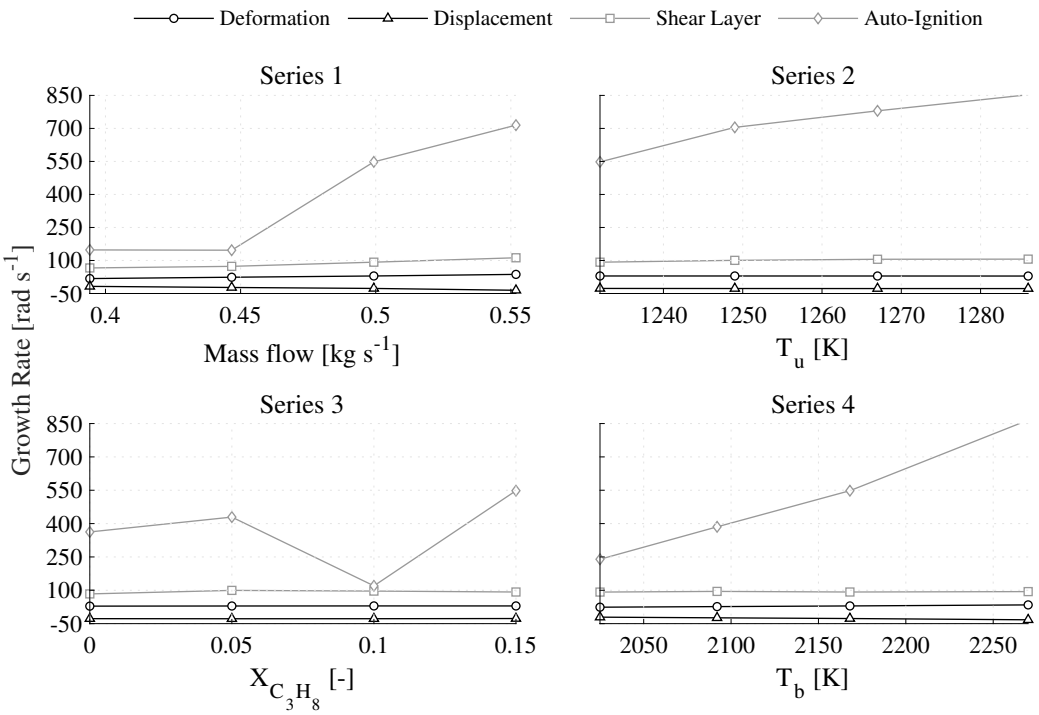

Figure 5.10: *Growth rates of the corresponding series for deformation, displacement, convective modulation of reactive shear layer (Shear Layer) and acoustic modulation of auto-ignition time delay (Auto-Ignition). Deformation and displacement results are highlighted in black.*

The computed growth rates for the deformation and displacement mechanisms are plotted in Fig. 5.10 against the varied control parameter in each experimental series (cf. Tab. E.1). In Fig. 5.10, it is observed that the deformation mechanism induces driving, as expected from its Rayleigh index (cf. Fig. 5.9 b)), whereas the displacement mechanism generates damping. The displacement mechanism can provoke damping depending on the morphology of the flame and its position with respect to the acoustic mode as shown in [91]. Specifically, for T1 modes in which the flame is a thin brush located within the upper quarter of the chamber, as it is the case of the reheat combustor, damping is obtained [91]. The second conclusion that can be drawn from Fig. 5.10 is that driving due to deformation and damping due to displacement is more intense in Series 1 and 4. This can be ascribed to an increased intensity of the mean heat release and consequently, the gradients of mean heat release. For Series 1 mean heat release in the reheat flame increases as a result of an increased air mass flow. On the other hand, in Series 4, heat release increases due to an increase in fuel mass flow, cf. Tab. E.1.

Finally, for all studied series, the net effect of deformation and displacement mechanisms almost cancels out. Therefore, their relevance on driving the instability is secondary.

5.2.2 Driving due to Convective Modulation of the Reactive Shear Layer

Experiments in the reheat combustor hinted a convective modulation of heat release in the reactive shear layers [31]. Acoustically induced vortex shedding transports hot combustion products into the cold reactants and vice versa [92]. This effect ultimately modulates the heat release in the reactive shear layer.

In this section, first the transport mechanism of hot products and cold reactants is explained in detail. Then, the spatial distribution of unsteady heat release due to convective modulation in the shear layer ($\hat{q}_c$) (cf. Eq. 2.66) is shown in Fig. 5.12 a). Furthermore, the Rayleigh index for this mechanism $\langle RI_c \rangle$ is depicted in Fig. 5.12 b). Finally, computed growth rates due to $\hat{q}_c$ for all available operating points (cf. Tab. E.1) are plotted in Fig. 5.13.

After the sudden area jump at the combustor inlet, an acoustically induced series of counter-rotating vortices is formed, cf. schematic in Fig. 5.11 a). Looking in more detail at this phenomenon, it is observed that between consecutive vortices, the velocity field of each vortex overlaps and as a result, increased velocity perpendicular to the shear layer, is obtained between vortices. As the vortices are counter-rotating, the ”inter-vortical” velocity changes alternatively its direction. This reinforced inter-vortical velocity transports hot products and cold reactants across the shear layer, cf. Fig. 5.11 a). As a result, a characteristic pattern of alternative hot products and cold reactants patches appears over the shear layer. Ultimately, patches of cold reactants that contain fresh gas imply increased heat release. On the other hand, patches of hot products, where the combustion reaction is complete, imply lower heat release.

Within the framework of premixed combustion, the progress variable determines the progress of reaction and therefore which parts of the flow are burned or unburned. Therefore, by solving a linearized transport equation for the progress

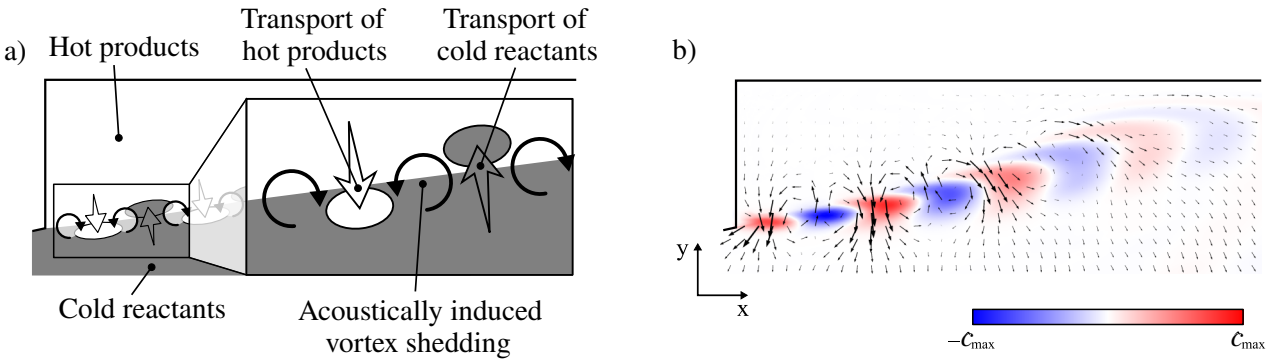

Figure 5.11: *a) Schematic of vortical transport of hot products and cold reactants at the shear layer. b) Perturbation progress variable and perturbation velocity field (arrows).*

variable (cf. Eq. 2.64), it is possible to obtain a distribution of the perturbation progress variable $\hat{c}$, which is modulated by acoustically induced vortex shedding. This result is shown in Fig. 5.11 b). There, positive values of $\hat{c}$ represent hot product patches and negative values of $\hat{c}$ cold reactant patches. The overlaid arrows in Fig. 5.11 b) represent the perturbation velocity field. This confirms that the inter-vortical velocity is responsible for the transport of products and reactants.

The unsteady heat release $\hat{q}_c$ (cf. Eq. 2.66) is obtained as a function of $\hat{c}$ by linearizing the mean reaction rate of the propagation stabilized flame zones (cf. Eq. 2.18). The spatial distribution of $\hat{q}_c$ is shown in Fig. 5.12 a). Qualitatively, some dispersion of the patches due to mean flow shear dispersion is noticed. Furthermore, by comparing the distribution of $\hat{q}_c$ to the distribution of $\hat{c}$ in Fig. 5.11 b), it is recognized a similar structure with an opposite sign. Therefore, as expected, in patches of positive $\hat{c}$ the combustion reaction has advanced and $\hat{q}_c$ is negative and in patches of negative $\hat{c}$, $\hat{q}_c$ is positive. Finally, the Rayleigh index of $\hat{q}_c$ is depicted in Fig. 5.12 b). A very similar distribution compared to $\hat{q}_c$ is observed for $\langle RI_c \rangle$, cf. Fig. 5.9 d). As long as, $\langle RI_c \rangle$ shows negative and positive areas an a priori prediction about whether $\hat{q}_c$ introduces driving cannot be made.

The computed growth rates for the convective modulation of reaction rate mechanism are plotted in Fig. 5.13 against the varied control parameter in each experimental series (cf. Tab. E.1).

In Fig. 5.13, it is observed that $\hat{q}_c$ induces driving. Specifically, driving grows

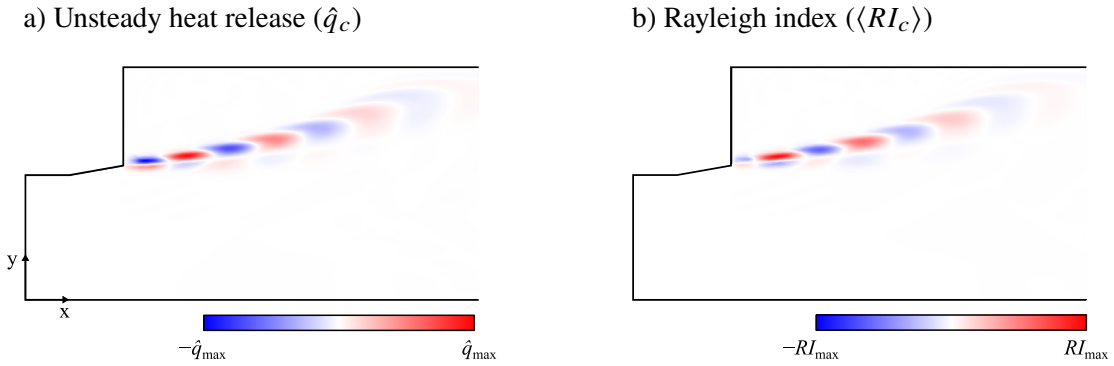

Figure 5.12: *Real part of unsteady heat release a) and period-averaged Rayleigh index b) for convective modulation of the reactive shear layer. Results for OP-01.*

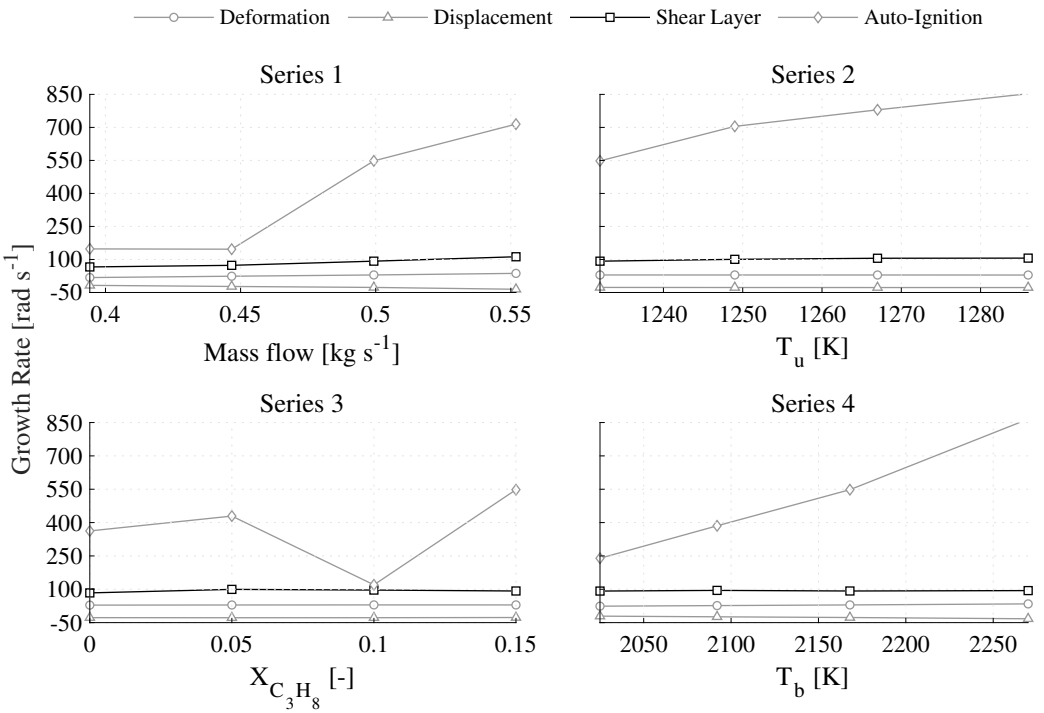

Figure 5.13: *Growth rates of the corresponding series for deformation, displacement, convective modulation of reactive shear layer (Shear-Layer) and acoustic modulation of auto-ignition time delay (Auto-Ignition). Convective modulation of reaction rate results are highlighted in black.*

in Series 1 for increasing mass flow. Increasing mass flow entails higher mean velocities at the shear layer and therefore vortex shedding strengthens. This in turn enhances the convective transport of products and reactants across the shear layer and increases the heat release modulation. For Series 2, 3 and 4, mass flow is constant, and accordingly, growth rates for those series are essentially constant.

Finally, it is observed that convective modulation at the shear layer is a relevant driving mechanism in the studied configuration (cf. Fig. 5.13). Specifically, growth rates due to convective modulation in the shear layer are about three times stronger than those due to deformation. Still, driving due to convective modulation is about one order of magnitude smaller than driving due to convective modulation of the auto-ignition time delay. The latter mechanism will be analyzed in detail in the next section.

5.2.3 Driving due to Acoustic Modulation of the Auto-Ignition Time Delay

The auto-ignition time delay determines the position of the auto-ignition stabilized flame front in reheat flames. The auto-ignition time delay is a function of temperature and density (cf. Eq. 2.26). Thus, fluctuations of those quantities lead to modulation of the auto-ignition time delay, which in turn alters the flame front position and ultimately modifies the heat release.

In this section, first the acoustic modulation of the auto-ignition time delay ($\hat{t}_{\mathrm{ign}}$) is shown in Fig. 5.14. Then, the corresponding fluctuating displacement fields are depicted in Fig. 5.15. The unsteady heat release distribution $\hat{q}_{\mathrm{AI}}$ (cf. Eq. 2.79) associated with the previously mentioned displacement fields is shown in Fig. 5.16 a). Additionally, the Rayleigh index derived from $\hat{q}_{\mathrm{AI}}$, i.e. $\langle RI_{\mathrm{AI}} \rangle$ is depicted in Fig. 5.16 b). Finally, computed growth rates arising from $\hat{q}_{\mathrm{AI}}$ for all available operating points (cf. Tab. E.1) are plotted in Fig. 5.17.

Modulation of the flame front displacement is calculated by solving the corresponding linearized transport Eq. 2.72. That equation can be physically interpreted as a purely convective transport equation of the displacement with a source term that is proportional to the local auto-ignition time delay $\hat{t}_{\mathrm{ign}}$. In Fig. 5.14,

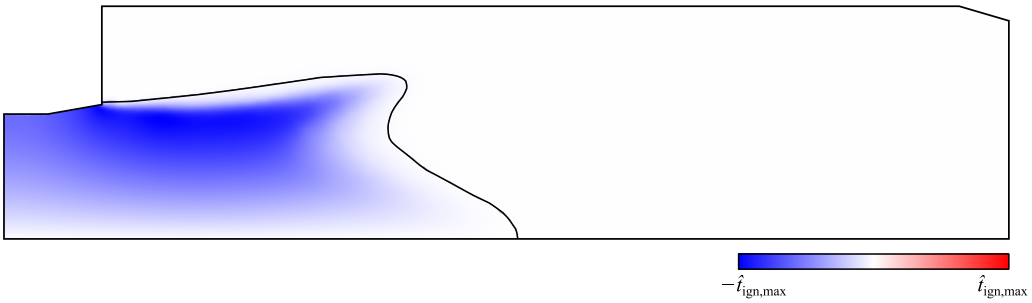

Figure 5.14: *Real part of fluctuating auto-ignition time delay* $\mathrm{Re}(\hat{t}_{\mathrm{ign}})$. *Isoline* $\bar{c} = 0.5$ *(—), representative of the flame front position. Results for OP-01.*

$\hat{t}_{\mathrm{ign}}$ is depicted. It can be observed negative modulation of $\hat{t}_{\mathrm{ign}}$ for the studied T1 mode, which features positive pressure close to the faceplate of the chamber, cf. Fig. 5.4 a). It implies that the local auto-ignition time delay decreases for positive values of pressure. This is expected as increasing pressure accelerates the auto-ignition reaction. Decrease of $\hat{t}_{\mathrm{ign}}$ with increasing $\hat{p}$ can be further corroborated from the linearized empirical correlation of $\hat{t}_{\mathrm{ign}}$, Eq. 2.73. There, it can be seen that ultimately $\hat{t}_{\mathrm{ign}}$ is a function of $\hat{p}$ only, if perturbation density and temperature are assumed isentropic. Therefore, $\hat{t}_{\mathrm{ign}}$ reflects the T1 eigenmode pressure distribution with opposite sign. Finally, note that fluctuations of $\hat{t}_{\mathrm{ign}}$ downstream of the flame are not visible in Fig. 5.14 due to high mean flow temperatures of the products. Mean auto-ignition time delay decreases exponentially with temperature and therefore the linear fluctuations of $\hat{t}_{\mathrm{ign}}$ after the flame are some orders of magnitude smaller than upstream of the flame.

From $\hat{t}_{\mathrm{ign}}$ fluctuations arise $\hat{\boldsymbol{x}}_{\mathrm{f}}$ fluctuations, which are depicted in Figs. 5.15 a) and b) for x- and y-directions, respectively. These fields are obtained after solving Eq. 2.70 with Neumann boundary conditions –i.e $\partial \hat{x}_{\mathrm{f}}/\partial x = 0$ and $\partial \hat{y}_{\mathrm{f}}/\partial x = 0$ at the inlet. These boundary conditions are selected because the pressure mode starts already in the mixing channel, cf. Fig. 5.4 a). There, it is observed that pressure is not zero at the inlet. Consequently, the auto-ignition time delay modulation starts already at the end of the mixing channel as $\hat{t}_{\mathrm{ign}}$ is active there, cf. e.g. Fig. 5.14. Neumann boundary conditions allow that the solution for flame front displacement has a non-zero value at the inlet so that value can adapt itself to the displacement field and be consistent with it. If a Dirichlet boundary condition was applied at the inlet, it would imply that the oscillating displacement field

would have always a node at the inlet, disregarding the history of a fluid particle throughout its flying path from injection until the flame front.

At first glance, it is observed in Fig. 5.15 that the qualitative magnitude of displacement is more intense in x-direction as the mean flow is dominant in that direction. Note that magnitude comparison between Figs. 5.15 a) and b) is possible because color scales have the same maximum and minimum values. Moreover, two characteristic zones are recognized in the displacement plots. First, upstream of the flame, where the source term is active and dominates in the governing Eq. 2.70, a zone with almost constant intensity is noticeable. This means that the flame front tends to move to areas of reduced $\hat{t}_{\mathrm{ign}}$. Downstream of the flame, as long as there is no source active, a convective pattern is visible. The convective pattern is more clearly recognizable on the one-dimensional plot depicted in Fig. 5.15 c). The convective character of that pattern is further confirmed by analytically estimating the convective wavelength. The convective wavelength in x-direction ($\lambda_{x,\mathrm{c}}$) can be estimated by the quotient between horizontal mean flow velocity and frequency $\lambda_{x,\mathrm{c}} = \bar{u}/f$. Introducing representative mean flow velocity values – i.e. $\bar{u} = 100\,\mathrm{m\,s^{-1}}$ and $f = 1600\,\mathrm{Hz}$, $\lambda_{x,\mathrm{c}} \approx 6 \times 10^{-2}\,\mathrm{m}$ is obtained. Note that the analysis focuses on the horizontal component of displacement only, as it is the dominant motion. The wavelength estimation can be compared to Fig. 5.15 c), where the wavelength scale is depicted. Simulated and analytically calculated values of convective wavelength of $\hat{x}_{\mathrm{f}}$ match, which confirms the convective character of the simulated unsteady flame front displacement. Regarding the actual displacement values, in the theory Section 2.4.3.1 where the displacement model was presented, it was analytically estimated that the order of magnitude of $\hat{x}_{\mathrm{f}}$ is about 2 cm. This estimation is further confirmed by the FEM simulations shown in Figs. 5.15 a) and b). There, the originally non-dimensional simulated fields have been scaled using the maximum experimental pressure (approximately 2000 kPa for OP-01) in order to obtain dimensional values of displacement. At the auto-ignition stabilized flame front, which is highlighted with red contours in Figs. 5.15 a) and b), displacement agrees with the analytic estimation. Finally, also note that some modulation of displacement field arises at the shear layer region. This is due to the high intensity of mean flow velocity gradients in that area close to the recirculation zone.

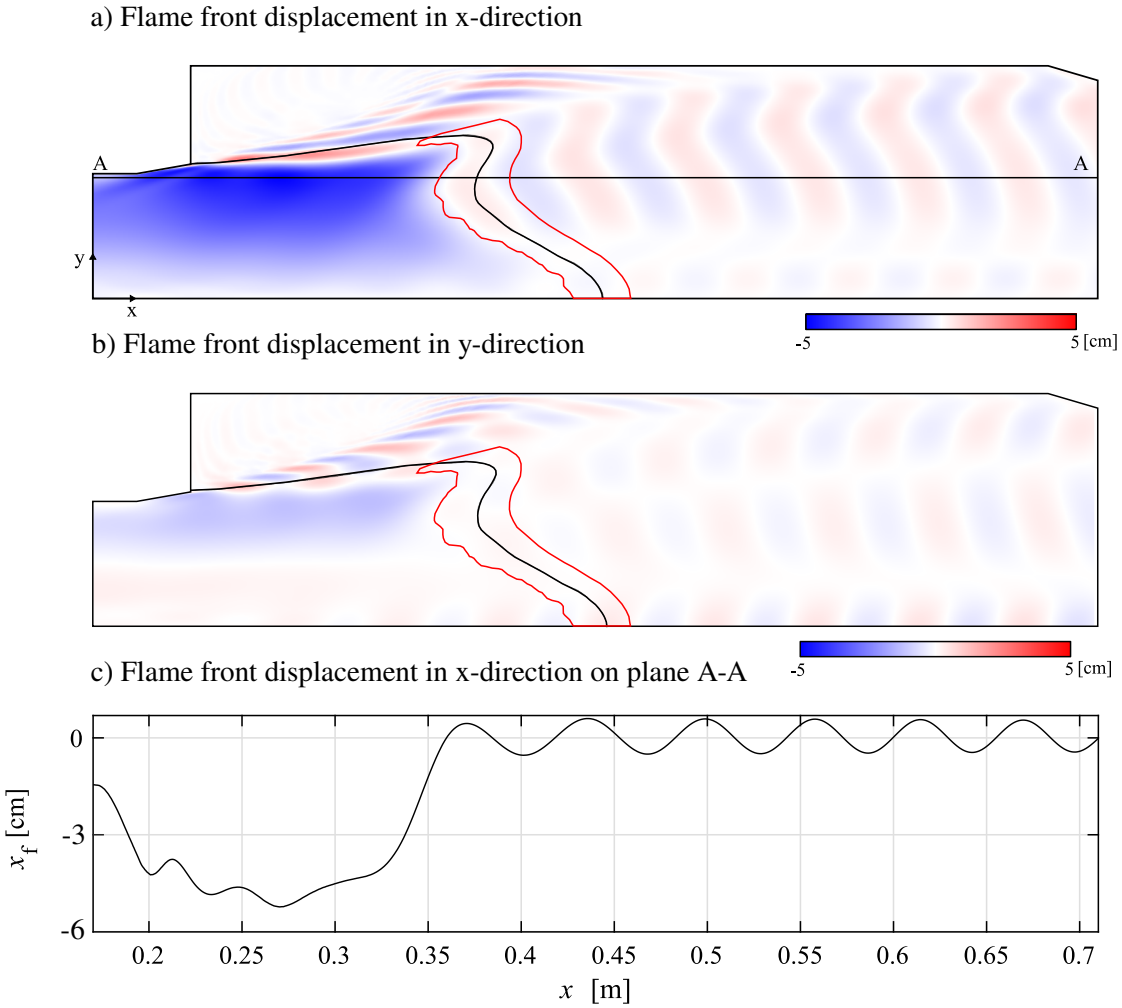

Figure 5.15: *Real part of fluctuating flame front displacement in x- and y-directions,* $\mathrm{Re}(\hat{x}_f)$ *and* $\mathrm{Re}(\hat{y}_f)$ *in Figs. a) and b). Isoline* $\bar{c} = 0.5$ *(—), representative of the flame front position. Isoline* $\bar{q} = 0.4\ \bar{q}_{\mathrm{ai,max}}$ *(—) represents the approximate contour of the auto-ignition stabilized flame front. Flame front displacement in x-direction in section plane A-A represented in Fig. c). Results for OP-01.*

Once the flame front displacement fields have been discussed, the focus is put on the unsteady heat release due to auto-ignition ($\hat{q}_{\mathrm{AI}}$). Both, flame front displacement and unsteady heat release are related via Eq. 2.79. Consequently, such an equation is used as basis of the subsequent analysis. The dominant term in $\hat{q}_{\mathrm{AI}}$ is mainly proportional to $\partial\hat{\boldsymbol{x}}_{\mathrm{f}}/\partial t$ as velocity and density fields present low values at the position of the auto-ignition flame front. Specifically, velocity oscillations are most intense at the shear layer region. Similarly, density under the isentropic assumption follows the pressure field and it is more intense towards the chamber

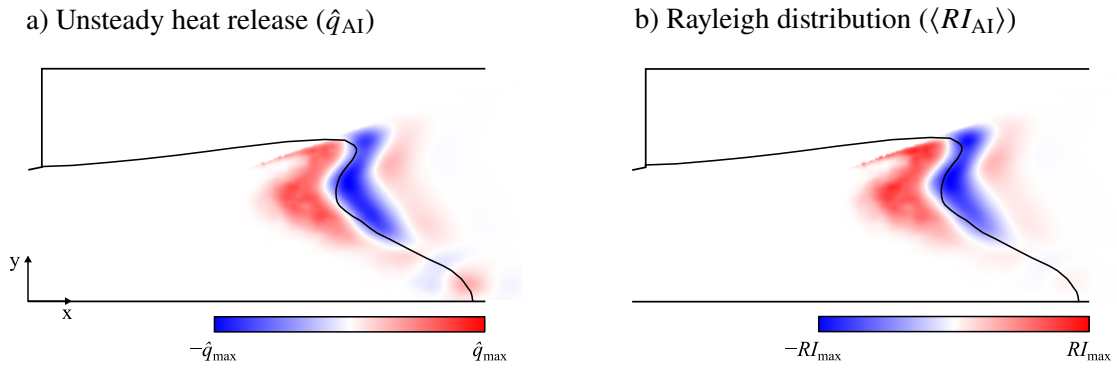

Figure 5.16: *Real part of unsteady heat release a) and period-averaged Rayleigh index b) for acoustic modulation of auto-ignition time delay mechanism. Isoline $\bar{c} = 0.5$ (—), representative of the flame front position. Results for OP-01.*

faceplate. Therefore, as hinted before the dominant term remains the temporal partial derivative of flame displacement which is dominant at the flame front, where auto-ignition is predominant.

As seen in Fig. 5.15 a), when $\hat{p}$ is positive the flame front tends to move to areas of reduced $\hat{t}_{\mathrm{ign}}$. Therefore, the flame front oscillates around its mean position. The flame moves towards the faceplate in positive pressure cycles and viceversa. For premixed flames, energy integrated over the flame volume is conserved for the moving flame [15]. As a result, the flame zone shows positive and negative distributions of unsteady heat release, cf. Fig. 5.16 a). In Fig. 4.5, it is also worth noting that $\hat{q}_{\mathrm{AI}}$ tails that should appear near to the shear layer following the mean heat release distribution $\bar{q}_{\mathrm{AI}}$ (cf. e.g. Fig. 4.5) are filtered out. This prevents the appearance of $\hat{q}_{\mathrm{AI}}$ singularities that pollute the numerical solution. The Rayleigh index $\langle RI_{\mathrm{AI}} \rangle$ is depicted in Fig. 5.16 b). It presents a similar spatial distribution compared with $\hat{q}_{\mathrm{AI}}$. However, $\langle RI_{\mathrm{AI}} \rangle$ shows some attenuation towards the centerline of the chamber due to the effect of the pressure eigenmode, which has a pressure node at the centerline. Furthermore, the Rayleigh index is predominately positive so it can be inferred that this mechanism induces driving.

The driving potential is confirmed by analyzing the computed growth rates plotted in Fig. 5.17 against the varied control parameter in each experimental series, cf. Tab. E.1. For all operating points driving is obtained. In fact, driving due to modulation of the auto-ignition time delay is the largest of all mechanisms analyzed. Specifically, it is seen in Fig. 5.17 that growth rates due to auto-ignition

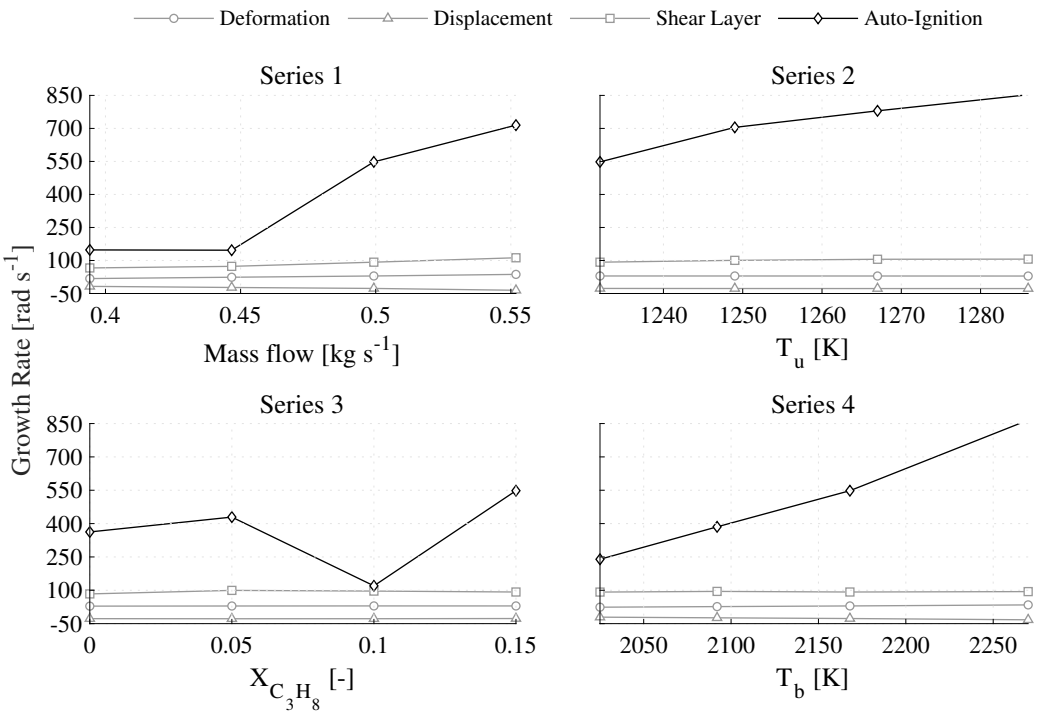

Figure 5.17: *Growth rates of the corresponding series of measurements for deformation, displacement, convective modulation of reactive shear layer (Shear layer) and acoustic modulation of auto-ignition time delay (Auto-Ignition).*

mechanism are about one order of magnitude larger than the other mechanisms. This is due to the fact that most of flame's heat is released in auto-ignition stabilized zones.

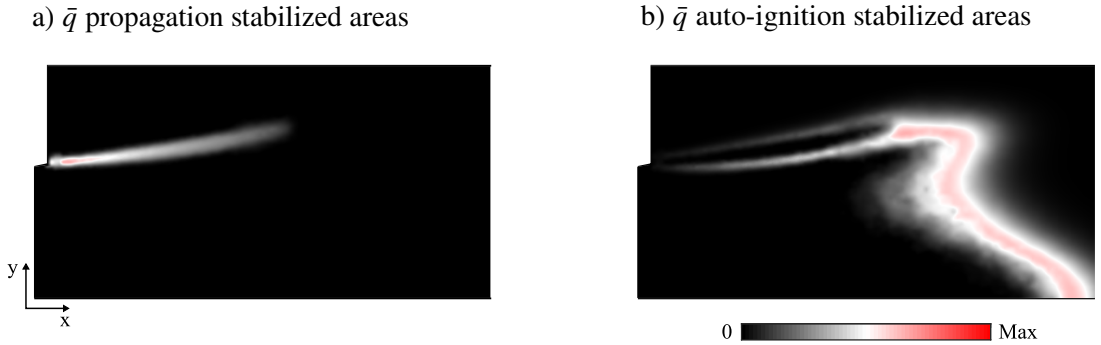

Figure 5.18: *Normalized volumetric heat release areas stabilized via propagation in a) and stabilized via auto-ignition in b). Results for OP-01.*

This can be observed again in Figs. 5.18 a) and b) where mean heat release for propagation and auto-ignition stabilized zones is separately depicted. There,

auto-ignition zones are way larger than propagation ones. As heat release density is similar, see color scale in Fig. 5.18, total heat release due to auto-ignition is also larger. Specifically, after volume integration of $\bar{q}_{\mathrm{AI}}$ for each characteristic zone it can be seen that about 90% of $\bar{q}_{\mathrm{AI}}$ is released at auto-ignition stabilized zones.

By taking this into account, it can be concluded that auto-ignition coupling has a driving potential per unit of mean heat release in the same order of magnitude as propagation related mechanisms –i.e. deformation, displacement and convective modulation of the shear layer. It is therefore the sheer amount of heat released at flame's auto-ignition stabilized areas which explains the difference between auto-ignition growth rates and the other mechanisms. These results are in line with previous models of coupling between acoustics and auto-ignition like the pressure sensitivity model derived by Zellhuber in [28]. There, different coupling mechanisms for reheat flames are discussed. Among them, the so-called pressure sensitivity captures the influence of acoustics on auto-ignition reaction. In terms of magnitude, based on its theoretical expression it can be followed that pressure sensitivity is in the same order of magnitude as deformation. This result is well reproduced with the auto-ignition coupling model presented in the current section.

5.2.4 Conclusions on Driving Mechanisms

Due to the linearity of all derived mechanisms, the total unsteady heat release ($\hat{q}$) can be obtained by simply adding all its individual contributions. Then, $\hat{q}$ can be compared to readily available phase-resolved CH^* CL images, which are representative of the flame dynamics in the combustion chamber.

A comparison of the simulated $\hat{q} = \hat{q}_\rho + \hat{q}_\Delta + \hat{q}_c + \hat{q}_{\mathrm{AI}}$ to their experimental counterparts is shown in Figs. 5.19 a) and b). Overall, qualitatively good agreement is found, cf. Fig. 5.19 a). The sequence of alternating patches is reproduced. A more detailed comparison of length and position of the alternating patches is performed in Fig. 5.19 b) by overlaying the contours of the simulated heat release onto the experimental images. By inspecting Fig. 5.19 b), it is observed best agreement in length for the three first patches. Subsequently, the length of the simulated patches is underestimated, likely due to the lack of turbulent diffusion.

LEE can only capture shear dispersion due to interactions with the mean flow, but this alone is insufficient to reproduce the increasing lengths of the patches caused by progressive diffusion. Similarly, the transverse dimension of the patches is underestimated in the simulations. In addition to the lack of turbulent diffusion, the reduced thickness in $\hat{q}$ can be ascribed to the reduced thickness of the flame brush in the mean flow reactive simulations due to not considering effects of flame stretch (cf. Section 4.3.2).

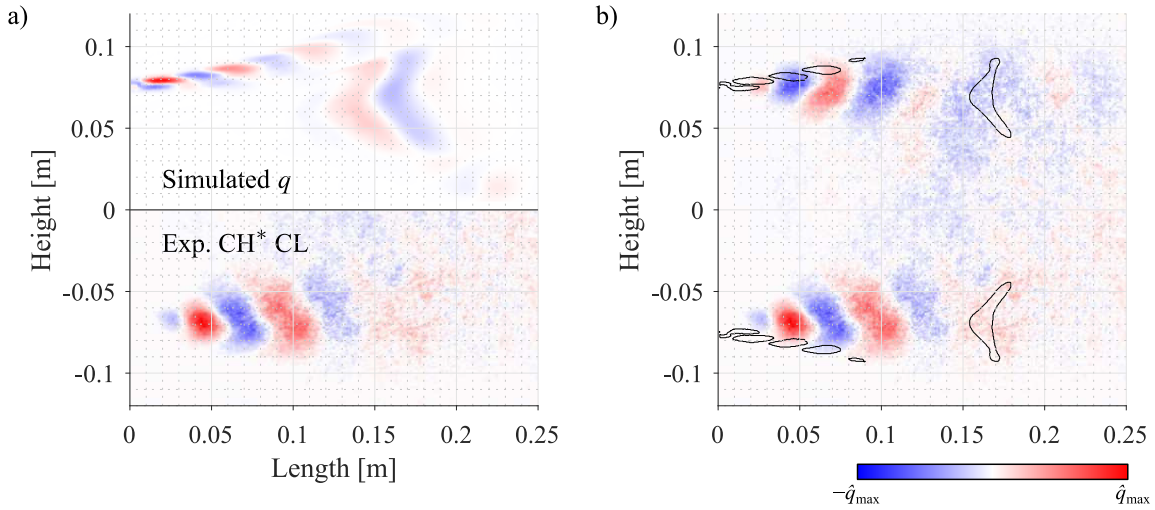

Figure 5.19: *a) Comparison of simulated unsteady heat release ($\hat{q}$) obtained by superposition of $\hat{q}_\rho$, $\hat{q}_\Delta$, $\hat{q}_c$ and $\hat{q}_{\mathrm{AI}}$ (top) and phase-resolved CH* CL (bottom). b) Comparison of simulated unsteady heat release (—) and phase-resolved CH* CL. CH* CL images were kindly provided by Jonathan McClure.*

Finally, as a summary of this section concerned with driving assessment, the following conclusions regarding driving mechanisms of the T1 mode in the reheat combustor can be drawn:

- Good agreement is found between simulated spatial distributions of $\hat{q}$ and the corresponding phase-resolved CH* CL images. Specifically, the characteristic alternating pattern of unsteady heat release observed in the experiments is reproduced by superposition of all individual coupling mechanisms. This reveals that the relevant coupling mechanisms between flame and acoustics are considered.
- The sum of driving due to deformation and displacement mechanisms has an almost neutral effect on stability of the T1 mode. This is explained by the fact

that the thermoacoustic driving introduced by the deformation mechanism is compensated by the effect of the displacement mechanism.

- Driving due to convective modulation of the shear layer is a relevant driving mechanism for the T1 mode. Furthermore, for increasing mean mass flow, the intensity of driving increases due to the strengthening of acoustically induced vortex shedding.
- Driving due to acoustic modulation of the auto-ignition time delay is the strongest of all analyzed coupling mechanisms. Its contribution to the total driving rate is about one order of magnitude larger than the convective modulation of the shear layer. The sheer amount of heat released in the auto-ignition stabilized zones of the flame explains the important influence of this mechanism on the driving rates.

The good qualitative agreement between experiments and simulations in Fig. 5.19 indicates that most of the relevant mechanisms are already described. Still, there is the possibility that the shear layer is also modulated by equivalence ratio fluctuations [31]. The employed methodology could be extended to account for the effects of equivalence ratio fluctuations as follows. The first step would be to carry out non-premixed reactive mean flow simulations from which mean fields of any variable that accounts for unmixedness are obtained e.g. mixture fraction. Then, a linearized transport equation for the mixture fraction is required. In such an equation, the source term should correspond to acoustically modulated fuel injection. Effects of unmixedness from the first combustion stage could be taken into account with appropriate inlet boundary conditions. By solving the linearized transport equation, a perturbation mixture fraction field would be obtained. The latter could be directly linked to heat release fluctuations. This mechanism could be particularly relevant for eigenmodes in which acoustic perturbations reach the mixing section thus modulating the mixture fraction.

5.3 Net Thermoacoustic Growth Rates

Finally, for the 16 operating points, all contributions of damping and driving are added up to obtain the net growth rate that determines the linear thermoacoustic

stability of the reheat combustor's T1 mode. The net growth rates (white symbols) with their individual contributions of driving mechanisms (reddish bars) and damping (bluish bars) are represented in Fig. 5.20. Finally, experimental damping rates estimated using Lorentzian fitting of the power spectral density of pressure time traces (cf. Appendix H for further detail on Lorentzian fitting procedure) are represented with black circles.

The following outcomes concerning thermoacoustic stability can be retrieved from scrutinizing Fig. 5.20:

- All simulated operating points yield strongly positive net growth rates. Therefore, all of them are linearly unstable. This is not in line with experimental observations of the T1 mode in the reheat combustor, for which the operating points show intermittent behavior between stable and unstable condition [35]. Intermittency is a precursor of self-sustained thermoacoustic instability [93] and it is thus associated with small negative growth rates contrary to those obtained from the simulations.
- Despite the obtained linear instability, strong driving and damping mechanisms are present in the experiment, especially at the shear layers. Damping due to acoustic boundary layer is still relevant as it is in the same order of magnitude as driving mechanisms like deformation.
- Linear instability can be mostly attributed to the driving potential due to auto-ignition as it is almost one order of magnitude larger than convective modulation of the reactive shear layer, which is the second coupling mechanism in order of importance. Relevance of auto-ignition coupling is even larger when compared to deformation and displacement together because these both almost cancel out each other as displacement adds damping in the current configuration.

The resulting mismatch between simulated and experimental growth rates could be ascribed essentially to the following causes: insufficient quality of the CFD that produces the auto-ignition mean heat release distribution and disregard of three-dimensional effects when accounting for damping induced by interactions between acoustics and mean flow.

As hinted at the end of Chapter 4, which deals with the reactive CFD simulations, some more work may have to be put into the auto-ignition CFD model in order to obtain a more detailed heat release distribution. This is crucial for the auto-ignition coupling model as it is highly dependent on local heat release distribution as it interacts with convective patterns that are relatively small in scale and therefore interplay between them affect largely the final growth rate. Another potential improvement for the current auto-ignition coupling model is considering a thick flame. Current model is based on the assumption that the flame is an infinitely thin interface. This allows to straightforwardly derive a kinematic balance across flame interface (cf. e.g. Eq. 2.77) that relates burning speed with the time derivative of the flame front position and the perturbation velocity. However, in the case of a thick flame this simple balance does not apply anymore and it has to be revisited.

Furthermore, it is likely that damping mechanisms are underestimated due to the two-dimensional combustion chamber assumption. For the real three-dimensional configuration the rotating mean flow induced by the vortex generators upstream of the reheat combustion chamber may be inserting significant damping that cannot be taken into account with a two-dimensional approach. Also, there exists a small area jump in the shorter dimension of the chamber as the mixing channel is slightly narrower than the sequential combustion chamber (cf. planes XZ in Fig. 3.2). This forms recirculation zones in the XZ plane, which despite being shorter than those formed in XY planes, may introduce relevant damping based on the fact that significant acoustic dissipation can occur within short distances. This effect again cannot be assessed with the current two-dimensional simulations. These topics should be addressed in future work for obtaining growth rates that reproduce the experiments better.

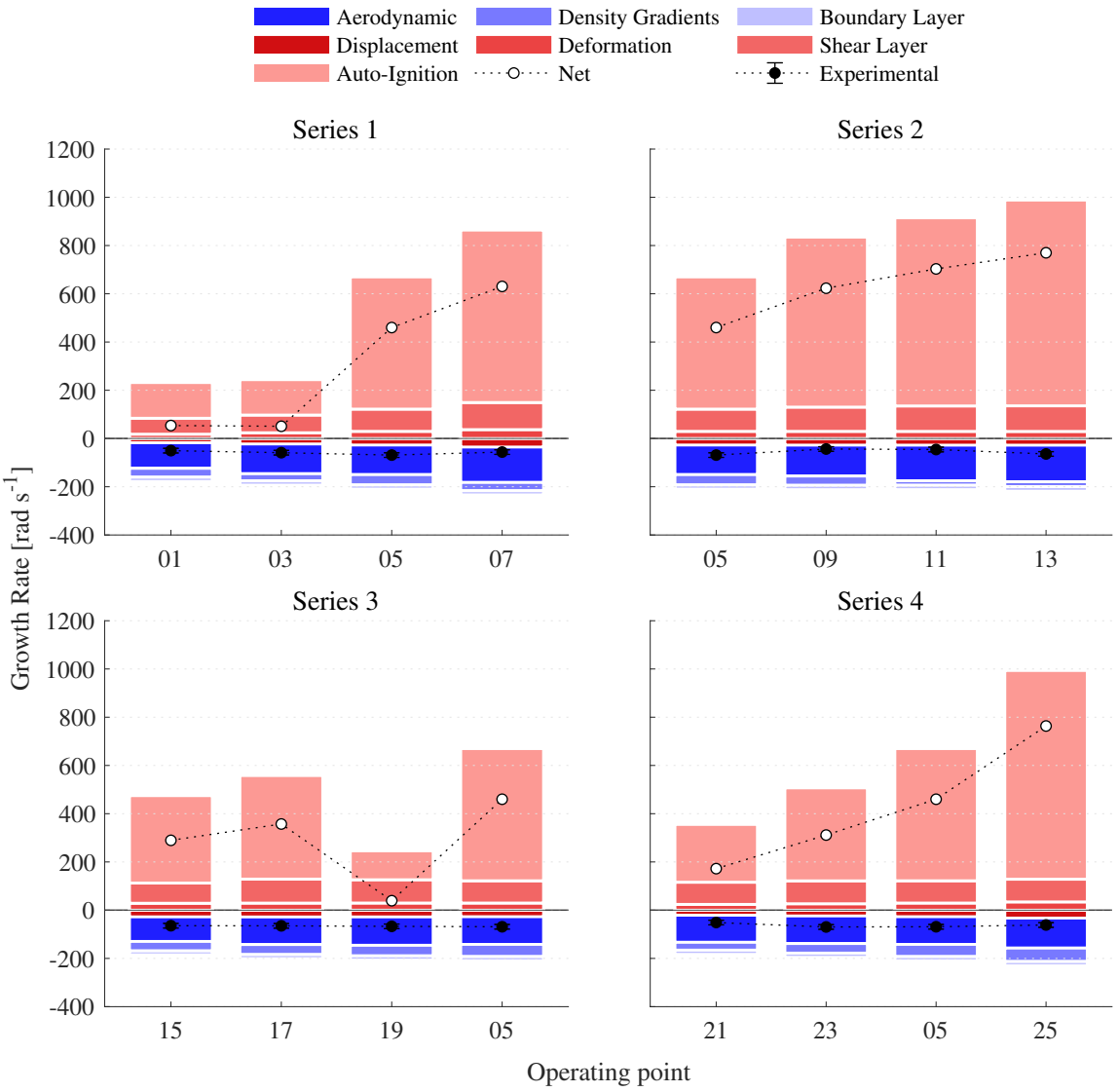

Figure 5.20: *Damping rates (bluish bars) due to: Acoustically induced vortex shedding ("Aerodynamic" in the legend, cf. Section 5.1.2), interactions with non-homentropic mean flow ("Density Gradients", cf. Section 5.1.2) and acoustic boundary layer ("Boundary Layer", cf. Section 5.1.1). Driving rates (reddish bars) due to: Deformation and displacement mechanisms (cf. Section 5.2.1), convective modulation of the reactive shear layer ("Shear Layer", cf. Section 5.2.2) and acoustic modulation of the auto-ignition time delay ("Auto-Ignition", cf. Section 5.2.3). Net growth rate is shown with white circles. Experimental growth rates and corresponding error estimation are depicted with black circles.*

6 Summary, Conclusions and Future Work

In this work, the thermoacoustic linear stability limits of the first transverse (T1) eigenmode of a lab-scale reheat combustor were assessed using a hybrid Computational Fluid Dynamics/Computational Aeroacoustics (CFD/CAA) methodology. The analysis was based on eigenfrequency and growth rate computations with the Linearized Euler equations (LEE), which were solved using a stabilized Finite Element Method.

Hybrid CFD/CAA methods require three elements: governing equations for linear acoustic motion, a stationary mean flow and models for linear thermoacoustic coupling between flame and acoustics. In the present work, the three of them were addressed.

First, a set of isentropic LEE was derived by decomposing the LEE into their isentropic and non-isentropic contributions. In the isentropic LEE, only acoustic and vortical modes propagate. These equations can be applied to combustors with highly turbulent flows, for which entropy waves are unimportant for thermoacoustic stability analysis and direct application of non-isentropic LEE leads to an overestimation of entropy waves. Furthermore, appropriate boundary conditions to account for the damping due to the acoustic boundary layer without resolving it were also derived. This is significant to systems with high surface-to-volume ratio at high-frequencies, for which boundary layer losses are not negligible.

Future work at theoretical level concerns the derivation of a set of linearized equations which treat the flame region, where gradients of mean flow density and unsteady heat release appear, in a non-isentropic fashion. The rest of the domain

however, should be treated isentropically.

Second, a CFD procedure to obtain reactive mean flow fields of reheat combustion suitable for acoustic simulations was introduced. Different combustion models for the propagation stabilized shear layers and auto-ignition stabilized core of the reheat flame were employed. Specifically, the Bray-Moss-Libby model was implemented for the propagation stabilized shear layers. Additionally, a model based on the convective transport of the auto-ignition time delay was employed for capturing the auto-ignition stabilized core. The CFD procedure was able to reproduce experimentally observed flame lengths and density gradients, which are relevant for the associated thermoacoustic calculations.

Third, a linear flame-acoustics coupling model for convective modulation of unsteady heat release at the reactive shear layers of the reheat flame was derived. The reactive shear layer modulation mechanism is based on the vortical transport of combustion products and reactants across the shear layer. The vortices are product of acoustic interactions between the T1 mode and the shear layer. Furthermore, a second model that accounts for acoustic modulation of the auto-ignition time delay was derived. The auto-ignition time delay is modulated between the combustor inlet and the auto-ignition flame front by perturbations of the acoustic variables. Finally, the flame front drifts away from its balance position modulating ultimately the unsteady heat release.

Further developments of the proposed CFD/CAA methodology should include additional flame-acoustic coupling models that account for equivalence ratio fluctuations. Those mechanisms may be also relevant for thermoacoustic stability of technically premixed systems.

Finally, the proposed methodology was tested against a set of 16 experimental operating points of a lab-scale reheat combustor. For these operating points eigenfrequencies and growth rates were calculated. All simulated operating points were linearly stable as observed in experiments. Furthermore, the following conclusions can be drawn:

- Good agreement is found between simulated spatial distributions of unsteady heat release and the corresponding measurements. Specifically, the

characteristic alternating pattern of unsteady heat release observed in experiments is reproduced by the numerical procedure. This indicates that the relevant coupling mechanisms between flame and acoustics are considered.

- Convective modulation of the reactive shear layer is a relevant driving mechanism. The driving induced increases with increasing mass flow due to reinforcing of the acoustically induced vortex shedding. Driving due to acoustic modulation of the auto-ignition time delay is the largest contribution to driving for the T1 mode. This is explained on the basis of the amount of heat released at the auto-ignition stabilized zones, which is far larger than at propagation stabilized zones.

- Strong damping mechanisms are present in the experiment, mainly at the shear layers and strong driving mechanisms occur at the auto-ignition flame front. The net sum of all of them adds up to positive growth rates which indicate that the simulated operating points are thermoacoustically linearly unstable. This is not congruent with experimental observations which show that the test rig is close to its stability limit.

In pursuance of obtaining a better reproduction of the experimental growth rates, future work is twofold. First, a more detailed representation of the auto-ignition mean heat release distribution is needed. Therefore, some more work has to be put into the reactive CFD model in order to fulfill that objective. Last, the two-dimensional chamber assumption may have to be revisited and eventually take into account the full three-dimensional flow. In this case, special focus has to be placed on the effect on damping of the swirling flow from the vortex generators. Also the small recirculation zones that are formed in the shorter dimension of the flat sequential combustion chamber should be considered as they may introduce relevant damping. By considering these, growth rates more fitting to experiments are expected to be obtained.

Appendices

A Entropy Production due to Interactions of Mean Heat Release and Acoustics

In this appendix it is demonstrated that during an acoustic oscillation cycle the Term 3 of the continuity source (cf. Eq. 2.51) produces a net amount of entropy.

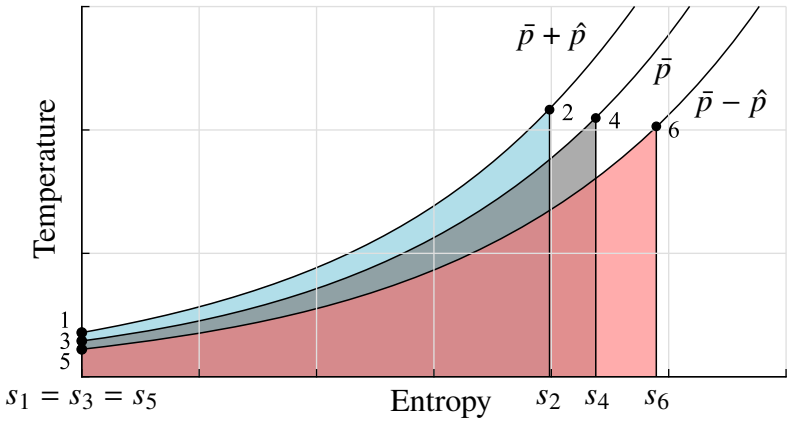

Figure A.1: *T-s diagram displaying constant mean heat release addition at pressure levels $\bar{p} + \hat{p}$, $\bar{p}$ and $\bar{p} - \hat{p}$.*

As starting point, in the T-s diagram (cf. Fig. A.1) States 1 and 5 correspond to oscillatory isentropic increase and decrease of pressure due to acoustics. In the following, only the derivation of the change of state 1 to state 2 is shown as changes of state 3-4 and 5-6 can be derived similarly. Knowing beforehand the mean state 3, the temperature T_1 is given by the isentropic relation of pressures:

$$T_1 = T_3 \left(1 + \frac{\hat{p}}{\bar{p}}\right)^{\frac{\gamma-1}{\gamma}} \approx T_3 \Bigg(1 + \underbrace{\frac{\gamma - 1}{\gamma} \frac{\hat{p}}{\bar{p}}}_{\epsilon}\Bigg) = T_3(1 + \epsilon) \tag{A.1}$$

Note that Eq. A.1 is linearized around the mean state $\bar{p}$ due to smallness of acoustic motion ($\hat{p} \ll \bar{p}$). For the sake of simplicity, small terms are gathered in the variable ϵ. For perfectly premixed flames and small pressure perturbations, the heat released by the flame is constant regardless of the incoming pressure waves. This results in:

$$\bar{q} = \int_{s_3}^{s_4} T_{\bar{p}}(s)\,\mathrm{d}s = \int_{s_1=s_3}^{s_2} T_{\bar{p}+\hat{p}}(s)\,\mathrm{d}s = \int_{s_5=s_3}^{s_6} T_{\bar{p}-\hat{p}}(s)\,\mathrm{d}s \tag{A.2}$$

Furthermore, for low Mach numbers, heat is released in an isobaric process; thus, the temperature $T_{\bar{p}+\hat{p}}$ is given by the following expression for the isobar $\bar{p}+\hat{p}$:

$$T_{\bar{p}+\hat{p}}(s) = T_1 \exp\left(\frac{s-s_3}{c_p}\right) \tag{A.3}$$

The variation of entropy is obtained after integrating Eq. A.2 taking into account the temperature function given by Eq. A.3, resulting in:

$$s_2 - s_1 = c_p \log\left(\frac{\bar{q}}{c_p T_1} + 1\right) \approx c_p \log\left[\frac{\bar{q}}{c_p T_3}(1-\epsilon+\epsilon^2) + 1\right] \tag{A.4}$$

Note that in the last approximation in Eq. A.4, the expression for T_1, Eq. A.1, is introduced. Only deviation of entropy with respect to the mean state 4 is of interest:

$$\begin{aligned}
\frac{\Delta s_{\bar{p}+\hat{p}}}{c_p} &= \frac{s_2 - s_4}{c_p} = \frac{s_2 - s_1}{c_p} - \frac{s_4 - s_1}{c_p} \\
&= \log\left[\frac{\bar{q}}{c_p T_3}(1-\epsilon+\epsilon^2) + 1\right] - \log\left(\frac{\bar{q}}{c_p T_3} + 1\right) \\
&= \log\left[1 + \underbrace{\frac{\bar{q}}{\bar{q} + c_p T_3}}_{=K}(-\epsilon+\epsilon^2)\right] \approx -K\epsilon + \left(K - \frac{K^2}{2}\right)\epsilon^2
\end{aligned} \tag{A.5}$$

where K collects constant terms $\bar{q}$, c_p and T_3. One can proceed similarly for the lower pressure isobar, which gives:

$$\frac{\Delta s_{\bar{p}-\hat{p}}}{c_p} \approx K\epsilon + \left(K - \frac{K^2}{2}\right)\epsilon^2 \tag{A.6}$$

The net entropy production is obtained by adding up both contributions:

$$\frac{\Delta\hat{s}}{c_p} = \frac{\Delta s_{\bar{p}+\hat{p}}}{c_p} + \frac{\Delta s_{\bar{p}-\hat{p}}}{c_p} = \left(2K - K^2\right)\epsilon^2 \tag{A.7}$$

The result in Eq. A.7 can be further refined assuming harmonic oscillations of pressure and averaging over a period. In frequency domain the time-average operation over a period is given by taking the real part of the multiplication of the entropy increment and its complex conjugate:

$$\frac{\overline{\Delta\hat{s}}}{c_p} = \frac{1}{2}\mathrm{Re}\left[\Delta\hat{s}(\Delta\hat{s})^*\right] = \left(K - \frac{K^2}{2}\right)\left(\frac{\gamma-1}{\gamma}\right)^2 \frac{|\hat{p}|^2}{\bar{p}^2} \tag{A.8}$$

where $(\cdot)^*$ represents the complex conjugate and $|\cdot|$ is the module of the complex number, in this case the amplitude of the pressure wave.

B Derivation of a Boundary Condition to Account for Viscous Losses due to the Acoustic Boundary Layer

In this appendix, the derivation of the viscous boundary layer boundary condition is presented. First, a boundary condition for 1D acoustics is derived using the linearized Navier-Stokes equations. Second, the 1D model is extended to 3D using a suitable coordinate transformation. This yields a generic boundary condition that accounts for viscous losses within the acoustic boundary layer. Validation of 1D and 3D boundary conditions against analytic and experimental benchmarks is shown in Appendix C.

The linearized Navier-Stokes equations describe the motion within the acoustic boundary layer. Some assumptions can be made to further simplify them. First, mean flow velocity is not considered because the hydrodynamic boundary layer is much thicker than the acoustic boundary layer. Assuming zero mean flow velocity implies that the mean density gradients are zero. Second, heat conduction is neglected, i.e. $\lambda = 0$. Only viscous dissipation is thus taken into account. Thermal conductive effects can be modeled separately with an acoustic impedance as done in [69]. Finally, the acoustic pressure in the direction normal to the wall is constant as usually assumed in boundary layer analyses. The resulting simplified linearized governing equations are:

$$\mathrm{i}\omega\hat{\rho} + \nabla \cdot (\bar{\rho}\hat{\boldsymbol{u}}) = 0, \tag{B.1}$$

$$\mathrm{i}\omega\bar{\rho}\hat{\boldsymbol{u}} = -\nabla\hat{p} + \mu\nabla^2\hat{\boldsymbol{u}}, \tag{B.2}$$

$$\mathrm{i}\omega\hat{p} + \gamma\bar{p}\,(\nabla \cdot \hat{\boldsymbol{u}}) = 0. \tag{B.3}$$

The boundary layer has a thickness $\delta_\mathrm{v} = \sqrt{2\nu/\omega}$ [69] in the direction normal to the wall (y-direction in Fig. B.1). The length scale in y-direction is very small compared to the length scale in x-direction[i]. Consequently, scale analysis can

[i] Boundary layer thickness compared to the acoustic wavelength is $\delta_\mathrm{v}/\lambda_\mathrm{a} \approx \sqrt{\omega\nu}/\bar{c}$. For gases, they only reach the same order of magnitude for extremely high frequencies $\omega \approx 10 \times 10^{10}\,\mathrm{rad\,s^{-1}}$

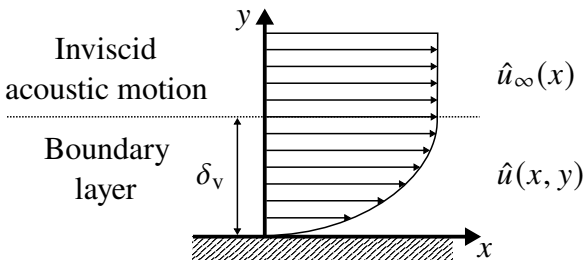

Figure B.1: *Schematic of a 2D acoustic boundary layer*

be carried out, and gradients in directions parallel to the wall can be neglected, further simplifying Eqs. B.1-B.3:

$$\mathrm{i}\omega\hat{\rho} + \bar{\rho}\left(\frac{\partial\hat{u}}{\partial x} + \frac{\partial\hat{v}}{\partial y}\right) = 0, \tag{B.4}$$

$$\mathrm{i}\omega\bar{\rho}\,\hat{u} + \frac{\partial\hat{p}}{\partial x} - \mu\frac{\partial^2\hat{u}}{\partial y^2} = 0, \tag{B.5}$$

$$\frac{\partial\hat{p}}{\partial y} = 0, \tag{B.6}$$

$$\mathrm{i}\omega\hat{p} + \gamma\bar{p}\left(\frac{\partial\hat{u}}{\partial x} + \frac{\partial\hat{v}}{\partial y}\right) = 0. \tag{B.7}$$

Equations B.4 - B.7 describe the acoustic motion within the acoustic boundary layer. Equations for the 1D inviscid motion that occurs outside the boundary layer can be retrieved by setting μ and $\hat{v}$ in Eqs. B.4 - B.7 to zero, yielding:

$$\mathrm{i}\omega\hat{\rho}_\infty + \bar{\rho}\frac{\partial\hat{u}_\infty}{\partial x} = 0, \tag{B.8}$$

$$\mathrm{i}\omega\bar{\rho}\,\hat{u}_\infty + \frac{\partial\hat{p}_\infty}{\partial x} = 0, \tag{B.9}$$

$$\hat{p}_\infty = \bar{c}^2\hat{\rho}_\infty, \tag{B.10}$$

where the subscript $(\cdot)_\infty$ denotes variables outside the boundary layer. According to Eq. B.6, acoustic pressure is constant throughout the boundary layer and its value corresponds to $\hat{p} = \hat{p}_\infty(x)$. Combining Eqs. B.9 and Eq. B.5, a differential equation for $\hat{u}$ is obtained:

$$\mathrm{i}\omega\bar{\rho}\,(\hat{u}-\hat{u}_\infty)=\mu\frac{\partial^2\hat{u}}{\partial y^2}. \tag{B.11}$$

Equation B.11 can be integrated with appropriate boundary conditions: zero velocity at the wall, i.e. $\hat{u}(0)=0$ and the velocity of the inviscid acoustic flow at the upper edge of the boundary layer, i.e. $\hat{u}(\infty)=\hat{u}_\infty(x)$. After integration of Eq. B.11, the velocity profile within the boundary layer (cf. Fig. B.1) is obtained:

$$\hat{u}(x,y)=\hat{u}_\infty(x)\left\{1-\exp\left[-\frac{(1+\mathrm{i})y}{\delta_\mathrm{v}}\right]\right\}, \tag{B.12}$$

In order to determine the velocity in y-direction, $\hat{v}$, the velocity profile Eq. B.12 is introduced into the continuity equation, Eq. B.4. The resulting differential equation is solved with the boundary condition $\hat{v}(0)=0$. The $\hat{v}$-velocity distribution within the boundary layer is:

$$\hat{v}(x,y)=\frac{\partial\hat{u}_\infty}{\partial x}\delta_\mathrm{v}\left(\frac{\mathrm{i}-1}{2}\right)\left\{\exp\left[-\frac{(1+\mathrm{i})y}{\delta_\mathrm{v}}\right]-1\right\}. \tag{B.13}$$

For $y\to\infty$ in Eq. B.13, the velocity at the upper edge of the boundary layer is recovered:

$$\hat{v}(x)=-\frac{\partial\hat{u}_\infty}{\partial x}\delta_\mathrm{v}\left(\frac{\mathrm{i}-1}{2}\right). \tag{B.14}$$

As long as the radius of curvature of the geometry is much larger than the boundary layer thickness, the expression in Eq. B.14 can be extended to 3D configurations by selecting a local system of curvilinear coordinates (cf. Fig B.2). This is safely fulfilled for typical combustor geometries[ii]. Therefore, the boundary layer can be regarded as flat in local coordinates. The vector basis of the curvilinear system is a vector normal to the wall $\boldsymbol{n}$ and a vector parallel to

[ii] Assuming $\nu\approx 1\times10^{-5}\,\mathrm{m^2\,s^{-1}}$; $\omega\approx 1\times10^{4}\,\mathrm{rad\,s^{-1}}$ the acoustic viscous boundary layer thickness (cf. Eq. 2.60) is $\delta_\mathrm{v}\approx 1\times10^{-4}\,\mathrm{m}$

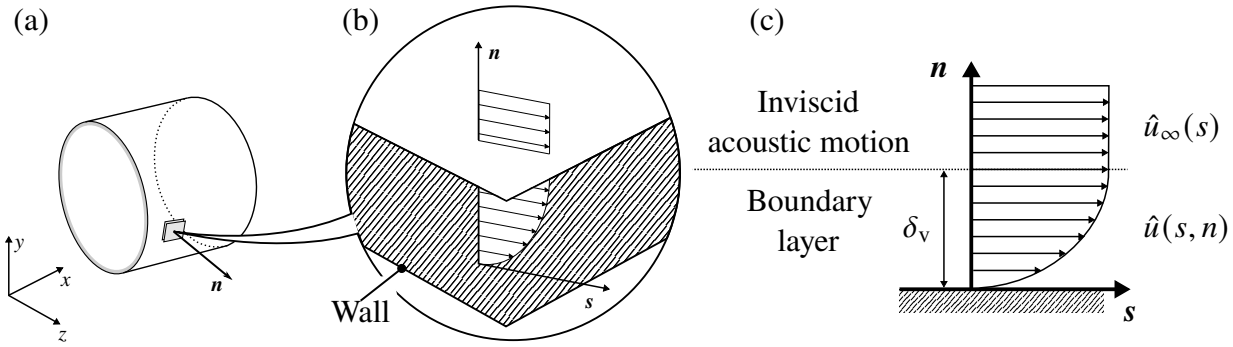

Figure B.2: *(a) Generic geometry (b) Flat boundary layer (c) Velocity profile within the boundary layer*

the direction of the acoustic velocity $\boldsymbol{s}$. The boundary layer structure presented in Fig. B.1 is preserved except for the naming of the coordinates. Hence, integrating the velocity profile, Eq. B.12, along the boundary layer thickness according to the 3D continuity equation:

$$\mathrm{i}\omega\hat{\rho} + \bar{\rho}\left(\nabla_{\boldsymbol{n}} \cdot \hat{\boldsymbol{u}} + \nabla_{\boldsymbol{s}} \cdot \hat{\boldsymbol{u}}\right) = 0, \tag{B.15}$$

the normal velocity at the upper edge of the boundary layer is obtained:

$$\hat{u}_{n,\infty} = -(\nabla_{\boldsymbol{s}} \cdot \hat{\boldsymbol{u}}_\infty)\,\delta_v \left(\frac{\mathrm{i}-1}{2}\right). \tag{B.16}$$

Note that in Eq. B.15 the divergence operator is split into normal and tangential directions. This separates normal and tangent contributions, which allows for integrating along the normal direction only. Equation B.16 can be implemented as boundary condition in the acoustic governing equations.

C Validation of Boundary Conditions Accounting for the Acoustic Boundary Layer

In this appendix, validation of the boundary conditions that account for viscous losses within the acoustic boundary layer (cf. Appendix B) is shown. First, the 1D boundary condition (cf. Eq. B.14) is imposed to a generic tube and its solution compared to analytic baselines. Second, the 3D boundary condition is validated against an experimental benchmark

C.1 Validation of the 1D Boundary Condition

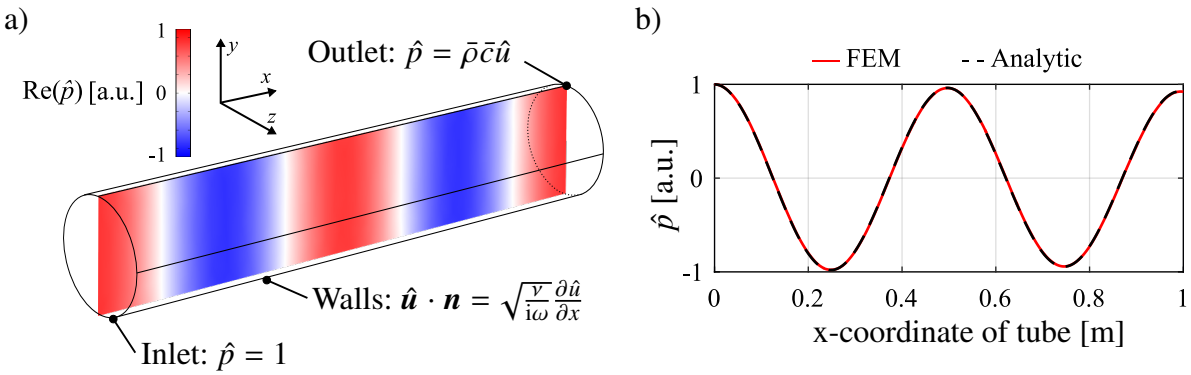

Figure C.1: *(a) Geometry and acoustic pressure (b) Spatial pressure trace from FEM (—), analytic solution from dispersion relation Eq. C.2 (- -)*

A tube of 1 m length and 0.1 m radius is used as test case for the 1D boundary condition validation, cf. Fig C.1 a). Constant bulk pressure and temperature are set to 101 325 Pa and 300 K, respectively. The corresponding kinematic viscosity at 300 K is increased by a factor of 200 to 3.14×10^{-3} m^2 s^{-1} in order to induce noticeable attenuation in the pressure traces. The acoustic field is described by means of the zero-mean-flow LEE (cf. Eqs. B.1-B.3 with $\bar{\boldsymbol{u}} = 0$). The equations are solved via FEM. The computational domain is discretized using an unstructured tetrahedral mesh with a spatial resolution of approximately 13 cells per wavelength. Quadratic Lagrange functions are used as weighting functions in the FEM scheme, which results in approximately 33 000 degrees of freedom.

First, a frequency response study is carried out. At the inlet, the pressure is set to

1 in order to longitudinal excitation, cf. Fig. C.1 a). At the outlet, a non-reflecting boundary condition is imposed –i.e. $\hat{p} - \bar{\rho}\bar{c}\hat{u} = 0$. At the walls, Eq. B.14 is used to include the boundary layer effect,. Then, the zero-mean-flow LEE are solved for a frequency of 694 Hz (third longitudinal mode of the tube)[i]. The one-dimensional pressure field is depicted in Fig. C.1 b). There, one can recognize a slight attenuation between the inlet and the outlet of the tube. In order to assess the accuracy of the computed attenuated pressure trace, it is compared to its analytic solution. For a longitudinal mode within a tube, the pressure follows [69]

$$\hat{p}_{\mathrm{an}}(x) = \mathrm{Re}[\hat{p}_0 \exp(\mathrm{i}k_x x)], \tag{C.1}$$

where $\hat{p}_0$ and k_x denote the pressure amplitude and the longitudinal wavenumber, respectively. For a tube, the latter can be written in terms of the following dispersion relation that takes viscous losses [69] into account:

$$\frac{k_x^2}{k_0^2} = \frac{A}{A - \frac{1}{2}(1-\mathrm{i})L_{\mathrm{p}}\delta_{\mathrm{v}}}, \tag{C.2}$$

where A and L_{p} are the cross-sectional area and perimeter of the tube, respectively. In addition, k_0 is the unperturbed wavenumber defined as $k_0 = \omega/c_0$. Using Eqs. C.1 and C.2, with $\hat{p}_0$ equals to 1, the analytic pressure distribution is plotted in Fig. C.1 b). At first sight, an excellent match between the analytic and the computed pressure traces is recognized. This is further confirmed by calculating the 2-norm relative error between both discrete curves, $|\hat{p}_{\mathrm{an}} - \hat{p}_{\mathrm{FEM}}|^2/|\hat{p}_{an}|^2$. It yields an error of 0.77 %, ensuring that a correct attenuation is captured by the numerical model.

Second, an eigenvalue (EV) study is carried out in order to assess the damping rates due to the viscous boundary layer. The imaginary part of the eigenfrequency corresponds to the damping rate of that particular mode, i.e. $\omega = \omega_R + \mathrm{i}\alpha$. The zero-mean-flow LEE is again solved numerically via FEM. The same mesh as for the pressure response study is employed. At the walls, Eq. B.14 is applied.

[i]Selection of that particular mode attends to purely illustrative reasons, as similar results are obtained for all modes

At the inlet and outlet, $\hat{u} = 0$ is set in order to be consistent with the boundary conditions implemented in the analytic model used for validation. The value of the computed damping rate for the third longitudinal mode is given in Table C.1. As analytic baseline, the expression for assessing the decay in tubes introduced in [18] is used:

$$\alpha = \frac{1}{R}\sqrt{\frac{\nu\omega}{2}}, \tag{C.3}$$

where R is the radius of the tube. The results are listed in Table C.1. It is observed that the relative error between the analytic and the numerical damping rates remains below 2 %, proving that the derived boundary condition precisely reproduces the analytical damping rates. Overall, as the three-dimensional model is obtained from a mathematical transformation of this model, the observed accuracy can be extrapolated to the extended model.

Table C.1: *Comparison of analytic and numerical damping rates*

	Analytic Eq. (C.3)	Numerical FEM	Abs. Error [%]
Damping rates [rad s^{-1}]	26.16	26.56	1.5

C.2 Validation with an Experimental Test Case

For the validation of the generic boundary condition given by Eq. B.16. The damping rate of the first transverse (T1) mode of the Common Research Chamber (CRC) [94] is computed and compared to measured damping rates.

The CRC is a test rig located at the DLR in Lampoldshausen and dedicated to studying high-frequency combustion instabilities. Geometrically, the test rig consists of a cylindrical combustion chamber with 0.2 m in diameter and 0.04 m in depth, cf. Fig. C.2 a). Before conducting reactive experiments, the combustion chamber was acoustically characterized under cold-flow conditions. Specifically,

the forced response at 1000 Hz, which corresponds to the T1 mode of the chamber (cf. Fig. C.2 b)), was measured and the damping rate was identified from the power spectrum of the signal [94]. As long as there was no mean flow in the chamber, the damping was found to be mainly due to the viscous and thermal diffusion within the boundary layers.

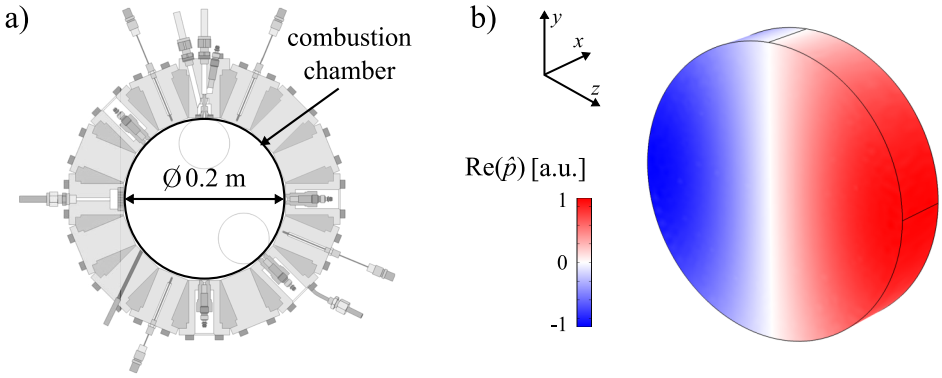

Figure C.2: *a) Cross section of the CRC b) Computed acoustic pressure T1 mode*

To compute the damping rate of the T1 mode of the chamber two eigenvalue (EV) studies are conducted. One study assesses the damping due to the viscous boundary layer, using Eq. B.16. Other study assesses the damping rates due to the thermal boundary layer, using the impedance in Eq. 2.57. As acoustic motions are linear, the total damping rate is obtained by adding both contributions. In each case the zero-mean-flow LEE (Eqs. B.1-B.3 with $\bar{\boldsymbol{u}} = 0$) is solved via FEM. The computational domain is discretized using an unstructured tetrahedral mesh with a resolution of approximately 40 cells per wavelength. Quadratic Lagrange weighting functions are again employed for a total of 101 000 DOF. Constant mean pressure and temperature are prescribed at 101 325 Pa and 288 K, respectively. Consequently, the kinematic viscosity is 1.57×10^{-5} m^2 s^{-1} and the Prandtl number is 0.77. Computed damping rates are listed in the Tab. C.2 along with the recorded CPU times (computed in a workstation with 8 cores at 3.4GHz; 16GB RAM).

The difference between the computed and experimental damping rates can be attributed to the detachment of the acoustic boundary layer at sharp edges, which creates zones of vortex shedding and increases damping. This effect is not in-

Table C.2: *Computed and experimental damping rates of the CRC*

	EV Study: Viscous	EV Study: Thermal	Total	Exp. [94]
CPU time [s]	42	12	54	-
Damping rate [rad s^{-1}]	6	3.8	9.8	13

cluded in the model. Although a slight mismatch is found, the results are in good agreement with the experimental benchmarks. Furthermore, the CPU times measured are in the order of minutes. That allows to efficiently account for the damping due to the boundary layer even in early design stages.

D Weak Form of the Isentropic Linearized Euler Equations with Streamline Upwind Petrov-Galerkin Stabilization

In this appendix, first, FEM is briefly introduced. Second, the weak form of the isentropic LEE, Eqs. 2.47-2.48, is presented. Finally, as LEE are convective-dominated equations, numerical stabilization is required. For that purpose, SUPG stabilization expressions are summarized and exemplified for a two-dimensional case.

Essentially, FEM consists in three steps:

1. To express strong form governing partial differential equations (PDE) in their weak form. This allows relaxing the requirements on the solution, as weak form solutions are fulfilled in an integral way over the domain and not pointwise as in regular PDEs. This also permits finding non-differentiable solutions of the equations as solution smoothness requirements are relaxed.
2. To discretize continuous differential operators using the Galerkin method. The solution is therefore approximated by a linear combination of basis functions multiplied by unknown nodal values. In the current thesis, linear basis functions are employed. After applying the boundary conditions on the corresponding discretized nodes, a system of linear equations for the nodal values is obtained.
3. Matrix assembling and solution. The system of linear equations can be solved as eigenvalue problem in order to retrieve eigenmodes of the system with their corresponding growth rates. The system can be also solved as forced frequency response solution by providing the oscillating frequency and solving for the corresponding fluctuating field. The system can be solved using algebraic methods. In this thesis the method MUMPS is employed [73].

In the following sections, the weak formulation of the isentropic LEE, Eqs. 2.47-2.48, and the required numerical stabilization are introduced.

D.1 Weak Form of Isentropic Linearized Euler Equations

The isentropic LEE, Eqs. 2.47-2.48, are a particular case of the convection-reaction-diffusion equation without diffusion terms. If the primary variables are gathered in a vector $\hat{\boldsymbol{\phi}} = [\hat{p}, \hat{\boldsymbol{u}}]^{\mathrm{T}}$, the residual $R(\hat{\boldsymbol{\phi}})$ of Eqs. 2.47-2.48 can be written as [47]:

$$R(\hat{\boldsymbol{\phi}}) = \mathrm{i}\omega\hat{\boldsymbol{\phi}} + A_i \frac{\partial \hat{\boldsymbol{\phi}}}{\partial x_i} + C\hat{\boldsymbol{\phi}} = 0, \tag{D.1}$$

where A_i and C are the convective and reactive matrices, respectively. In order to numerically implement the governing equations in FEM, the first step is transforming Eq. D.1 into its weak form. This is achieved with the Galerkin method by integrating the residual multiplied by a weighting function over the entire spatial domain:

$$\int_{\Omega} \boldsymbol{w}\, \boldsymbol{I}\, R(\hat{\boldsymbol{\phi}})\, \mathrm{d}\Omega = 0. \tag{D.2}$$

In Eq. D.2, $\boldsymbol{w}$ represents a vector of weight functions associated to each primary variable and $\boldsymbol{I}$ is the identity matrix. The solution of the weak form satisfies the strong equation globally, on an average fashion over the domain, compared to local solution of the strong form. FEM based on Galerkin finite element approximations lacks of numerical stability when diffusive terms of the governing equations are small compared to reactive or convective terms. This issue is addressed in the next section.

D.2 SUPG Stabilization for Isentropic Linearized Euler Equations

In convection-dominated problems, adding artificial numerical diffusion is required to stabilize the solution. The SUPG method is one of the available stabilization techniques [47]. Such a method conveniently introduces artificial diffusion only in streamline direction. It can be formulated as follows:

$$\int_\Omega \boldsymbol{w}\boldsymbol{I}R(\hat{\boldsymbol{\phi}})\,\mathrm{d}\Omega + \int_\Omega \boldsymbol{\tau}R(\hat{\boldsymbol{\phi}})\mathscr{L}(\boldsymbol{w})\,\mathrm{d}\Omega = 0, \tag{D.3}$$

where the second integral in Eq. D.3 comprises the terms of the SUPG stabilization. Specifically, $\boldsymbol{\tau}$ is the stabilization matrix, a diagonal matrix that contains the stabilization parameter of each LEE equation –i.e. $\boldsymbol{\tau} = \delta_{ij}(\tau_i)$. The stabilization parameter is derived from the spectral radius of the convection matrix $r(A_j)$ as follows:

$$\tau_i = \alpha_\tau \max_j \left[\frac{h}{r(A_j)}\right] = \alpha_\tau \max_j \left(\frac{h}{\bar{c} + |\bar{u}_j|}\right). \tag{D.4}$$

On the RHS of Eq. D.4 the spectral radius is written as a function of mean flow quantities. Furthermore, α_τ and h denote the tuning parameter and the characteristic element size, respectively. The operator $\mathscr{L}(\boldsymbol{w})$ for the SUPG method is defined as:

$$\mathscr{L}(\boldsymbol{w}) = A_i \frac{\partial \boldsymbol{w}}{\partial x_i}. \tag{D.5}$$

For example, for a two-dimensional case with a weighting function vector $\boldsymbol{w} = [w_u\, w_v\, w_p]^\mathrm{T}$, the SUPG stabilization of the isentropic LEE, Eqs. 2.47-2.48 is:

$$\begin{aligned}
\mathscr{L}(\boldsymbol{w}) &= \begin{bmatrix} \bar{u} & 0 & 1 \\ 0 & \bar{u} & 0 \\ \gamma\bar{p} & 0 & \bar{u} \end{bmatrix} \begin{bmatrix} \frac{\partial w_u}{\partial x} \\ \frac{\partial w_v}{\partial x} \\ \frac{\partial w_p}{\partial x} \end{bmatrix} + \begin{bmatrix} \bar{v} & 0 & 0 \\ 0 & \bar{v} & 1 \\ 0 & \gamma\bar{p} & \bar{v} \end{bmatrix} \begin{bmatrix} \frac{\partial w_u}{\partial y} \\ \frac{\partial w_v}{\partial y} \\ \frac{\partial w_p}{\partial y} \end{bmatrix} = \\
&= \begin{bmatrix} \bar{u}\frac{\partial w_u}{\partial x} + \bar{v}\frac{\partial w_u}{\partial y} + \frac{\partial w_p}{\partial x} \\ \bar{u}\frac{\partial w_v}{\partial x} + \bar{v}\frac{\partial w_v}{\partial y} + \frac{\partial w_p}{\partial y} \\ \gamma\bar{p}\left(\frac{\partial w_u}{\partial x} + \frac{\partial w_v}{\partial y}\right) + \bar{u}\frac{\partial w_p}{\partial x} + \bar{v}\frac{\partial w_p}{\partial y} \end{bmatrix}
\end{aligned} \tag{D.6}$$

E Experimental Operating Points of the HTRC

	Exp. No.	$\dot{m}_{air}$ [g s^{-1}]	$Y_{st,air}$ [–]	λ_{EV} [–]	λ_{SEV} [–]	Y_{f,C_3H_8} [–]	P_{EV} [kW]	$\dot{m}_{sh,air}$ [g s^{-1}]	$\dot{m}_{f,SEV}$ [g s^{-1}]	P_{SEV} [kW]
Series 1	Case 1	OP-01	300	0.85	2.10	1.25	0.15	417	21.6	11.1	543
	Case 2	OP-03	340	0.85	2.10	1.25	0.15	473	24.5	12.5	612
	Case 3	OP-05	380	0.85	2.10	1.25	0.15	529	27.4	14.0	685
	Case 4	OP-07	420	0.85	2.10	1.25	0.15	584	30.3	15.5	759
Series 2	Case 1	OP-05	380	0.85	2.10	1.25	0.15	529	27.4	14.0	685
	Case 2	OP-09	380	0.85	2.05	1.25	0.15	542	27.8	13.8	675
	Case 3	OP-11	380	0.85	2.00	1.25	0.15	555	28.1	13.6	666
	Case 4	OP-13	380	0.85	1.95	1.25	0.15	569	28.4	13.4	656
Series 3	Case 1	OP-15	380	0.85	2.10	1.25	0.00	529	27.4	14.0	685
	Case 2	OP-17	380	0.85	2.10	1.25	0.05	529	27.4	14.0	685
	Case 3	OP-19	380	0.85	2.10	1.25	0.10	529	27.4	14.0	685
	Case 4	OP-05	380	0.85	2.10	1.25	0.15	529	27.4	14.0	685
Series 4	Case 1	OP-21	380	0.85	2.10	1.55	0.15	529	28.9	11.4	558
	Case 2	OP-23	380	0.85	2.10	1.40	0.15	529	28.3	12.6	617
	Case 3	OP-05	380	0.85	2.10	1.25	0.15	529	27.4	14.0	685
	Case 4	OP-25	380	0.85	2.10	1.10	0.15	529	26.1	15.9	778

Table E.1: *($\dot{m}_{air}$) Air ass flow 1st stage; ($Y_{st,air}$) staging air ratio 1st stage; (λ_{EV}) air-fuel eq. ratio 1st stage; (λ_{SEV}) air-fuel eq. ratio reheat stage; (Y_{f,C_3H_8}) mass fraction of propane in reheat stage fuel; (P_{EV}) thermal power 1st stage; ($\dot{m}_{sh,air}$) mass flow shielding air; ($\dot{m}_{f,SEV}$) mass flow fuel reheat stage; (P_{SEV}) thermal power reheat stage.*

F Mesh Independence Study of Reactive CFD Simulations

F.1 Mesh Independence Ternary Mixing

In order to prove mesh independence of the ternary mixing CFD setup (cf.Section 4.2.2) three different meshes are employed, cf. Tab. F.1. Results for velocity and fuel mass fraction are compared for each mesh size in Figs. F.1 and F.2. The similarity of the velocity fields obtained with the three different mesh setups shows that the results are mesh independent.

Table F.1: *Summary of mesh properties for the ternary mixing setup.*

Mesh	Size	Size refinement	No. layers prismatic mesh	Height 1stelement prismatic mesh	Growth rate prismatic mesh	No. elements
Coarse	5 mm	3 mm	30	0.05 mm	1.10	1.4×10^6
Medium	4 mm	2.5 mm	30	0.05 mm	1.10	2.3×10^6
Fine	4 mm	2 mm	30	0.05 mm	1.10	3.5×10^6

F.2 Mesh Independence Premixed Combustion

In order to prove mesh independence of the premixed CFD setup (cf. Section 4.3) three different meshes are employed, cf. Tab. F.2. Results for volumetric heat release and turbulent kinetic energy are compared for each mesh size in Figs. F.1 and F.2. The similarity of the velocity fields obtained with the three different mesh setups shows that the results are mesh independent.

Table F.2: *Summary of mesh properties for the premixed combustion setup.*

Mesh	Size	Size refinement	No. layers prismatic mesh	Height 1stelement prismatic mesh	Growth rate prismatic mesh	No. elements
Coarse	5 mm	3 mm	30	0.05 mm	1.10	0.7×10^6
Medium	4 mm	2.5 mm	30	0.05 mm	1.10	1.1×10^6
Fine	3.5 mm	2 mm	30	0.05 mm	1.10	1.7×10^6

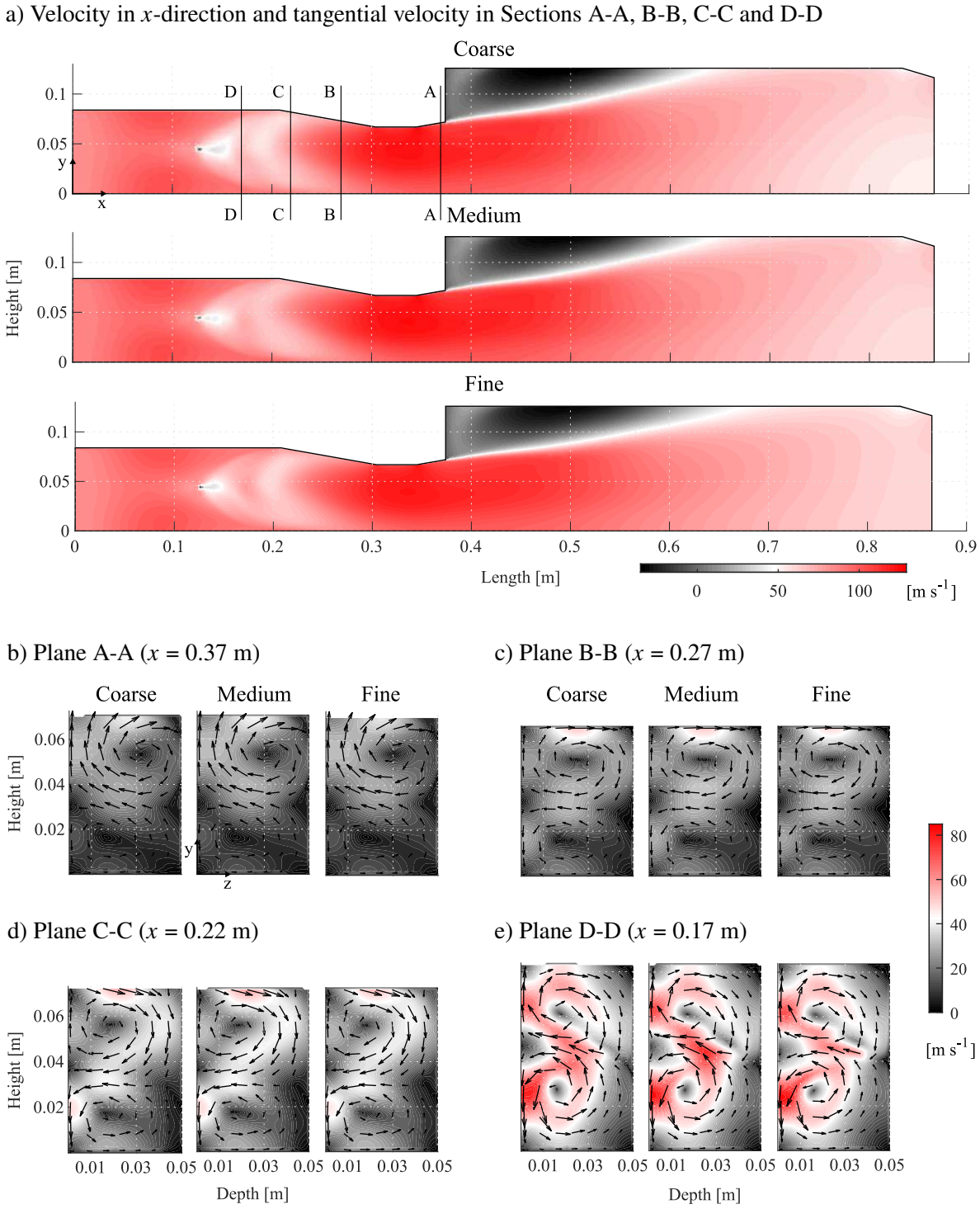

Figure F.1: *Mesh dependence of velocity fields in the ternary mixing stage: a) Velocity in x-direction in symmetry plane b)-e) Tangential velocity in corresponding plane sections*

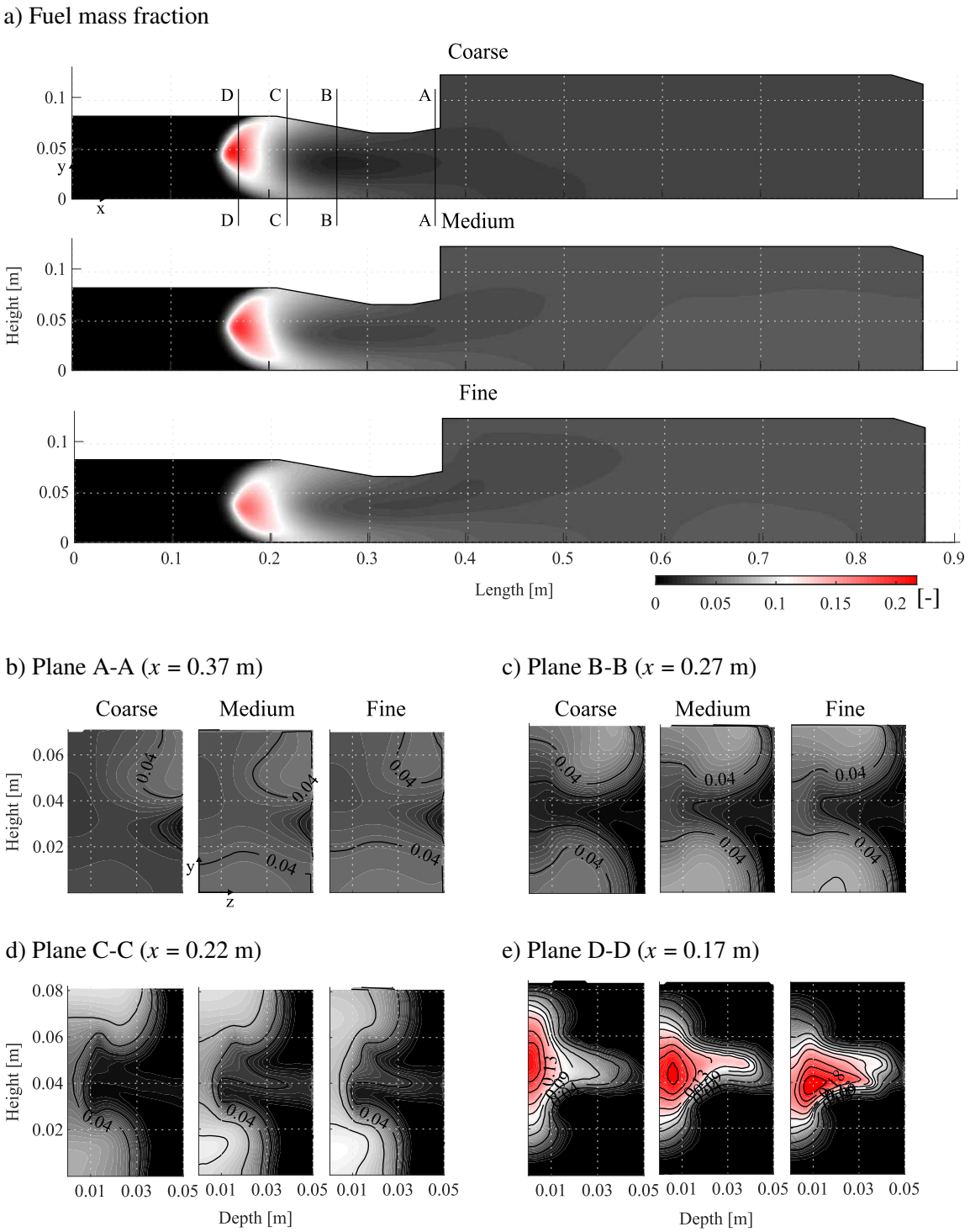

Figure F.2: *Mesh dependence of fuel mass fraction in the ternary mixing stage: a) Fuel mass fraction in symmetry plane b)-e) Fuel mass fraction in corresponding plane sections*

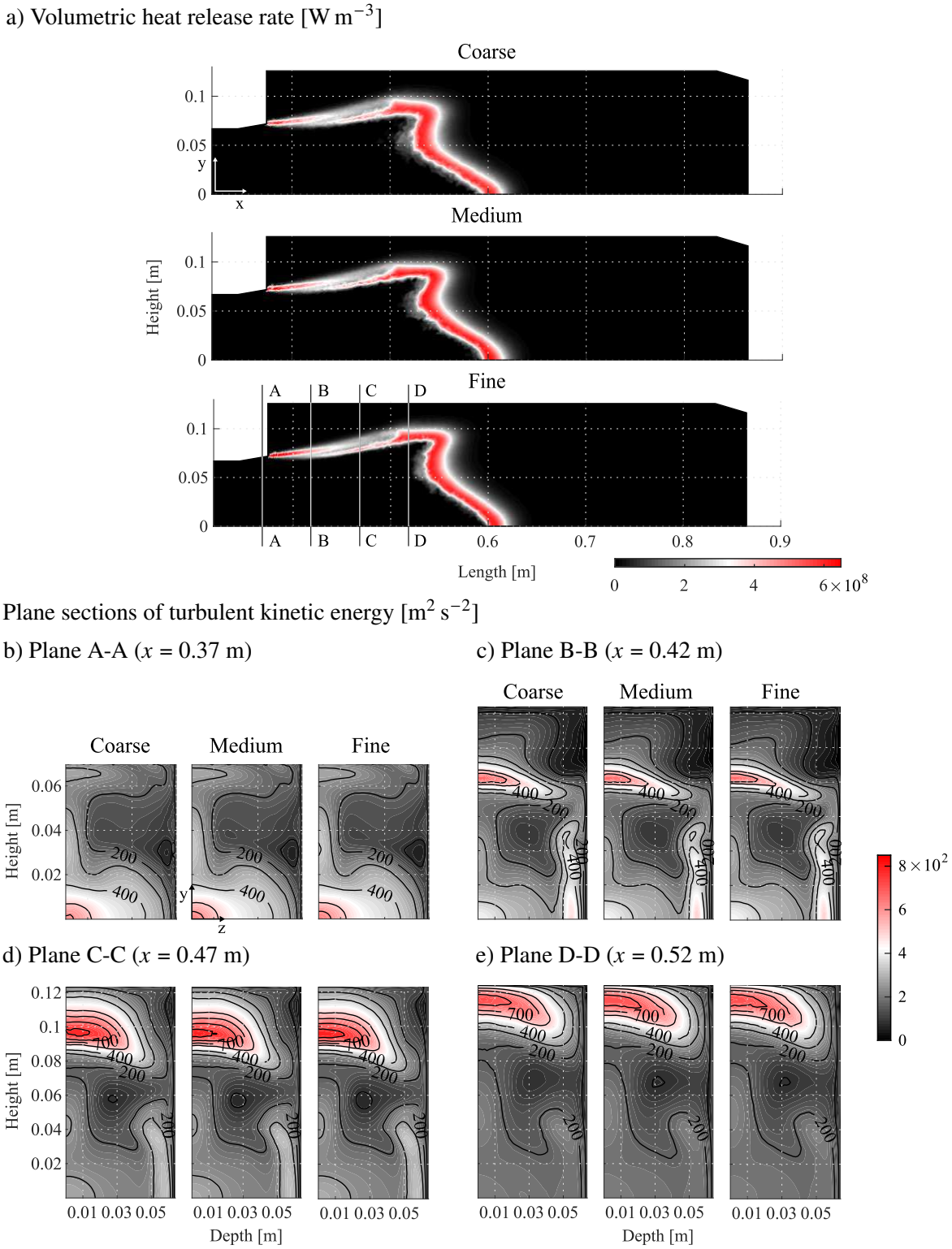

Figure F.3: *Mesh dependence in the premixed stage: a) Volumetric heat release rate b)-e) Turbulent kinetic energy in corresponding plane sections.*

G Mesh Independence Study of Thermoacoustic Simulations

Damping and growth rates depend on the mesh size and the stabilization parameter [48]. Therefore, in this appendix, mesh size and stabilization parameter independence studies for the operating point OP-01 are shown. Similar behavior is expected for the rest of the studied operating points, and hence those studies are omitted. A configuration without oscillating heat release is employed for the studies, so that the imaginary part of the obtained eigenfrequencies introduces damping only.

First, the base mesh size is investigated. For constant corner refinement size (500 times finer than base mesh size) and $\alpha_\tau = 360$, the damping rates for increasingly finer mesh sizes are plotted in Fig. G.1. There, it can be seen that damping rates converge to a nearly constant value for mesh sizes smaller than 1.5 mm (about 4×10^5 DOFs). Therefore, that value is selected as base mesh size.

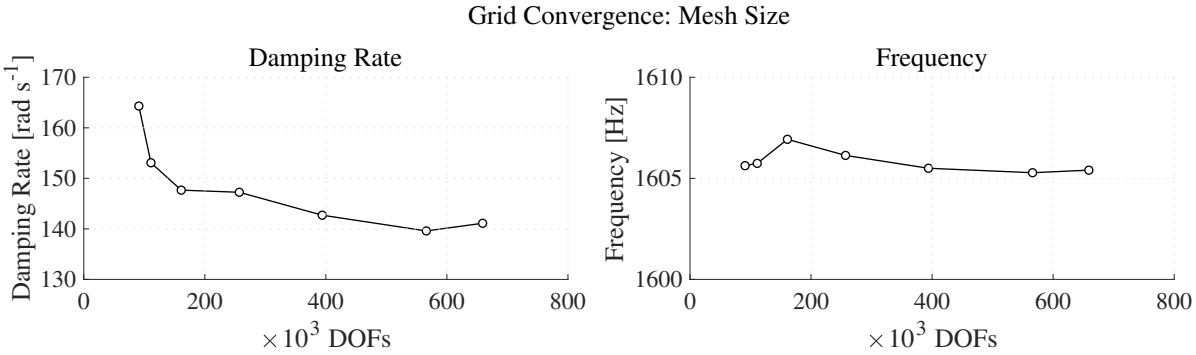

Figure G.1: *Evolution of damping for rates (OP-01) for different mesh sizes (from left to right 8, 5, 3, 2, 1.5, 1.2 and 1.1 mm). The corner refinement is 500 finer than the base mesh size.*

Second, the corner mesh size is studied. It is crucial to sufficiently resolve the corner area in order to capture the energy transformation processes between acoustic and vortical modes that determine the damping rate (cf. [66]). To do so, the base size is refined a number of times. In Fig. G.2, damping rates for increasingly finer corner mesh size are depicted. It can be observed that corner refinement is needed as damping rate values without mesh refinement (cf. leftmost

point in Fig. G.2) deviate about 40% from the converged value. Furthermore, a minimum corner refinement size is determined. For the studied configuration it is sufficient to use a mesh 500 times finer than the base mesh size.

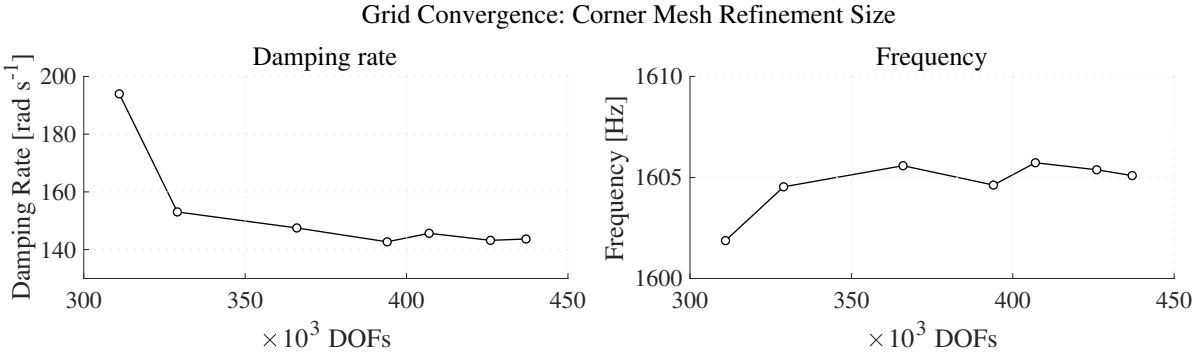

Figure G.2: *Evolution of damping for rates (OP-01) for different mesh corner refinement sizes (Base mesh size is 1.5 mm, corner refinement is 1, 10, 100, 500, 1000, 3000 and 6000 times finer than the base mesh size).*

Finally, the influence of the SUPG stabilization parameter on the damping rates is analyzed. A parameter sweep study for α_τ, with α_τ ranging between 1 and 2060, is carried out. Results for two base mesh sizes (3 mm and 1.5 mm) are compared with each other in Fig. G.3. The coarser mesh size configuration (left plots in Fig. G.3) does not show convergence for increasing α_τ regardless of the corner refinement size selected. Better convergence is found for the finer mesh configuration (right plots in Fig. G.3). In particular, damping rates converge for sufficient corner refinement within a window of α_τ from 360 to 600. This is further demonstrated by calculating the relative change of damping rates for consecutive values of α_τ. This is denoted as relative error and defined as:

$$\text{Rel.err.}[\%] = 100 \times \frac{|\text{DR}_{\alpha_\tau(i)} - \text{DR}_{\alpha_\tau(i-1)}|}{\text{DR}_{\alpha_\tau(i-1)}} \tag{G.1}$$

Relative error for increasing α_τ is plotted in Fig. G.4. For the damping rates it can be seen that damping rates change under 1 % between 250 and 1000. For frequencies, the relative error is below 0.1 % for the entire studied α_τ-range.

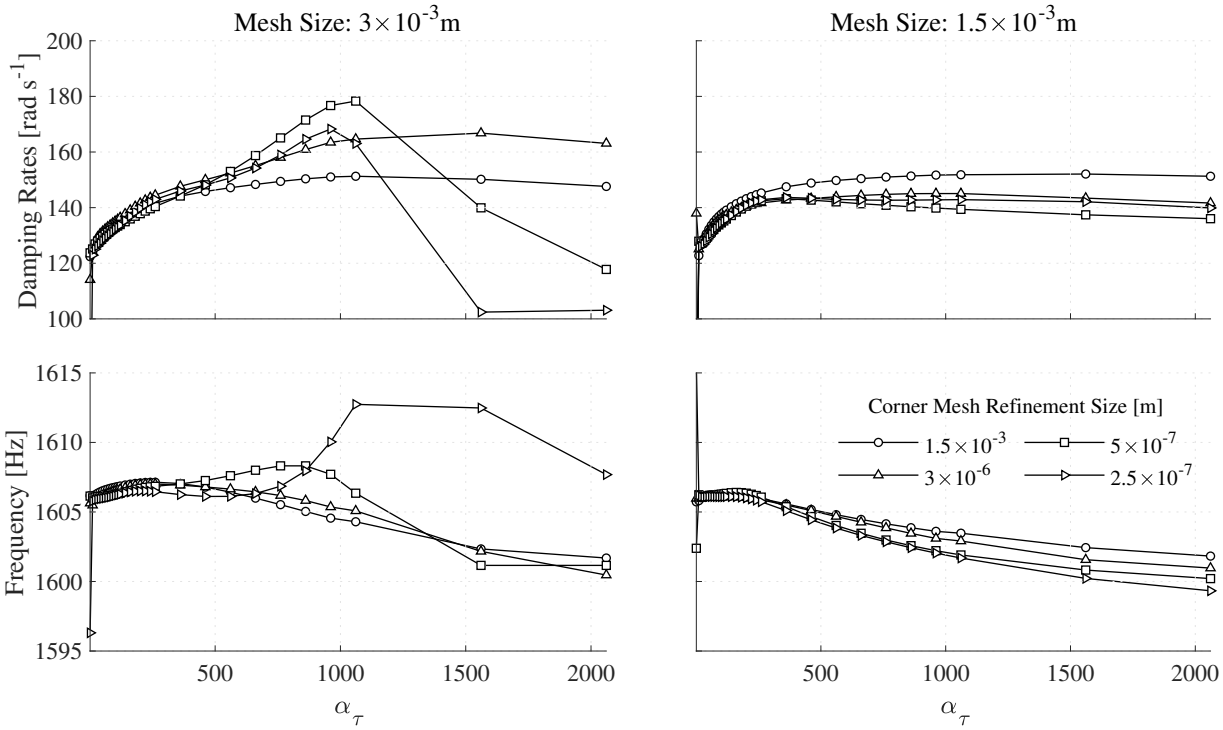

Figure G.3: *Damping rates (top row) and frequency (bottom row) dependence on stabilization parameter for different corner refinement sizes.*

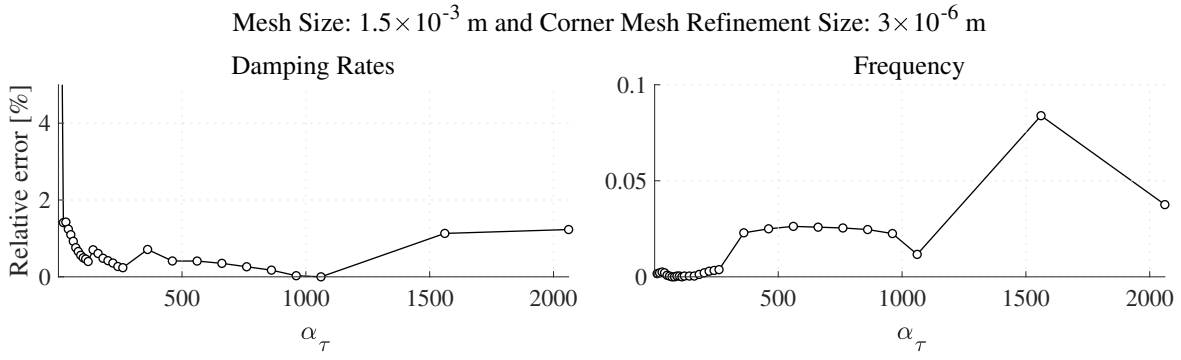

Figure G.4: *Relative error of damping rates and frequency of consecutive α_τ values for the selected mesh size and corner refinement.*

H Estimation of Experimental Damping Rates: Lorentzian Fitting of Power Spectral Density

H.1 Lorentzian Fitting of Power Spectral Density

Damping rates of time-dependent pressure signals can be estimated by applying a Lorentzian fitting on the power spectral density (PSD) of the corresponding pressure traces. Note that this method is only applicable to linearly stable systems with moderate forcing so the system remains in the linear regime [95]. Theoretically, this is supported by the fact that small linear pressure fluctuations in a thermoacoustic system can be modeled as a damped harmonic oscillator [95]. The PSD of the response to stochastic driving from turbulent combustion is proportional to a Lorentzian distribution:

$$\mathrm{PSD}(\omega) \propto \frac{p_0^2}{(\omega - \omega_0)^2 + \alpha^2} \tag{H.1}$$

where p_0 is the amplitude of the pressure signal, ω_0 is the resonance frequency of the corresponding mode and α is the associated damping rate [96]. Therefore, in order to estimate the damping rate of a given operating point. First, the PSD is obtained from recorded temporal pressure traces. Subsequently, a Lorentzian fitting is applied to the PSD from which parameters ω_0 and α are retrieved.

H.2 Results of Experimental Damping Rates

For illustrative purposes, the PSD distribution of the OP-01 (cf. Tab. E.1 in Appendix E) is represented in Fig. H.1. This PSD is estimated from 4.5 s long pressure traces using the so-called Welch's method [97], which is readily available as the `pwelch` function in the Signal Processing toolbox of MATLAB [98]. This method splits up the original signal into a series of overlapping signal segments. Afterwards, a windowed periodogram of each segment is computed. Finally, all periodograms are averaged to obtain the PSD. All in all, the averaging process

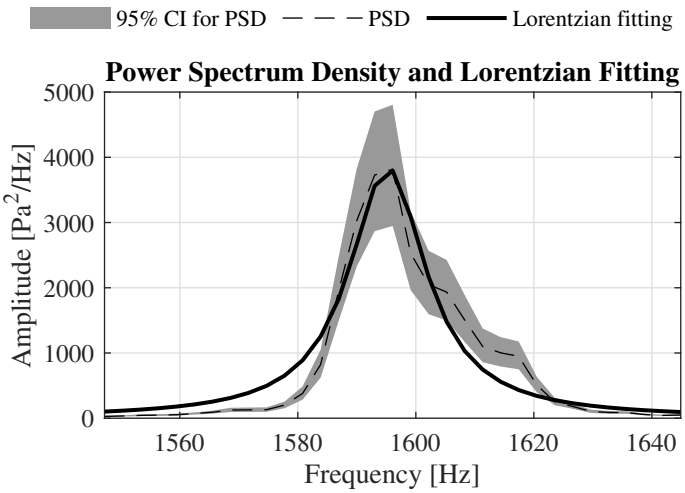

Figure H.1: *Power spectrum density (PSD) of the pressure trace of OP-01 with confidence interval (CI) of 95% and corresponding Lorentzian fitting.*

allows to reduce noise in the PSD at the cost of reducing the frequency resolution [97].

Table H.1: *Damping rates in for each experimental operating point (cf. Appendix E).*

	Exp. No.	Damping rate [rad s^{-1}]		Exp. No.	Damping rate [rad s^{-1}]
Series 1	OP-01	50 ± 3	Series 3	OP-15	64 ± 3
	OP-03	59 ± 3		OP-17	65 ± 3
	OP-05	69 ± 3		OP-19	67 ± 3
	OP-07	56 ± 3		OP-05	69 ± 3
Series 2	OP-05	69 ± 3	Series 4	OP-21	51 ± 3
	OP-09	43 ± 3		OP-23	70 ± 3
	OP-11	46 ± 3		OP-05	69 ± 3
	OP-13	64 ± 3		OP-25	61 ± 3

The available pressure traces are divided into 20 segments (window length of 0.225 s) and then Hamming windowing is applied. This smooths the PSD out, while a frequency resolution of about 3 Hz is ensured. Finally, fitting to a Lorentzian curve is applied to the PSD. Note that the PSD is bandpassed around the first transverse mode frequency so the corresponding PSD peak is centered with respect to the frequency window of the bandpass filter. The previously

described process is applied to all available operating points, cf. Tab. E.1 in Appendix E. The resulting experimental damping rates are gathered in Table H.1.

Bibliography

[1] *World Energy Outlook 2018*. OECD, 2018. DOI: 10.1787/weo-2018-en.

[2] K. Juhrich. *CO2 Emission Factors for Fossil Fuels*. German Environment Agency, editor. German Environment Agency (Umweltbundesamt), 2016. URL: www.umweltbundesamt.de/en/publikationen/co2-emission-factors-for-fossil-fuels.

[3] C. F. A. Rodrigues, M. A. P. Dinis, and M. J. Lemos de Sousa. Review of European energy policies regarding the recent "carbon capture, utilization and storage" technologies scenario and the role of coal seams. *Environmental Earth Sciences*, 74(3):2553–2561, 2015. DOI: 10.1007/s12665-015-4275-0.

[4] M. A. Gonzalez-Salazar, T. Kirsten, and L. Prchlik. Review of the operational flexibility and emissions of gas- and coal-fired power plants in a future with growing renewables. *Renewable and Sustainable Energy Reviews*, 82:1497–1513, 2018. URL: www.sciencedirect.com/science/article/pii/S1364032117309206.

[5] A. Lefebvre. *Gas Turbine Combustion: Alternative Fuels and Emissions, Third Edition*. CRC Press, 2010. DOI: 10.1201/9781420086058.

[6] F. Güthe, J. Hellat, and P. Flohr. The Reheat Concept: The Proven Pathway to Ultralow Emissions and High Efficiency and Flexibility. *Journal of Engineering for Gas Turbines and Power*, 131(2), 2008. DOI: 10.1115/1.2836613.

[7] K. M. Düsing, A. Ciani, U. Benz, A. Eroglu, and K. Knapp. Development of GT24 and GT26 (Upgrades 2011) Reheat Combustors, Achieving Reduced Emissions and Increased Fuel Flexibility. In *Proceedings of the ASME Turbo Expo 2013*, 2013. DOI: 10.1115/GT2013-95437.

[8] F. Joos, P. Brunner, M. Stalder, and S. Tschirren. Field Experience of the Sequential Combustion System for the GT24/GT26 Gas Turbine Family. In *Proceedings of the ASME International Gas Turbine and Aeroengine Congress and Exhibition 1998*, 1998. DOI: 10.1115/98-GT-220.

[9] F. Joos, P. Brunner, B. Schulte-Werning, K. Syed, and A. Eroglu. Development of the Sequential Combustion System for the ABB GT24/GT26 Gas Turbine Family. In *Proceedings of the ASME International Gas Turbine and Aeroengine Congress and Exhibition 1996*, 1996. DOI: 10.1115/96-GT-315.

[10] T. Sattelmayer, M. P. Felchlin, J. Haumann, J. Hellat, and D. Styner. Second-Generation Low-Emission Combustors for ABB Gas Turbines: Burner Development and Tests at Atmospheric Pressure. *Journal of Engineering for Gas Turbines and Power*, 114(1):118, 1992. DOI: 10.1115/1.2906293.

[11] C. Steinbach, T. Ruck, J. Lloyd, P. Jansohn, K. Döbbeling, T. Sattelmayer, and T. Strand. ABB's Advanced EV Burner — A Dual Fuel Dry Low NOx Burner for Stationary Gas Turbines. In *Proceedings of the ASME International Gas Turbine and Aeroengine Congress and Exhibition 1998*, 1998. DOI: 10.1115/98-GT-519.

[12] D. A. Pennell, M. R. Bothien, A. Ciani, V. Granet, G. Singla, S. Thorpe, A. Wickstroem, K. Oumejjoud, and M. Yaquinto. An Introduction to the Ansaldo GT36 Constant Pressure Sequential Combustor. In *Proceedings of the ASME Turbo Expo 2017*, 2017. DOI: 10.1115/GT2017-64790.

[13] M. R. Bothien, A. Ciani, J. P. Wood, and G. Fruechtel. Toward Decarbonized Power Generation With Gas Turbines by Using Sequential Combustion for Burning Hydrogen. *Journal of Engineering for Gas Turbines and Power*, 141(12), 2019. DOI: 10.1115/1.4045256.

[14] J. O'Connor, V. Acharya, and T. Lieuwen. Transverse combustion instabilities: Acoustic, fluid mechanic, and flame processes. *Progress in Energy and Combustion Science*, 49:1–39, 2015. URL: www.sciencedirect.com/science/article/abs/pii/S0360128515000027.

[15] T. Hummel, F. M. Berger, M. Hertweck, B. Schuermans, and T. Sattelmayer. High-Frequency Thermoacoustic Modulation Mechanisms in Swirl-Stabilized Gas Turbine Combustors Part Two: Modeling and Analysis. *Journal of Engineering for Gas Turbines and Power*, 139(7), 2017. DOI: 10.1115/1.4035592.

[16] F. M. Berger, T. Hummel, M. Hertweck, J. Kaufmann, B. Schuermans, and T. Sattelmayer. High-Frequency Thermoacoustic Modulation Mechanisms in Swirl-Stabilized Gas Turbine Combustors—Part I: Experimental Investigation of Local Flame Response. *J. Eng. Gas Turbines Power*, 139(7), 2017. DOI: 10.1115/1.4035591.

[17] T. C. Lieuwen. *Unsteady Combustor Physics*. Cambridge University Press, Cambridge, 2012. DOI: 10.1017/CBO9781139059961.

[18] F. Culick. *Unsteady Motions in Combustion Chambers for Propulsion Systems*, volume TR-IST-028 of *RTO technical report*. N.A.T.O, Neuilly-sur-Seine Cedex, 2008. DOI: 10.14339/RTO-AG-AVT-039.

[19] A. Ni, W. Polifke, and F. Joos. Ignition Delay Time Modulation as a Contribution to Thermo-Acoustic Instability in Sequential Combustion. In *Proceedings of the ASME Turbo Expo 2000*, May 2000. DOI: 10.1115/2000-GT-0103.

[20] Y. Yang, N. Noiray, A. Scarpato, O. Schulz, K. M. Düsing, and M. Bothien. Numerical Analysis of the Dynamic Flame Response in Alstom Reheat Combustion Systems. In *Proceedings of the ASME Turbo Expo 2015*, 2015. DOI: 10.1115/GT2015-42622.

[21] A. Scarpato, L. Zander, R. Kulkarni, and B. Schuermans. Identification of Multi-Parameter Flame Transfer Function for a Reheat Combustor. In *Proceedings of the ASME Turbo Expo 2016*, 2016. DOI: 10.1115/GT2016-57699.

[22] M. Weilenmann, Y. Xiong, M. Bothien, and N. Noiray. Background-Oriented Schlieren of Fuel Jet Flapping Under Thermoacoustic Oscillations in a Sequential Combustor. *Journal of Engineering for Gas Turbines and Power*, 141(1), 2019. DOI: 10.1115/1.4041240.

[23] O. Schulz and N. Noiray. Autoignition flame dynamics in sequential combustors. *Combustion and Flame*, 192:86–100, 2018. URL: www.sciencedirect.com/science/article/abs/pii/S0010218018300609.

[24] O. Schulz, U. Doll, D. Ebi, J. Droujko, C. Bourquard, and N. Noiray. Thermoacoustic instability in a sequential combustor: Large eddy simulation and experiments. *Proceedings of the Combustion Institute*, 37(4):5325–5332, 2019. URL: www.sciencedirect.com/science/article/abs/pii/S1540748918305078.

[25] O. Schulz and N. Noiray. Combustion regimes in sequential combustors: Flame propagation and autoignition at elevated temperature and pressure. *Combustion and Flame*, 205:253–268, 2019. URL: www.sciencedirect.com/science/article/abs/pii/S0010218019301087.

[26] G. Singla, N. Noiray, and B. Schuermans. Combustion Dynamics Validation of an Annular Reheat Combustor. In *Proceedings of the ASME Turbo Expo 2012*, 2012. DOI: 10.1115/GT2012-68684.

[27] B. Schuermans, M. Bothien, M. Maurer, and B. Bunkute. Combined Acoustic Damping-Cooling System for Operational Flexibility of GT26/GT24 Reheat Combustors. In *Proceedings of the ASME Turbo Expo 2015*, 2015. DOI: 10.1115/GT2015-42287.

[28] M. P. G. Zellhuber. *High Frequency Response of Auto-Ignition and Heat Release to Acoustic Perturbations*. Ph.D. Thesis, Technische Universität München, Munich, 2013. URL: www.epc.ed.tum.de/fileadmin/w00cgc/tfd/Forschung/Dissertationen/Zellhuber_2013_High_Frequency_Response_of_Auto-Ignition_and_Heat_Release_to_Acoustic.pdf.

[29] J. Schwing and T. Sattelmayer. High-Frequency Instabilities in Cylindrical Flame Tubes: Feedback Mechanism and Damping. In *Proceedings of the ASME Turbo Expo 2013*, 2013. DOI: 10.1115/GT2013-94064.

[30] F. M. Berger, T. Hummel, P. Romero, B. Schuermans, and T. Sattelmayer. A Novel Reheat Combustor Experiment for the Analysis of High-Frequency Flame Dynamics: Concept and Experimental Validation. In *Proceedings of the ASME Turbo Expo 2018*, 2018. DOI: 10.1115/GT2018-77101.

[31] F. M. Berger. *High Frequency Transverse Thermoacoustic Instabilities in Swirl and Reheat Combustors*. Ph.D. Thesis, Technische Universität München, Munich, 2020. URL: www.epc.ed.tum.de/fileadmin/w00cgc/td/Forschung/Dissertationen/Berger_Frederik.pdf.

[32] J. Schwing, F. Grimm, and T. Sattelmayer. A Model for the Thermo-Acoustic Feedback of Transverse Acoustic Modes and Periodic Oscillations in Flame Position in Cylindrical Flame Tubes. In *Proceedings of the ASME Turbo Expo 2012*, 2013. DOI: 10.1115/GT2012-68775.

[33] T. Hofmeister, T. Hummel, B. Schuermans, and T. Sattelmayer. Quantification of Energy Transformation Processes Between Acoustic and Hydrodynamic Modes in Non-Compact Thermoacoustic Systems via a Helmholtz-Hodge Decomposition Approach. In *Proceedings of the ASME Turbo Expo 2019*, 2019. DOI: 10.1115/GT2019-90240.

[34] N. Klarmann, T. Sattelmayer, W. Geng, and F. Magni. Flamelet Generated Manifolds for Partially Premixed, Highly Stretched and Non-Adiabatic Combustion in Gas Turbines. In *54th AIAA Aerospace Sciences Meeting*. American Institute of Aeronautics and Astronautics. DOI: 10.2514/6.2016-2120.

[35] J. McClure, F. M. Berger, M. Bertsch, B. Schuermans, and T. Sattelmayer. Self-Excited High-Frequency Transverse Limit-Cycle Oscillations and Associated Flame Dynamics in a Gas Turbine Reheat Combustor Experiment. In *Proceedings of the ASME Turbo Expo 2021*, 2021. DOI: 10.1115/GT2021-59540.

[36] T. Poinsot. Prediction and control of combustion instabilities in real engines. *Proceedings of the Combustion Institute*, 36(1):1–28, 2017. URL: www.sciencedirect.com/science/article/abs/pii/S1540748916300074.

[37] A. Ghani, T. Poinsot, L. Gicquel, and G. Staffelbach. LES of longitudinal and transverse self-excited combustion instabilities in a bluff-body stabilized turbulent premixed flame. *Combustion and Flame*, 162(11):4075–4083, 2015. DOI: 10.1016/j.combustflame.2015.08.024. URL: www.sciencedirect.com/science/article/pii/S0010218015002989.

[38] T. Hofmeister and T. Sattelmayer. Amplitude-Dependent Damping and Driving Rates of High-Frequency Oscillations in a Lab-Scale Lean-Premixed Gas Turbine Combustor. In *Proceedings of the ASME Turbo Expo 2021*, 2021. DOI: 10.1115/GT2021-58456.

[39] A. Kierkegaard, S. Boij, and G. Efraimsson. A frequency domain linearized Navier–Stokes equations approach to acoustic propagation in flow ducts with sharp edges. *The Journal of the Acoustical Society of America*, 127(2):710–719, Feb. 2010. DOI: 10.1121/1.3273899.

[40] J. Gikadi. *Prediction of Acoustic Modes in Combustors using Linearized Navier-Stokes Equations in Frequency Space*. Ph.D. Thesis, Technische Universität München, Munich, 2014. URL: www.epc.ed.tum.de/fileadmin/w00cgc/td/Forschung/Dissertationen/Gikadi2014.pdf.

[41] B.-T. Chu and L. S. G. Kovásznay. Non-linear interactions in a viscous heat-conducting compressible gas. *Journal of Fluid Mechanics*, 3(5):494–514, 1958. DOI: 10.1017/S0022112058000148.

[42] M. Schulze. *Linear Stability Assessment of Cryogenic Rocket Engines*. Ph.D. Thesis, Technische Universität München, Munich, 2016. URL: www.epc.ed.tum.de/fileadmin/w00cgc/td/Forschung/Dissertationen/schulze16.pdf.

[43] R. Ewert and W. Schröder. Acoustic perturbation equations based on flow decomposition via source filtering. *Journal of Computational Physics*, 188(2):365–398, 2003. URL: dl.acm.org/doi/10.1016/S0021-9991(03)00168-2.

[44] B. Schuermans. *Modeling and Control of Thermoacoustic Instabilities*. Ph.D. Thesis, École Polytechnique Fédérale de Lausanne, Lausanne, 2003. URL: https://infoscience.epfl.ch/record/33275.

[45] T. Emmert, S. Jaensch, C. Sovardi, and W. Polifke. taX - a Flexible Tool for Low-Order Duct Acoustic Simulation in Time and Frequency Domain. In *7th Forum Acusticum*, Krakow, Poland, 2014.

[46] S. R. Stow and A. P. Dowling. Thermoacoustic Oscillations in an Annular Combustor. In *Proceedings of the ASME Turbo Expo 2001*, 2001. DOI: 10.1115/2001-GT-0037.

[47] J. Donéa and A. Huerta. *Finite element methods for flow problems*. Wiley, Chichester ; Hoboken, NJ, 2003. DOI: 10.1002/0470013826.

[48] T. Hofmeister, T. Hummel, F. Berger, N. Klarmann, and T. Sattelmayer. Elimination of Numerical Damping in the Stability Analysis of Noncompact Thermoacoustic Systems With Linearized Euler Equations. *Journal of Engineering for Gas Turbines and Power*, 143(3), 2021. DOI: 10.1115/1.4049651.

[49] M. Meindl, M. Merk, F. Fritz, and W. Polifke. Determination of Acoustic Scattering Matrices from Linearized Compressible Flow Equations with Application to Thermoacoustic Stability Analysis. *J. Theor. Comp. Acout.*, 27(03), 2019. DOI: 10.1142/S2591728518500275.

[50] T. Poinsot and D. Veynante. *Theoretical and numerical combustion*. Edwards, Philadelphia, 2nd ed edition, 2005.

[51] R. Kulkarni, B. Bunkute, F. Biagioli, M. Duesing, and W. Polifke. Large Eddy Simulation of ALSTOM's Reheat Combustor Using Tabulated Chemistry and Stochastic Fields-Combustion Model. In *Proceedings of the ASME Turbo Expo 2014*, 2014. DOI: 10.1115/GT2014-26053.

[52] K. Aditya, A. Gruber, C. Xu, T. Lu, A. Krisman, M. R. Bothien, and J. H. Chen. Direct numerical simulation of flame stabilization assisted by autoignition in a reheat gas turbine combustor. *Proceedings of the Combustion Institute*, 37(2):2635–2642, 2019. DOI: 10.1016/j.proci.2018.06.084.

[53] ANSYS. Fluent 19 Theory Guide.

[54] K. N. C. Bray, M. Champion, and P. A. Libby. The Interaction Between Turbulence and Chemistry in Premixed Turbulent Flames. In R. Borghi and S. N. B. Murthy, editors, *Turbulent Reactive Flows*, Lecture Notes in Engineering, pages 541–563, 1989. DOI: 10.1007/978-1-4613-9631-4_26.

[55] D. Veynante and L. Vervisch. Turbulent combustion modeling. *Progress in Energy and Combustion Science*, 28(3):193–266, 2002. URL: www.sciencedirect.com/science/article/pii/S036012850100017X.

[56] K. N. C. Bray. Studies of the turbulent burning velocity. *Proceedings of the Royal Society of London. Series A: Mathematical and Physical Sciences*, 431(1882):315–335, 1990. DOI: 10.1098/rspa.1990.0133.

[57] J. Haßlberger. *Numerical Simulation of Deflagration-to-Detonation Transition on Industry Scale*. Ph.D. Thesis, Technische Universität München, Munich, 2017. URL: www.epc.ed.tum.de/fileadmin/w00cgc/td/Forschung/Dissertationen/hasslberger2017.pdf.

[58] L. J. Spadaccini and M. B. Colket. Ignition delay characteristics of methane fuels. *Progress in Energy and Combustion Science*, 20(5):431–460, 1994. URL: www.sciencedirect.com/science/article/pii/0360128594900116.

[59] D. G. Crighton, A. P. Dowling, J. E. F. Williams, M. Heckl, and F. G. Leppington. Thermoacoustic Sources and Instabilities. In D. G. Crighton, A. P. Dowling, J. E. F. Williams, M. Heckl, and F. G. Leppington, editors, *Modern Methods in Analytical Acoustics: Lecture Notes*, pages 378–405. Springer, London, 1992. DOI: 10.1007/978-1-4471-0399-8_13.

[60] A. P. Dowling. The calculation of thermoacoustic oscillations. *Journal of Sound and Vibration*, 180(4):557–581, 1995. URL: www.sciencedirect.com/science/article/pii/S0022460X85701009.

[61] Y. Xia, I. Duran, A. S. Morgans, and X. Han. Dispersion of Entropy Perturbations Transporting through an Industrial Gas Turbine Combustor. *Flow, Turbulence and Combustion*, 100(2):481–502, 2018. DOI: 10.1007/s10494-017-9854-6.

[62] M. Weilenmann, Y. Xiong, and N. Noiray. On the dispersion of entropy waves in turbulent flows. en. *J. Fluid Mech.*, 903:R1, 2020. DOI: 10.1017/jfm.2020.703.

[63] T. Sattelmayer. Influence of the Combustor Aerodynamics on Combustion Instabilities From Equivalence Ratio Fluctuations. *J. Eng. Gas Turbines Power*, 125(1):11–19, 2003. DOI: 10.1115/1.1365159.

[64] J. Eckstein, E. Freitag, C. Hirsch, and T. Sattelmayer. Experimental Study on the Role of Entropy Waves in Low-Frequency Oscillations for a Diffusion Burner. In *Proceedings of the ASME Turbo Expo 2004*, pages 743–751, 2004. DOI: 10.1115/GT2004-54163.

[65] T. Hummel. *Modeling and Analysis of High-Frequency Thermoacoustic Oscillations in Gas Turbine Combustion Chambers*. Ph.D. Thesis, Technische Universität München, Munich, 2019. URL: www.epc.ed.tum.de/fileadmin/w00cgc/td/Forschung/Dissertationen/Hummel2019.pdf.

[66] T. Hofmeister, T. Hummel, B. Schuermans, and T. Sattelmayer. Modeling and Quantification of Acoustic Damping Induced by Vortex Shedding in Noncompact Thermoacoustic Systems. *Journal of Engineering for Gas Turbines and Power*, 142(3):031016, 2020. DOI: 10.1115/1.4044936.

[67] N. Karimi, M. J. Brear, and W. H. Moase. Acoustic and disturbance energy analysis of a flow with heat communication. *J. Fluid Mech.*, 597:67–89, 2008. DOI: 10.1017/S0022112007009573.

[68] L. Strobio Chen, S. Bomberg, and W. Polifke. Propagation and generation of acoustic and entropy waves across a moving flame front. *Combustion and Flame*, 166:170–180, 2016. URL: www.sciencedirect.com/science/article/pii/S0010218016000286.

[69] S. W. Rienstra and A. Hirschberg. *An Introduction to Acoustics*. Eindhoven University of Technology, may 2016 edition, 2016. URL: www.win.tue.nl/~sjoerdr/papers/boek.pdf.

[70] J. Gikadi, M. Schulze, J. Schwing, S. Föller, and T. Sattelmayer. Linearized Navier-Stokes and Euler Equations for the Determination of the Acoustic Scattering Behaviour of an Area Expansion. In *18th AIAA/CEAS Aeroacoustics Conference*, 2012. DOI: 10.2514/6.2012-2292.

[71] G. Searby, M. Habiballah, A. Nicole, and E. Laroche. Prediction of the Efficiency of Acoustic Damping Cavities. *Journal of Propulsion and Power*, 24(3):516–523, 2008. DOI: 10.2514/1.32325.

[72] R. Codina. On stabilized finite element methods for linear systems of convection–diffusion-reaction equations. *Computer Methods in Applied Mechanics and Engineering*, 188(1-3):61–82, 2000. DOI: 10.1016/S0045-7825(00)00177-8.

[73] COMSOL. Comsol Multiphysics 4.4 Theory Guide.

[74] T. Hofmeister. *Influence of Acoustically Induced Vorticity Perturbations on High-Frequency Thermoacoustic Instabilities in Gas Turbine Combustors*. Ph.D. Thesis, Technische Universität München, Munich, 2021. URL: www.epc.ed.tum.de/fileadmin/w00cgc/td/Forschung/Dissertationen/hofmeister2021.pdf.

[75] D. G. Goodwin, R. L. Speth, H. K. Moffat, and B. W. Weber. *Cantera: An Object-oriented Software Toolkit for Chemical Kinetics, Thermodynamics, and Transport Processes*. 2018. DOI: 10.5281/zenodo.1174508. URL: www.cantera.org.

[76] G. P. Smith, D. M. Golden, M. Frenklach, N. W. Moriarty, and B. Eiteneer. GRI 3.0 mechanism. URL: combustion.berkeley.edu/gri-mech.

[77] G. He, Y. Guo, and A. T. Hsu. The effect of Schmidt number on turbulent scalar mixing in a jet-in-crossflow. *International Journal of Heat and Mass Transfer*, 42(20):3727–3738, 1999. URL: www.sciencedirect.com/science/article/pii/S0017931099000502.

[78] F. Guethe, D. Guyot, G. Singla, N. Noiray, and B. Schuermans. Chemiluminescence as diagnostic tool in the development of gas turbines. en. *Applied Physics B*, 107(3):619–636, 2012. DOI: 10.1007/s00340-012-4984-y.

[79] S. Sardeshmukh, M. Bedard, and W. Anderson. The use of OH* and CH* as heat release markers in combustion dynamics. en. *International Journal of Spray and Combustion Dynamics*, 9(4):409–423, 2017. DOI: 10.1177/1756827717718483.

[80] N. Klarmann, T. Sattelmayer, W. Geng, B. T. Zoller, and F. Magni. Impact of Flame Stretch and Heat Loss on Heat Release Distributions in Gas Turbine Combustors: Model Comparison and Validation. In *Proceedings of the ASME Turbo Expo 2016*, 2016. DOI: 10.1115/GT2016-57625.

[81] J. A. van Oijen, A. Donini, R. J. M. Bastiaans, J. H. M. ten Thije Boonkkamp, and L. P. H. de Goey. State-of-the-art in premixed combustion modeling using flamelet generated manifolds. *Progress in Energy and Combustion Science*, 57:30–74, 2016. URL: www.sciencedirect.com/science/article/pii/S0360128515300137.

[82] M. Brandt. *Beschreibung der Selbstzündung in turbulenter Strömung unter Einbeziehung ternärer Mischvorgänge*. Ph.D. Thesis, Technische Universität München, Munich, 2005. URL: www.epc.ed.tum.de/fileadmin/w00cgc/tfd/Forschung/Dissertationen/Brandt_2005_Beschreibung_der_Selbstzuendung_in_turbulenter_Stroemung_unter_Einbeziehung.pdf.

[83] X. Wang. *Modélisation et Simulation Numérique de la Combustion en Présence d' Interactions Flammes/Auto-Inflammation*. Ph.D. Thesis, ISAE-ENSMA, École Nationale Supérieure de Mécanique et d'Aérotechique, Poitiers, 2020. URL: https://tel.archives-ouvertes.fr/tel-02860046.

[84] O. Schulz, T. Jaravel, T. Poinsot, B. Cuenot, and N. Noiray. A criterion to distinguish autoignition and propagation applied to a lifted methane–air jet flame. *Proceedings of the Combustion Institute*, 36(2):1637–1644, 2017. URL: www.sciencedirect.com/science/article/abs/pii/S1540748916304114.

[85] M. Zahn, M. Schulze, C. Hirsch, M. Betz, and T. Sattelmayer. Frequency Domain Predictions of Acoustic Wave Propagation and Losses in a Swirl Burner With Linearized Navier-Stokes Equations. In *Proceedings of the ASME Turbo Expo 2015*, 2015. DOI: 10.1115/GT2015-42723.

[86] R. Kathan. *Verlustmechanismen in Raketenbrennkammern*. Ph.D. Thesis, Technische Universität München, Munich, 2013. URL: www.epc.ed.tum.de/fileadmin/w00cgc/td/Forschung/Dissertationen/Kathan2013.pdf.

[87] E. W. Lemmon and R. T Jacobsen. Viscosity and Thermal Conductivity Equations for Nitrogen, Oxygen, Argon, and Air. en. *International Journal of Thermophysics*, 25(1):21–69, 2004. DOI: 10.1023/B:IJOT.0000022327.04529.f3.

[88] M. Hertweck. *Einfluss der Flammenposition auf transversale hochfrequente akustische Moden in zylindrischen Brennkammern*. Ph.D. Thesis, Technische Universität München, Munich, 2016. URL: www.epc.ed.tum.de/fileadmin/w00cgc/td/Forschung/Dissertationen/hertweck16.pdf.

[89] Rayleigh, John William Strutt. *The theory of sound*. 1896. URL: www.archive.org/details/theorysound06raylgoog/page/n1/mode/2up.

[90] F. Nicoud and T. Poinsot. Thermoacoustic instabilities: Should the Rayleigh criterion be extended to include entropy changes? *Combustion and Flame*, 142(1-2):153–159, 2005. URL: www.hal.archives-ouvertes.fr/hal-00908285/file/chu-CandF-final.pdf.

[91] P. Romero, F. M. Berger, T. Hummel, B. Schuermans, and T. Sattelmayer. Numerical Design of a Novel Reheat Experiment for the Analysis of High-Frequency Flame Dynamics. In *Proceedings of the ASME Turbo Expo 2018*, 2018. DOI: 10.1115/GT2018-77034.

[92] D. E. Rogers and F. E. Marble. A Mechanism for High-Frequency Oscillation in Ramjet Combustors and Afterburners. *Journal of Jet Propulsion*, 26(6):456–462, 1956. DOI: 10.2514/8.7049. American Institute of Aeronautics and Astronautics.

[93] N. B. George, V. R. Unni, M. Raghunathan, and R. I. Sujith. Pattern formation during transition from combustion noise to thermoacoustic instability via intermittency. en. *Journal of Fluid Mechanics*, 849:615–644, Aug. 2018. DOI: 10.1017/jfm.2018.427.

[94] M. Oschwald, Z. Farago, G. Searby, and F. Cheuret. Resonance Frequencies and Damping of a Combustor Acoustically Coupled to an Absorber. *Journal of Propulsion and Power*, 24(3):524–533, 2008. DOI: 10.2514/1.32313.

[95] N. Noiray and B. Schuermans. Deterministic quantities characterizing noise driven Hopf bifurcations in gas turbine combustors. *International Journal of Non-Linear Mechanics*, 50:152–163, Apr. 2013. URL: www.sciencedirect.com/science/article/pii/S0020746212001825.

[96] M. Gruberbauer, T. Kallinger, W. W. Weiss, and D. B. Guenther. On the detection of Lorentzian profiles in a power spectrum: A Bayesian approach using ignorance priors. *Astronomy & Astrophysics*, 506(2):1043–1053, Nov. 2009. DOI: 10.1051/0004-6361/200811203. arXiv: 0811.3345.

[97] P. Stoica and R. L. Moses. *Spectral analysis of signals*. Pearson/Prentice Hall, Upper Saddle River, N.J, 2005.

[98] MATLAB. *version 9.9.0.1467703 (R2020b)*. The MathWorks Inc., Natick, Massachusetts, 2020.